Land Surface Temperature and Emissivity Retrieval from Thermal
Infrared Hyperspectral Imagery

by

Marvin Boonmee

B.S. Rochester Institute of Technology, 2001

A dissertation submitted in partial fulfillment of the
requirements for the degree of Doctor of Philosophy
in the Chester F. Carlson Center for Imaging Science
Rochester Institute of Technology

October 22, 2007

Signature of the Author ⎯⎯⎯⎯⎯⎯⎯⎯⎯⎯⎯⎯⎯⎯⎯⎯⎯⎯⎯

Accepted by ⎯⎯⎯⎯⎯⎯⎯⎯⎯⎯⎯⎯⎯⎯⎯⎯⎯⎯⎯⎯⎯
        Coordinator, Ph.D. Degree Program   Date

CHESTER F. CARLSON CENTER FOR IMAGING SCIENCE

ROCHESTER INSTITUTE OF TECHNOLOGY

ROCHESTER, NEW YORK

<u>CERTIFICATE OF APPROVAL</u>

Ph.D. DEGREE DISSERTATION

The Ph.D. Degree Dissertation of Marvin Boonmee
has been examined and approved by the
dissertation committee as satisfactory for the
dissertation required for the
Ph.D. degree in Imaging Science

_____
Dr. John R. Schott, Dissertation Advisor

_____
Dr. Satish Kandlikar

_____
Dr. David W. Messinger

_____
Dr. Carl Salvaggio

_____
Date

DISSERTATION RELEASE PERMISSION

ROCHESTER INSTITUTE OF TECHNOLOGY

CHESTER F. CARLSON CENTER FOR IMAGING SCIENCE

Title of Dissertation:

Land Surface Temperature and Emissivity Retrieval from Thermal Infrared

Hyperspectral Imagery

I, Marvin Boonmee, hereby grant permission to Wallace Memorial Library of R.I.T. to reproduce my thesis in whole or in part. Any reproduction will not be for commercial use or profit.

Signature _____

Date

Land Surface Temperature and Emissivity Retrieval from Thermal Infrared Hyperspectral Imagery

by

Marvin Boonmee

Submitted to the
Chester F. Carlson Center for Imaging Science
in partial fulfillment of the requirements
for the Doctor of Philosophy Degree
at the Rochester Institute of Technology

Abstract

A new algorithm, optimized land surface temperature and emissivity retrieval (OLSTER), is presented to compensate for atmospheric effects and retrieve land surface temperature (LST) and emissivity from airborne thermal infrared hyperspectral data. The OLSTER algorithm is designed to retrieve properties of both natural and man-made materials. Multi-directional or multi-temporal observations are not required, and the scenes do not have to be dominated by blackbody features.

The OLSTER algorithm consists of a preprocessing step, an iterative search for near-blackbody pixels, and an iterative constrained optimization loop. The preprocessing step provides initial estimates of LST per pixel and the atmospheric parameters of transmittance and upwelling radiance for the entire image. Pixels that are under- or over-compensated by the estimated atmospheric parameters are classified as near-blackbody and lower emissivity pixels, respectively. A constrained optimization of the atmospheric parameters using generalized reduced gradients on the near-blackbody pixels ensures physical results. The downwelling radiance is estimated from the upwelling radiance by applying a look-up table of coefficients based on a polynomial regression of radiative

transfer model runs for the same sensor altitude. The LST and emissivity per pixel are retrieved simultaneously using the well established ISSTES algorithm.

The OLSTER algorithm retrieves land surface temperatures within about $\pm$ 1.0 K, and emissivities within about $\pm$ 0.01 based on numerical simulation and validation work comparing results from sensor data with ground truth measurements. The OLSTER algorithm is currently one of only a few algorithms available that have been documented to retrieve accurate land surface temperatures and absolute land surface spectral emissivities from passive airborne hyperspectral LWIR sensor imagery.

Acknowledgements

This work is dedicated to...

... my parents, whose hard work have allowed my brother and I to pursue our dreams.

... to my aunt Wandee, who tutored me when I was growing up.

... to all of my family for their support.

... and to my loving wife, Yan.

Contents

List of Figures

List of Tables

Chapter 1

Introduction

The retrieval of land surface temperature (LST) and land surface emissivity (LSE) from airborne passive hyperspectral sensors for the purpose of producing LST, LSE, and material classification maps is an ongoing area of research in remote sensing. Remote sensing allows for measurements of surface temperature on a regional or global scale. An airborne sensor measures the surface-leaving radiance modified by the atmosphere in different spectral channels. The surface parameter retrieval uses the thermal infrared (TIR) spectral region, which contains useful information about the emissive and thermal properties of the land surface. A desirable goal is to retrieve LST to better than 1 K, and LSE values to within $\pm\,0.01$.

LST retrieval is a difficult problem compared to retrieving sea surface temperatures (SST). The variable emissivity of the land presents certain difficulties. There are also problems associated with making a representative measurement of the land surface temperature. Daytime surface temperatures can vary by more than 10 K in just a few centimeters, and on a sunny afternoon temperatures can change by more than 1 K in less than a minute (Prata et al., 1995).

LST is an important parameter for modeling surface-atmosphere processes such as energy transfer. It is an indication of the equilibrium thermodynamic state resulting from the energy balance of the fluxes between the atmosphere, surface, and the subsurface soil (Schmugge et al., 2002). The LST distribution can be used as input for modeling and predicting climate change at various scales and can provide a constraint on model predictions. LST applications in environmental studies include the energy and water exchange between the atmosphere and the surface, vegetation monitoring and discrimination, frost detection and forecasting, monitoring water-stress in crops, and evapotranspiration. LST is sensitive to vegetation and soil moisture, and can be used to detect long-term land surface changes (Dash et al., 2002). One of the most important potential applications of LST retrieved from satellite data is to validate and improve global meteorological models (Wan et al., 2002).

LSE contains information about the structure and composition of the Earth's surface. The LSE gives the efficiency of the surface for transmitting the radiant energy into the atmosphere. LSE depends on the composition, surface roughness, and physical parameters of the surface, such as moisture content. In addition, the emissivity generally will vary with wavelength for natural surfaces (Schmugge et al., 2002). LSE provides useful information for geological studies because silicate materials in rocks and soils have various spectral shapes in emissivity (Tonooka, 2001). In the 8 to 12 μm atmospheric window, mineral groups such as silicates, carbonates, sulfates, and phosphates have spectral features related to the fundamental vibrational frequencies of their interatomic bonds. These features are known as reststrahlen bands, and can be used to identify a mineral sample. LSE also can be used to discriminate senescent vegetation (Wan et al., 2002). Estimation of emissivity is trivial for heavily vegetated surfaces since the emissivity is relatively uniform and close to one. For arid lands with sparse vegetation, the problem is more difficult

because the emissivity of the exposed soils and rocks is highly variable (Schmugge et al., 2002). Lack of knowledge of LSE introduces an LST error, which can be defined as the difference of LST retrieved at the actual LSE and at $\epsilon = 1$. For a LSE of 0.98 and a ground height of 0 km, the error on the LST retrieved using a single-channel method ranges from 0.2 K to 1.2 K for mid-latitude summer and from 0.8 K to 1.4 K for mid-latitude winter conditions (Dash et al., 2002). The LST error increases with decreasing emissivities, e.g. for $\epsilon = 0.93$ and a ground height of 0.5 km the LST error ranges from 0.8 K to 3.4 K for mid-latitude summer and from 2.8 K to 4.8 K for mid-latitude winter (Dash et al., 2002). Methods for LSE determination either aim for relative or absolute emissivity. The relative methods retrieve the spectral shape/ratio of emissivities, while the absolute methods depend on critical assumptions (Dash et al., 2002).

The radiative energy emitted by the Earth's surface interacts with the atmosphere. In the TIR region (8 to 14 μm), the interactions consist mainly of absorption and re-emission by the atmospheric gases. The absorbing gases include water vapor (H_2O), carbon dioxide (CO_2), ozone (O_3), CFCs, and aerosols (Prata et al., 1995). Water vapor is the principal absorber for these wavelengths. Other gases, such as ionospheric O_3 and CO_2, vary slowly. CO_2 is evenly distributed in the atmosphere, and tropospheric O_3 is of local importance only (Dash et al., 2002). The effect of fixed gases can be considered as constant at a global scale and small compared to the water vapor effect (Prata et al., 1995). In the case of clear-sky conditions, aerosol absorption and scattering is negligible and generally ignored (Prata et al., 1995). The transmission corresponding to aerosol absorption and scattering in the TIR is in the range of 0.95-0.98, unless volcanic eruptions strongly change the aerosol distribution.

Temperature and water vapor profiles in the atmosphere are two critical parameters for estimating the total atmospheric absorption and radiation. The size of the atmospheric

effects varies both with the water vapor content and the vertical profiles of temperature and pressure (Prata et al., 1995). The distributions of temperature and radiatively active gases in the atmosphere control atmospheric absorption and radiation. The distributions can vary significantly with time and location (Gu et al., 2000).

The absorption by water vapor is due to the absorption lines and also due to the continuum. The water vapor continuum is probably due to the effects of the far wings of strong absorption lines and to the presence of water vapor dimers $(H_2O)_2$ or polymers (Prata et al., 1995). Water vapor is largely concentrated near the surface-atmosphere boundaries (Gu et al., 2000).

The atmospheric transmittances vary with the total water vapor amount (Prata et al., 1995). Typical values of the transmittance due to water vapor vary from about 0.95 for dry atmospheres to 0.3-0.4 for humid atmospheres. This is due to the large variability of the total column of water vapor and the strong dependence on humidity of the continuum absorption mechanism (Prata et al., 1995). Water vapor is poorly mixed and varies on short time-scales (Dash et al., 2002). Radiosondes are useful for collecting the temperature and water-vapor profiles and other information about the state of the atmosphere (Dash et al., 2002). However, radiosonde data is only applicable when synchronized with the imaging sensor in location and time.

The estimation of the surface-leaving radiance from the at-sensor radiance of an airborne sensor requires atmospheric compensation. The surface-leaving radiance, also referred to as the at-surface radiance, includes the surface-emitted radiance and the surface-reflected downwelling radiance. In order to retrieve the surface temperature and emissivity from the surface-leaving radiance, a separation of the surface emissivity and surface temperature terms is required. A warm, humid atmosphere represents a difficult case for the general temperature/emissivity separation (TES) problem due to the low atmo-

spheric transmittance and high atmospheric emission effects (Ingram and Muse, 2001). The at-sensor radiance for a cold surface under a warm atmosphere is dominated by the upwelling radiance and reflected downwelling radiance. Errors in the atmospheric compensation spectra will be amplified for these difficult conditions.

A problem is properly posed if the solution satisfies the following requirements: (1) the solution must exist (existence); (2) the solution must be uniquely determined by the data (uniqueness); and (3) the solution must depend continuously on the data (stability) (Liang, 2000). The TES problem is ill-posed because a sensor with N spectral channels has N values of spectral radiance with $N+1$ unknowns; N emissivities (one per channel) plus one surface temperature (Li et al., 1999). There is no unique solution unless additional independent information is added to constrain the extra degree of freedom (Li et al., 1999).

Additional information comes from measurements, such as humidity data and radiosonde data, the use of empirical equations, and physical limits on the solution. This has led to the development of algorithms that differ according to the assumptions that they make (Schmugge et al., 2002). Many atmospheric compensation algorithms ignore surface-emissivity, or assign a constant value of emissivity to all pixels in the dataset. This may not be a realistic approximation for natural surfaces.

In addition to being underdetermined, the radiative transfer equation (RTE) is also nonlinear. The main sources of the nonlinearity in the RTE are: 1) the temperature dependence of the atmospheric transmission, 2) the dependence of transmission on absorber concentration, 3) temperature dependence of the Planck function, 4) wavelength dependence of the Planck function across a spectral band, 5) wavelength dependence of the Planck function between spectral bands, and 6) nonlinear constraints (Wan and Li, 1997).

The approach in this research uses an optimization loop and constraint functions to

overcome the ill-posed retrieval problem. The algorithm accounts for downwelling radiance, and can be applied to both man-made and natural surfaces. Ancillary data such as a radiosonde profile are not required. The next section describes the specific goals of the research and of the LST/LSE retrieval algorithm.

1.1 Objectives

The goal of this research is to develop and test an algorithm for atmospheric compensation and surface parameter retrieval of land surface temperature and land surface emissivity using airborne hyperspectral TIR radiance imagery. The desired accuracy is a temperature estimation within ± 1 K and retrieved emissivity values within ± 0.01.

The approach is a hybrid algorithm using data-driven methods and physics-based modeling. The atmospheric compensation accounts for downwelling radiance. An optimization approach is used to ensure physical results and to minimize the impact of non-unique and unstable solutions due to sensor noise and artifacts. Empirical relationships are avoided where possible, and surface materials are not limited to natural objects or to materials from a database. Ancillary sounding data is not required, and image registration issues associated with multi-directional and multi-temporal methods are avoided.

A sensitivity analysis of the model parameters, such as sensor noise and altitude, is used to determine the strengths and weaknesses of the retrieval algorithm, as well as for providing insight for improvements. Validation of the approach was performed using sensor data with corresponding ground truth measurements. Results from a comparison with other algorithms in the literature are also presented. The next chapter provides a review of the governing equations and current algorithms available for atmospheric compensation and temperature and emissivity separation.

Chapter 2

Background

The temperature measured by a radiometer (radiometric temperature) is proportional to the temperature measured by a thermometer (thermodynamic temperature) for homogeneous isothermal surfaces (Dash et al., 2002). In certain cases, it is not possible to compare the thermodynamic temperature with the radiometric temperature. The land surface is composed of different materials with various geometries that complicate radiometric temperature estimation (Dash et al., 2002). When a radiometric temperature measurement is made over inhomogeneous or structured surfaces, the location of the point measurement for thermodynamic temperature is not clearly defined. Radiometric temperature measurements are more useful than thermodynamic temperatures for estimating the temperature of complex surfaces such as vegetation canopies. If the emissivity of the surface is unknown, then the radiometric temperature will not be accurate.

In remote sensing, land surface temperature (LST) is defined as the ensemble directional radiometric surface temperature corresponding to the instantaneous field-of-view of the sensor (Norman and Becker, 1995). The ensemble represents the bulk contribution of an inhomogeneous pixel. LST depends on the distribution of temperature and emissivity

within a pixel, the spectral channel of measurement, and the viewing angle.

The directional emissivity for opaque objects at thermal equilibrium at a specific wavelength, λ, is related to the hemispherical-directional reflectance by Kirchhoff's Law

$$\varepsilon\left(\theta, \phi, \lambda\right) = 1 - r\left(\theta, \phi, \lambda\right), \tag{2.1}$$

where θ is the zenith angle and ϕ is the azimuth angle (Norman and Becker, 1995). The hemispherical emissivity for a wavelength band i is then defined as

$$\varepsilon_i = \frac{1}{\pi} \int_0^{2\pi} \int_0^{\pi/2} \varepsilon_i\left(\theta, \phi\right) \sin\theta \cos\theta \, \mathrm{d}\theta \, \mathrm{d}\phi. \tag{2.2}$$

The land surface emissivity (LSE) can be approximated with the bihemispherical thermal reflectance using

$$\varepsilon_i \cong 1 - r_i \tag{2.3}$$

and assuming a Lambertian surface and that ε_i varies only slightly with wavelength (Norman and Becker, 1995).

2.1 Governing Equations

The spectral radiance emitted by a blackbody surface is related to its temperature by the Planck function $\left(\frac{W}{m^2\ sr\ \mu m}\right)$,

$$L_{bb}(T, \lambda) = \frac{C_1}{\pi \lambda^5} \frac{1}{e^{C_2/\lambda T} - 1}, \tag{2.4}$$

where

$C_1 = 3.74151 \times 10^{-16}(Wm^2) = 2\pi hc^2$ first radiation constant;

$C_2 = 0.0143879(m\ K) = hc/k$ second radiation constant;

$\lambda(\mu m)$ wavelength;

$T(K)$ temperature;

$h = 6.626076 \times 10^{-34}(Js)$ Planck's constant;

$c = 2.99792458 \times 10^8(m/s)$ speed of light;

$k = 1.380658 \times 10^{-23}(J/K)$ Boltzmann's constant.

Given a blackbody radiance measurement, equation 2.4 can be solved for a brightness temperature vector, defined as

$$T_B\left(L_{bb}, \lambda\right) = \frac{C_2}{\lambda \ln\left(\frac{C_1}{\pi\lambda^5 L_{bb}} + 1\right)}. \tag{2.5}$$

The brightness temperature is the equivalent temperature required for a blackbody to emit a given radiance and is a function of wavelength.

The at-sensor radiance for an image pixel is given by the radiative transfer equation (RTE) (Dash et al., 2002),

$$
\begin{aligned}
L_i &= \int_{\lambda_1}^{\lambda_2} f_i(\lambda)\varepsilon(\lambda)L_{bb}(T_s, \lambda)\tau(\lambda)\,\mathrm{d}\lambda + \int_{p=0}^{p_s}\int_{\lambda_1}^{\lambda_2} f_i(\lambda)L_{bb}(T_p, \lambda)\frac{\mathrm{d}\tau}{\mathrm{d}p}\,\mathrm{d}\lambda\,\mathrm{d}p \\
&\quad + \int_{\phi=0}^{2\pi}\int_{\theta=0}^{\pi/2}\int_{\lambda_1}^{\lambda_2} \frac{(1-\varepsilon(\lambda))}{\pi} f_i(\lambda)L_d(\lambda, \theta, \phi)\tau(\lambda)\cos\theta\sin\theta\,\mathrm{d}\lambda\,\mathrm{d}\theta\,\mathrm{d}\phi, (2.6)
\end{aligned}
$$

where

$$i \qquad \text{channel;}$$

$$f_i \qquad \text{normalized channel response function ;}$$

$$\theta \qquad \text{zenith angle ;}$$

$$\phi \qquad \text{azimuth angle ;}$$

$$\lambda_1, \lambda_2 \qquad \text{spectral range of the channel;}$$

$$L_d \qquad \text{downwelling radiance;}$$

$$p, p_s \qquad \text{pressure, and pressure at the surface;}$$

$$T_s, T_p \qquad \text{surface temperature and air temperature at pressure p.}$$

The first term in the RTE is the radiance emitted by the surface, the second term is the upwelling radiance from the atmosphere, and the last term is the surface reflected radiance. In the thermal infrared, the RTE assumes that the atmosphere is at local thermodynamic equilibrium, that the surface is Lambertian, and that there is no scattering (Dash et al., 2002). The RTE can be simplified by writing the Planck function for a given channel as

$$L_{bb\_i}(T) = \int_{\lambda_1}^{\lambda_2} f_i(\lambda) L_{bb}(T, \lambda) \, d\lambda. \tag{2.7}$$

The downward hemispherical irradiance is given by

$$E_{hem\_i}^{\downarrow} = \int_{\phi=0}^{2\pi} \int_{\theta=0}^{\pi/2} L_d(\lambda) \cos\theta \sin\theta \, d\theta \, d\phi. \tag{2.8}$$

After integrating over the channel response and applying the mean value theorem for integrals, the RTE can be expressed as equations 2.9 and 2.10,

$$L_{obs\_i} = \varepsilon_i \tau_i(\theta) L_{bb\_i}(T_s) + L_{u\_i}(\theta) + \frac{1 - \varepsilon_i}{\pi} \tau_i(\theta) E^{\downarrow}_{hem\_i}, \tag{2.9}$$

$$L_{obs\_i} = \varepsilon_i \tau_i(\theta) L_{bb\_i}(T_s) + L_{u\_i}(\theta) + (1 - \varepsilon_i) \tau_i(\theta) L_{d\_i}. \tag{2.10}$$

The surface-leaving radiance here is defined as

$$L_{surf\_i}(x) = \varepsilon_i(x) L_{bb\_i}(T_s(x)) + [1 - \varepsilon_i(x)] L_{d\_i}(x), \tag{2.11}$$

where x is pixel location. The at-sensor observed spectral radiance is modeled by the modified RTE,

$$L_{obs\_i}(x) = L_{surf\_i}(x) \tau_i(x) + L_{u\_i}(x), \tag{2.12}$$

where $\tau_i(x)$ is the atmospheric transmittance along the sensor's line of sight (LOS) and $L_{u\_i}(x)$ is the upwelling atmospheric radiance along the LOS. Both equations 2.11 and 2.12 assume that there are no mixed pixels in the TIR data.

2.2   Algorithms in the literature

The following is a brief review of the algorithms in the literature. These algorithms address specific retrieval problems such as atmospheric compensation and temperature/emissivity separation, and some address both as an end-to-end solution. Each algorithm has its advantages and disadvantages, mostly based on the assumptions made to overcome the ill-posed nature of the surface parameter retrieval problem.

2.2.1   In-Scene Atmospheric Compensation

The In-Scene Atmospheric Compensation (ISAC) algorithm (Young et al., 2002) esti-mates the relative atmospheric transmittance and upwelling radiance spectra directly from the TIR image data. The relative atmospheric transmittance and upwelling radiance spec-tra are scaled to absolute values using the transmittance and upwelling radiance from a radiative transfer model at a reference channel. The radiative transfer equation can be lin-earized by assuming blackbody features in the TIR image. With $\epsilon(x, \lambda) \approx 1$, the surface-leaving radiance can be approximated as $L_{surf}(x, \lambda) \approx L_{bb}(T(x), \lambda)$. The blackbody assumption effectively means that ISAC ignores downwelling radiance.

ISAC assumes that the atmosphere is spatially uniform over the sensor's field of view (FOV). After substituting the approximate surface-leaving radiance into equation 2.12 and removing the spatial dependence of the atmospheric parameters, the RTE for the ISAC algorithm can be defined as

$$L_{obs}(\lambda) \cong \tau(\lambda)L_{bb}(T, \lambda) + L_u(\lambda). \tag{2.13}$$

The steps in the ISAC algorithm are given in Table 2.1. The first step converts the ob-served radiance at the sensor to brightness temperature using the inverse Planck function, implemented as a numerical version of equation 2.5 over the sensor bandpass. The un-compensated observed radiance spectrum plotted as brightness temperature per pixel will exhibit spectral structure caused by the atmosphere and surface spectral emissivity. It is likely that at λ_m, the wavelength where the maximum brightness temperature occurs for a given pixel, $\varepsilon(\lambda_m)$ and $\tau(\lambda_m)$ are close to unity, and $L_u(\lambda_m)$ is close to zero (Young et al., 2002). A common reference channel for all pixels, λ_r, is selected to avoid inconsistencies in the definition of the atmospheric compensation parameters. The spectral channel with

Table 2.1: ISAC algorithm

1.	Compute the brightness temperature spectrum per pixel, $T_B(L_{obs}(x, \lambda), \lambda)$.
2.	Select a reference channel, λ_r, defined as the spectral channel with the most maximum brightness temperatures.
3.	Estimate $\hat{T}_s(x)$ per pixel using $T_B(L_{obs}(x, \lambda_r), \lambda_r)$.
4.	Compute the Planck radiance per pixel, $\hat{L}_{BB}(\hat{T}_s(x), \lambda)$.
5.	Estimate the $\hat{\tau}(\lambda)$ and $\hat{L}_u(\lambda)$ spectra with $L_{obs}(\lambda)$ versus $\hat{L}_{BB}(\lambda)$ linear regressions fitted to the top of each scatter plot, with $\hat{\tau}(\lambda)$ = slope, and $\hat{L}_u(\lambda)$ = intercept. Only the pixels with a maximum brightness temperature at λ_r are included in the scatter plot.
6.	The relative atmospheric spectra are scaled to absolute spectra using the 11.7 μm water absorption band.
7.	Fit a line to the top of a scatter plot of the mean water band absorptance versus the total mean band radiance, and search a MODTRAN LUT for a match on band averages and rescale $\hat{\tau}(\lambda)$ and $\hat{L}_u(\lambda)$.
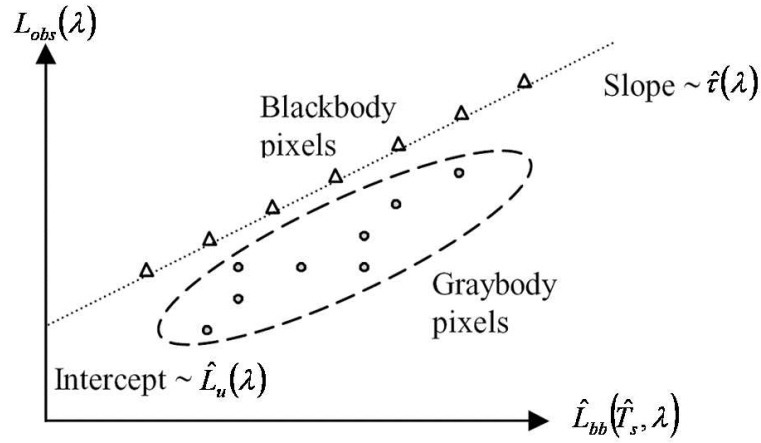
Figure 2.1: An illustration of a scatter plot of the observed radiance versus Planck radiance per wavelength used to estimate the atmospheric parameters (Borel, 2003)

the most occurrences of λ_m is defined as λ_r.

The surface temperature $\hat{T}_s(x)$ per pixel is estimated using $T_B(L_{obs}(x, \lambda_r), \lambda_r)$, and the Planck radiance per pixel is approximated by $\hat{L}_{BB}(\hat{T}_s(x), \lambda)$. A scatter plot of the observed radiance versus the estimated Planck radiance is created for each spectral channel using only the "most-hits" pixels where $\lambda_m = \lambda_r$. An illustration of the observed radiance versus estimated Planck radiance scatter plot is shown in Figure 2.1. Limiting the scatter plot to the "most-hits" pixels is required because it is possible for low emissivity pixels to lie above the expected location of blackbody pixels in the upper edge of the cluster in the scatter plots due to a biased estimate of $\hat{T}_s(x)$ that underestimates the Planck radiance (Young et al., 2002).

The $\hat{\tau}(\lambda)$ and $\hat{L}_u(\lambda)$ values are estimated as the slope and intercept of the line fitted to the points in the scatter plot for each spectral channel. The estimated $\hat{\tau}(\lambda)$ and $\hat{L}_u(\lambda)$ atmospheric compensation spectra may be unphysical, especially with negative values for the estimated upwelling radiance and values higher than one for the estimated atmo-

spheric transmittance. The unphysical values for the relative compensation spectra are the result of errors in the estimated $\hat{T}_s(x)$ and $\hat{L}_{BB}(\hat{T}_s(x), \lambda)$ caused by values of $\varepsilon(\lambda_r) < 1$, $\tau(\lambda_r) < 1$, and $L_u(\lambda_m) > 0$.

There are three empirical methods available for rescaling the estimated relative atmospheric spectra based on radiative transfer modeling of the atmosphere. One method uses radiosonde data as input into MODTRAN and adjusts $\hat{\tau}(\lambda)$ and $\hat{L}_u(\lambda)$ to match the MODTRAN transmittance and radiance at a specific wavelength. Alternatively, generic atmospheric profiles can be used instead of radiosonde data. Another method uses the 11.7 μm water absorption band. The line averages of transmittance and upwelling radiance describing the effect of line absorption in the water band is obtained by a line fit to a scatter plot of the average radiance depression due to line absorption versus the total mean band radiance for all pixels. The line averages of transmittance and upwelling radiance is related to the band averages of the total transmission and upwelling radiance by searching a table of MODTRAN calculated line, continuum, and total transmittance spectra, as well as total upwelling radiance. The MODTRAN calculations vary the temperature and water vapor concentration in US 1976 standard model by a factor of ten (Young et al., 2002).

The ISAC algorithm avoids the direct use of spectra from radiative transfer codes as the atmospheric compensation spectra. The data-driven approach used by the ISAC algorithm has the advantage of being insensitive to errors in the sensor's spectral calibration. Spectral miscalibration issues can amplify instead of eliminate the atmospheric effects, resulting in unsmooth brightness temperature and emissivity spectra (Young et al., 2002).

The linearization of the RTE requires that the scenes be dominated by blackbody features such as water or vegetation. In addition, a spread in surface temperatures is also required to avoid a noisy regression of the atmospheric compensation spectra. ISAC does not account for the reflected downwelling atmospheric radiance.

2.2.2   Autonomous Atmospheric Compensation

The Autonomous Atmospheric Compensation (AAC) algorithm (Gu et al., 2000), uses the 11.73 μm water absorption band to calculate two index parameters, the transmittance ratio and the upwelling radiance difference between the strong and weak absorption channels. The index parameters are then used to estimate the atmospheric transmittance and upwelling radiance spectra for separating the atmospheric and surface radiation. AAC uses the image data near the water band as input for the radiative transfer model. The assumptions in AAC include a spatially homogenous local atmosphere over a spatially variable land surface and that the surface-leaving radiance spectra are smoother than the atmospheric radiation and absorption spectra.

The ratio of the surface-leaving radiance at wavelengths λ_1 and λ_2 is a result of rearranging equation 2.12 to give,

$$\frac{L_{surf}(x, \lambda_1)}{L_{surf}(x, \lambda_2)} \frac{\tau(x, \lambda_1)}{\tau(x, \lambda_2)} = \frac{L_{obs}(x, \lambda_1) - L_u(x, \lambda_1)}{L_{obs}(x, \lambda_2) - L_u(x, \lambda_2)}. \tag{2.14}$$

Solving for the at-sensor observed radiance at λ_1 gives

$$\begin{aligned}
L_{obs}(x, \lambda_1) = &\frac{L_{surf}(x, \lambda_1)}{L_{surf}(x, \lambda_2)} \frac{\tau(x, \lambda_1)}{\tau(x, \lambda_2)} L_{obs}(x, \lambda_2) + L_u(x, \lambda_1) \\
&- \frac{L_{surf}(x, \lambda_1)}{L_{surf}(x, \lambda_2)} \frac{\tau(x, \lambda_1)}{\tau(x, \lambda_2)} L_u(x, \lambda_2).
\end{aligned} \tag{2.15}$$

When the wavelengths λ_1 and λ_2 are close to each other, with one of the wavelengths in an atmospheric absorption band and the other outside the band, the surface-leaving radiance difference between λ_1 and λ_2 can be small and neglected compared to the difference for the τ and L_u variables (Gu et al., 2000). The λ_1 and λ_2 are relabeled as λ_s and λ_w, with λ_s as the center wavelength in a strong absorption band and λ_w in a weak absorption band.
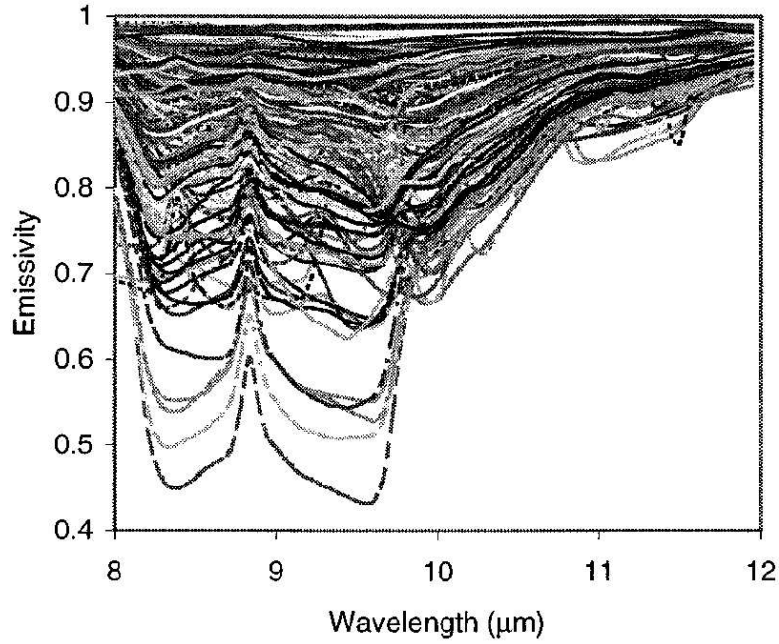
Figure 2.2: Emissivity spectra from the ASTER spectral library. The emissivity values are relatively close to one with less spectral variability near the 11.73 μm water band compared to other wavelengths (Gu et al., 2000).

The 11.73 μm water absorption band, where the emissivity of most natural materials are smooth and close to unity, is used in the AAC algorithm. An example for various natural surface materials is shown in Figure 2.2.

Neglecting the surface-leaving radiance difference and relabeling λ_1 and λ_2 as λ_s and λ_w, equation 2.15 now becomes

$$
\begin{aligned}
L_{obs}(x, \lambda_s) = & \frac{\tau(x, \lambda_s)}{\tau(x, \lambda_w)} L_{obs}(x, \lambda_w) + L_u(x, \lambda_s) \\
& - \frac{\tau(x, \lambda_s)}{\tau(x, \lambda_w)} L_u(x, \lambda_w).
\end{aligned}
\tag{2.16}
$$

The atmospheric index parameters transmittance ratio (Tr) and path radiance difference

Table 2.2: AAC algorithm

1.	Define the weak and strong absorption channels.
2.	Run radiative transfer models to derive the coefficients C(λ).
3.	Divide the image into pixel blocks. The atmosphere is assumed to be spatially homogeneous in each block.
4.	For each pixel block, estimate Tr and Pd with equation 2.18.
5.	For each pixel block, estimate $\hat{\tau}(\lambda)$ and $\hat{L}_u(\lambda)$ with equation 2.19.
6.	Compensate each pixel block for the atmosphere.

(Pd) measure the strength of the 11.73 μm water absorption band, and are defined as

$$Tr = \frac{\tau(x, \lambda_S)}{\tau(x, \lambda_W)} \tag{2.17a}$$

$$Pd = L_u(x, \lambda_S) - Tr L_u(x, \lambda_W). \tag{2.17b}$$

The linear regression model becomes

$$L_{obs}(x, \lambda_s) = Tr\ L_{obs}(x, \lambda_w) + Pd. \tag{2.18}$$

An empirical function used to solve for atmospheric transmittance and path radiance spectra using Tr and Pd is given by

$$y(\lambda) = \sum_{i=1}^{3} \sum_{j=1}^{3} C_{ij}(\lambda) Tr^{i-1} Pd^{j-1}, \tag{2.19}$$

where y is either transmittance or upwelling radiance and $C(\lambda)$ are wavelength-dependent coefficients. The steps in the AAC algorithm are given in Table 2.2.

The AAC algorithm requires that the surface materials have a smooth and high emissivity near the water absorption band. In general, this assumption works well for most

natural surfaces. The downwelling radiance is ignored in AAC. Another source of error in applying the AAC algorithm is the uncertainty in the instrument's spectral calibration. The radiative transfer model spectra require a resampling into instrument spectra which are used directly as the atmospheric compensation spectra. An error in the spectral location, bandwidth and filter shape of the sensor will result in errors in the atmospheric compensation. In general, the AAC spectra results are not as smooth as the results obtained from the ISAC algorithm.

2.2.3 ASTER's TES

The temperature/emissivity separation (TES) algorithm designed for the Advanced Spaceborne Thermal Emission and Reflection Radiometer (ASTER) thermal infrared (TIR) scanner aboard NASA's Earth Observing System, Terra (EOS-AM1), produces land surface temperature and emissivity images (Gillespie et al., 1998). ASTER has five bands in the TIR window. The input images for the TES algorithm are surface-leaving radiance, already compensated for atmospheric transmittance and upwelling radiance, and downwelling radiance from the ASTER standard product AST09. The TES algorithm consists of three modules that are adapted from previous temperature and emissivity techniques. The first module is the normalized emissivity method (NEM), used to estimate emissivities, iteratively remove reflected downwelling radiance, and estimate surface temperatures by assuming a maximum emissivity value. The ratio module (RAT) calculates emissivity ratios using the NEM temperatures. These emissivity ratios, called β spectra by the TES authors, resemble the shape of the actual emissivities but not the amplitude. The amplitude is estimated in the maximum-minimum relative emissivity difference (MMD) module by using an empirical relationship between the minimum emissivity and the emissivity's maximum-minimum difference for a library of laboratory reflectance spectra con-
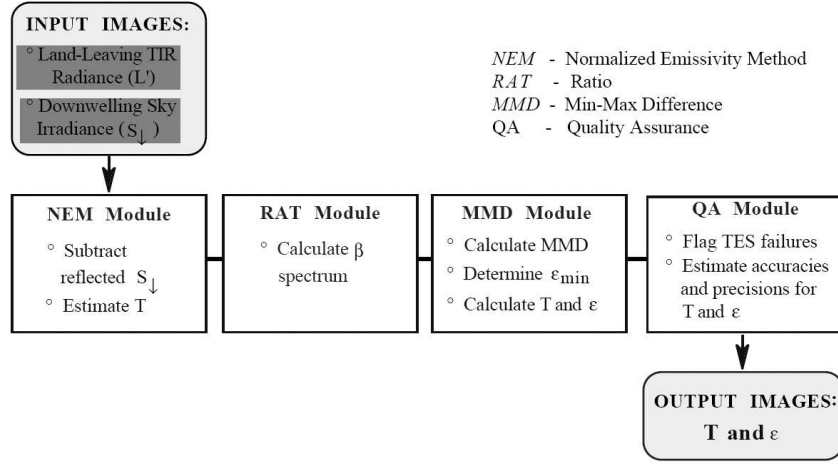
Figure 2.3: TES algorithm (Gillespie et al., 1998)

verted to equivalent emissivity (Gillespie et al., 1998). The MMD algorithm is similar to the alpha-derived emissivity method (ADE), which uses an empirical relationship between the mean emissivity and the variance of the alpha-residual emissivities instead. A flowchart of the TES algorithm is shown in Figure 2.3.

The maximum emissivity, ε_{max}, in the NEM module is assumed to be 0.99 (Gillespie et al., 1998). The surface-emitted radiance, $R(x, \lambda)$, is estimated by subtracting the reflected downwelling radiance from the surface-leaving radiance,

$$R(x, \lambda) \equiv \varepsilon(x, \lambda) L_{bb}(T(x), \lambda) = L_{surf}(x, \lambda) - (1 - \varepsilon_{max}) L_d(x, \lambda). \qquad (2.20)$$

The NEM temperature, $T_s(x)$, is defined as the maximum brightness temperature over all bands. The NEM temperature is used to calculate the apparent NEM emissivity by

dividing the surface-leaving radiance by the blackbody radiance at $T_s(x)$,

$$\varepsilon_N(x, \lambda) = \frac{R(x, \lambda)}{L_{bb}\left(T_s(x), \lambda\right)}. \tag{2.21}$$

The estimated surface-emitted radiance, $R(x, \lambda)$, is updated by replacing the maximum assumed emissivity with the apparent NEM emissivity,

$$R(x, \lambda) = L_{surf}(x, \lambda) - \left(1 - \varepsilon_N(x, \lambda)\right) L_d(x, \lambda). \tag{2.22}$$

The NEM module iteratively removes the reflected downwelling radiance by refining its estimates of emissivity and temperature. The iterations continue until the change in $R(x, \lambda)$ is less than some threshold or the number of iterations exceeds a limit.

The ratio module of TES simply computes the relative emissivity, $\beta(x, \lambda)$, by dividing each NEM emissivity by its average. The last step is the MMD module which scales the $\beta(x, \lambda)$ relative emissivities to absolute emissivities. An empirical relationship predicts the minimum emissivity, $\varepsilon_{\min}$, from the maximum-minimum relative emissivity difference (MMD),

$$\text{MMD}(x) = \beta(x, \lambda)\mid_{max} - \beta(x, \lambda)\mid_{min}, \tag{2.23}$$

and estimates the absolute emissivity with

$$\varepsilon(x, \lambda) = \beta(x, \lambda) \left(\frac{\varepsilon_{min}}{\beta(x, \lambda)\mid_{min}}\right). \tag{2.24}$$

The $\varepsilon_{\min}$ and MMD relationship was established using a library of 86 laboratory reflectance spectra of rocks, soils, vegetation, snow and water (Gillespie et al., 1998). The reflectance spectra were converted to equivalent emissivity by Kirchhoff's law and resampled with the ASTER sensor response. Then the $\varepsilon_{\min}$ data from the library were plotted
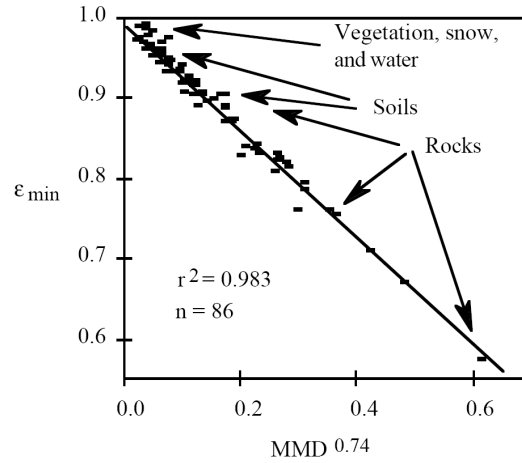
Figure 2.4: MMD and minimum emissivity relationship (Gillespie et al., 1998)

versus the MMD values, shown in Figure 2.4. The relationship follows an empirical power law,

$$\varepsilon_{\min} = 0.994 - 0.687 * MMD^{0.737}. \tag{2.25}$$

Minimum emissivity is used in the TES algorithm as opposed to the mean emissivity due to a higher correlation and less scatter about the regression line. MMD is used to measure spectral complexity due to its simplicity, although using variance reduces sensitivity to measurement error for near-blackbody surfaces (Gillespie et al., 1998). The $\varepsilon_{\min}$ versus MMD regression generally works well for natural surfaces only.

The TES algorithm is designed to recover temperatures to within 1.5 K and emissivities to 0.015 (Gillespie et al., 1998). The performance of the TES algorithm in general is related to the scatter about the $\varepsilon_{\min}$ - MMD regression line and the input surface-leaving radiance compensated for the atmospheric transmittance and upwelling radiance. The NEM module requires more iterations for the apparent emissivity to converge for lower emissivity surfaces, and may even diverge with each iteration. The emissivities never

converge for a low emissivity surface if the sky and ground temperatures are the same (Gillespie et al., 1998).

2.2.4 ISSTES and ARTEMISS

The iterative spectrally smooth temperature-emissivity separation (ISSTES) algorithm (Borel, 1998) retrieves emissivity spectra based on the spectral smoothness assumption. The surface emissivity spectrum of solids is comparatively smoother than the emissivity spectra of atmospheric gases in the TIR window. The spectral features of solids are usually wider than for gases. The width of a spectral feature is inversely proportional to the lifetimes of excited states. Solids have short lifetimes because the excited states are easily disrupted by thermal motions in the lattice crystal. Gases have longer lifetimes of excited states with their isolated molecules, and have narrower spectral features than solids. This approach requires the use of hyperspectral sensors to resolve the spectral features.

The ISSTES algorithm creates an ensemble of estimated emissivity spectra by varying the surface temperature over a small range about an estimated temperature. An example of the ensemble of emissivity spectra is shown in Figure 2.5. The emissivity for a given pixel is defined as

$$\varepsilon\left(\lambda\right) = \frac{L_{obs}\left(\lambda\right) - L_u\left(\lambda\right) - \tau\left(\lambda\right)L_d\left(\lambda\right)}{\tau\left(\lambda\right)L_{bb}\left(\lambda, T_s\right) - \tau\left(\lambda\right)L_d\left(\lambda\right)}. \tag{2.26}$$

The temperature that produces the smoothest emissivity spectrum is chosen as the surface temperature estimate. Adjusting the temperature in equation 2.26 effectively balances the atmospheric emission lines in the upwelling radiance with the emission lines in the downwelling radiance (Bower et al., 1999). A measure of spectral smoothness, S, is defined by

$$S = \sum_{i=2}^{N-1}\left\{\varepsilon_i - \frac{\varepsilon_{i-1} + \varepsilon_i + \varepsilon_{i+1}}{3}\right\}^2, \tag{2.27}$$
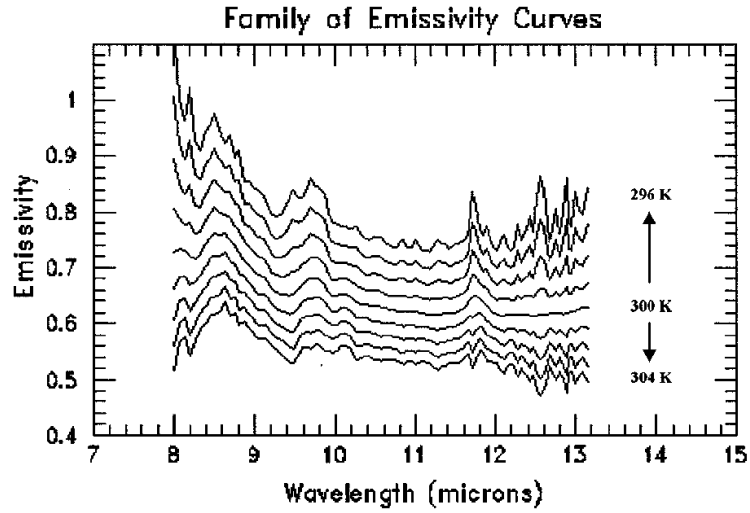
Figure 2.5: The ISSTES algorithm estimates the surface temperature based on the spectral smoothness of the retrieved emissivity. (Ingram and Muse, 2001)

where i is the spectral channel (Ingram and Muse, 2001). The ISSTES algorithm attempts to minimize the smoothness measure by varying the temperature.

An evaluation of the sensitivity of the ISSTES algorithm to algorithmic and measurement errors is available in the literature (Ingram and Muse, 2001). A general error model was used to quantify algorithmic, measurement, and parameter error. The vectors $\mathbf{X}$ and $\mathbf{Y}$ are the temperature and emissivity state vector and the observed spectral radiance vector, respectively, and are defined as

$$\mathbf{X} = \begin{pmatrix} t \\ \varepsilon_1 \\ \vdots \\ \varepsilon_n \end{pmatrix}, \tag{2.28}$$

$$\text{and} \quad \mathbf{Y} = \begin{pmatrix} L_1 \\ L_2 \\ \vdots \\ L_n \end{pmatrix}. \tag{2.29}$$

The forward model of the radiative transfer equation is the function $\mathbf{F_b}$, where $\mathbf{b}$ is a vector of the atmospheric compensation parameters,

$$\mathbf{F_b}\left(\mathbf{X}\right) = \mathbf{Y}. \tag{2.30}$$

An approximate inverse, $\mathbf{G_{\hat{b}}}$, to the forward model inverts a noisy observed radiance vector $\mathbf{Y} + \eta$ to an estimated temperature and emissivity vector $\hat{\mathbf{X}}$, where $\hat{\mathbf{b}}$ is a vector of estimated atmospheric compensation parameters and η is the measurement error,

$$\mathbf{G_{\hat{b}}}\left(\mathbf{Y} + \eta\right) = \hat{\mathbf{X}}. \tag{2.31}$$

The estimated temperature and emissivity error is given by

$$\hat{\mathbf{X}} - \mathbf{X} = \mathbf{G_{\hat{b}}}\left(\mathbf{F_b}\left(\mathbf{X}\right) + \eta\right) - \mathbf{X}. \tag{2.32}$$

After adding zero to the right-hand side of equation 2.32 ($[\mathbf{G_b}\left(\mathbf{F_b}\left(\mathbf{X}\right)\right) - \mathbf{G_b}\left(\mathbf{F_b}\left(\mathbf{X}\right)\right)]$ and $[\mathbf{G_b}\left(\mathbf{F_b}\left(\mathbf{X}\right) + \eta\right) - \mathbf{G_b}\left(\mathbf{F_b}\left(\mathbf{X}\right) + \eta\right)]$), and rearranging the terms, the general error

model defined in terms of algorithmic, measurement, and parameter error is written as

$$
\begin{aligned}
\mathbf{\hat{X}} - \mathbf{X} = &[\mathbf{G_b}\left(\mathbf{F_b}\left(\mathbf{X}\right)\right) - \mathbf{X}] + \\
&\ldots \text{algorithmic error} \\
&[\mathbf{G_b}\left(\mathbf{F_b}\left(\mathbf{X}\right) + \eta\right) - \mathbf{G_b}\left(\mathbf{F_b}\left(\mathbf{X}\right)\right)] + \\
&\ldots \text{ measurement error} \\
&[\mathbf{G_{\hat{b}}}\left(\mathbf{F_b}\left(\mathbf{X}\right) + \eta\right) - \mathbf{G_b}\left(\mathbf{F_b}\left(\mathbf{X}\right) + \eta\right)] \\
&\ldots \text{ parameter error.}
\end{aligned}
\tag{2.33}
$$

The algorithmic error for ISSTES is the retrieval error for radiance measurements and atmospheric parameters that are error-free. The measurement error is the retrieval error due to the observed radiance with added noise. The parameter error is the retrieval error due to the estimated atmospheric compensation parameters **b** and measurement noise. The sensitivity of the ISSTES algorithm has only been evaluated for the algorithmic and the measurement error in the literature (Ingram and Muse, 2001).

The source of the algorithmic error is the smoothness assumption. The ISSTES algorithm was applied to 246 emissivity spectra from the Johns Hopkins University (JHU) spectral library resampled for a SEBASS sensor. Only one material, a marble/limestone sample, was found to have a significant algorithmic error of 3.43 K for temperature and a maximum emissivity error of 0.086 (Ingram and Muse, 2001). A histogram of the algorithmic error for temperature versus altitude is shown in Figure 2.6, and for emissivity in Figure 2.7. Both of the histograms exclude the marble/limestone sample. The histogram's spread in temperature error increases with altitude up to 2 km due to the increasing atmospheric effects, with similar results for the emissivity error.

An analytical model and a Monte Carlo simulation were used to estimate the standard
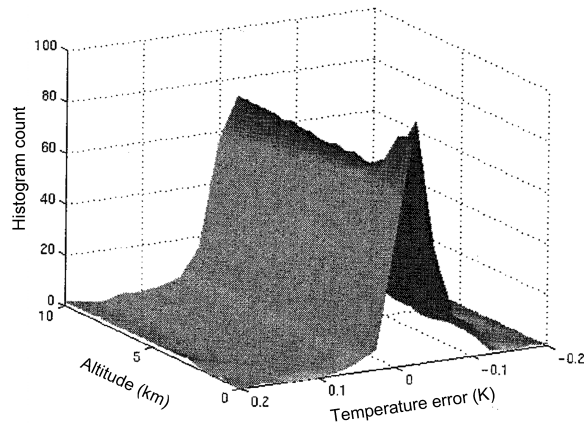
Figure 2.6: Histogram of algorithmic error in ISSTES for temperature error (-0.2 to 0.2 K) versus altitude (0-10 km) (Ingram and Muse, 2001)
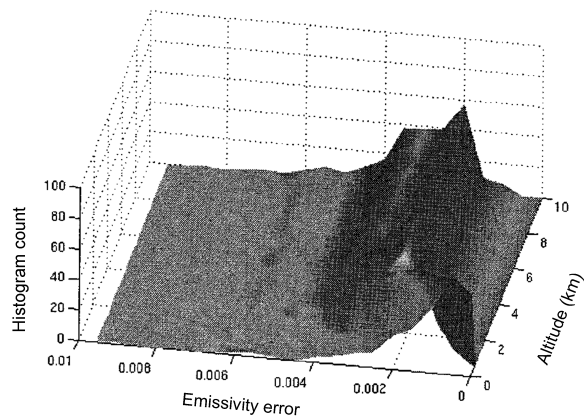
Figure 2.7: Histogram of algorithmic error in ISSTES for emissivity error (0 - 0.002) versus altitude (0-10 km) (Ingram and Muse, 2001)

deviation and bias for temperature and emissivity errors due to noise (Ingram and Muse, 2001). The results for temperature retrieval are shown in Figures 2.8 and 2.9. For ISSTES to retrieve approximately unbiased temperatures, the instrument noise levels should be below 1 μW/cm^2/sr/μm. The SEBASS sensor has a noise level of 0.6 μW/cm^2/sr/μm, giving a standard deviation of surface temperature of 0.18 K and a bias of 0.03 K (Ingram and Muse, 2001). The results for emissivity error show an increase in the magnitude of both the standard deviation and bias for wavelength regions with a relatively lower atmospheric transmittance, due to a loss of signal caused by increased atmospheric absorption (Ingram and Muse, 2001). Although the exact spectra were used for atmospheric compensation, the small errors in the retrieved temperatures resulted in small residual atmospheric features of water vapor, carbon dioxide, and ozone in the retrieved emissivity (Ingram and Muse, 2001).

When the atmospheric water vapor and temperature profiles are known, the atmospheric terms can be calculated with an accuracy limited by the radiative transfer model and the accuracy of the coefficients of the water vapor continuum and band absorptions (Wan and Li, 1997). However, temperature and water vapor profiles synchronized with the TIR image in both location and time may not be available. The alternative is to use a database of radiative transfer code runs to model the atmosphere. The automatic retrieval of temperature and emissivity using spectral smoothness (ARTEMISS) algorithm is a hybrid algorithm for atmospheric compensation based on the direct use of a database of MODTRAN runs as the compensation spectra (Borel, 2003). The ISAC results are used to select candidate atmospheric parameters from a look-up table (LUT) of MODTRAN atmospheric transmittance, upwelling radiance and downwelling radiance results for thousands of atmospheric conditions. The search is based on minimizing the spectral angle between the ISAC estimated transmittance and the MODTRAN LUT transmittance
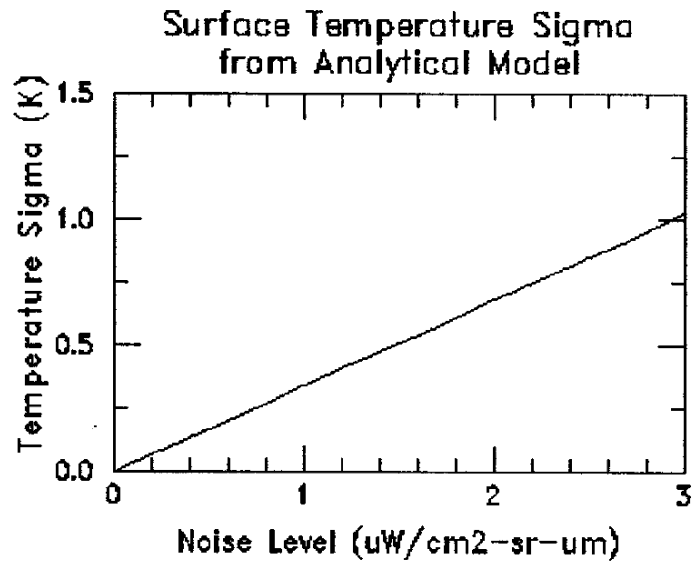
(a)
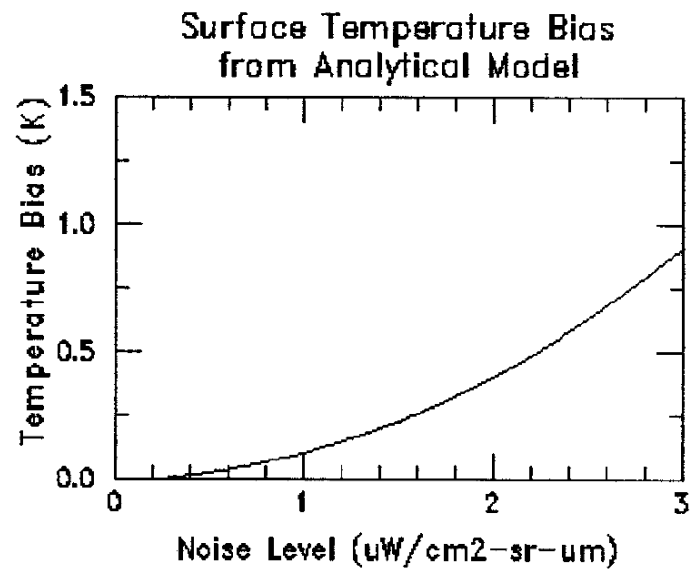
(b)

Figure 2.8: (a) Standard deviation of the estimated surface temperature using ISSTES (b) Bias of the estimated surface temperature using ISSTES (Ingram and Muse, 2001)

Analytical Estimate of Emissivity Sigma

(a)

Analytical Estimate of Emissivity Bias
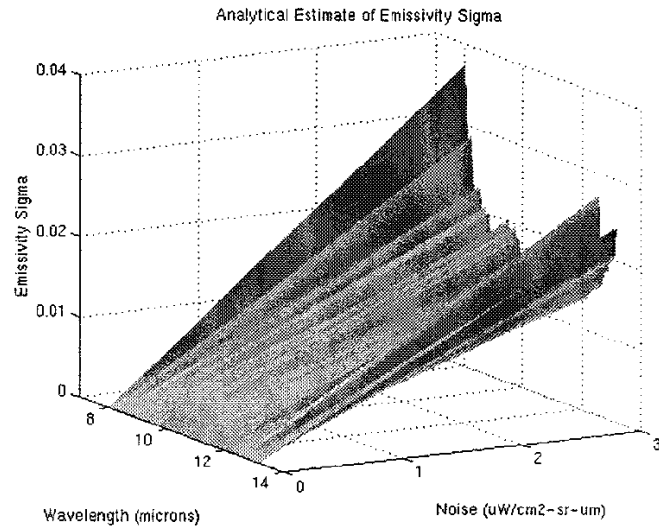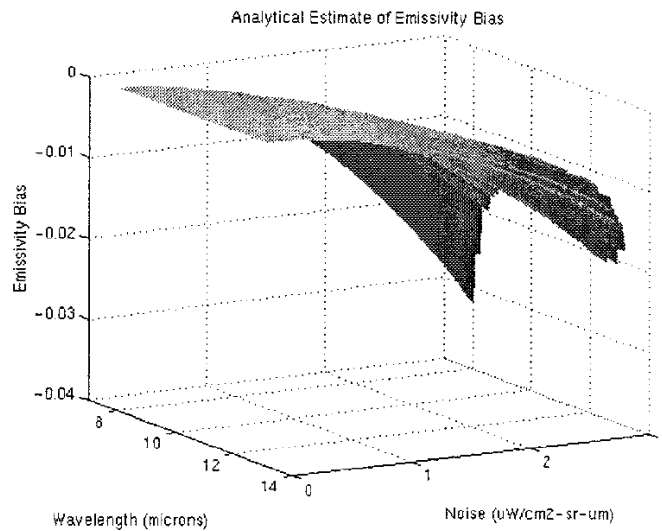
(b)

Figure 2.9: (a) Standard deviation of the estimated surface emissivity using ISSTES (b) Bias of the estimated surface emissivity using ISSTES (Ingram and Muse, 2001)

results. ISSTES is then run on each candidate atmosphere for a number of randomly chosen test pixels, and the candidate atmosphere with the smoothest ISSTES result is chosen. The atmospheric parameters from the chosen MODTRAN LUT are directly used to compensate the atmosphere and ISSTES is applied to all pixels to retrieve temperature and emissivity (Borel, 2003).

The ARTEMISS and OLSTER algorithms are currently the only ones in the literature that perform both atmospheric compensation and temperature and emissivity separation. The ARTEMISS algorithm is simple and fast, as well as applicable to both man-made and natural surface materials. However, the use of MODTRAN spectra directly as the compensation spectra may result in nonsmooth emissivity spectra due to spectral and radiometric calibration errors and sensor noise. In addition, published results using the ARTEMISS algorithm have been for synthetic data only.

2.2.5   ASSET

The automated separation of surface emissivity and temperature (ASSET) algorithm is a TES algorithm (Hayashi and Sharp, 2002). ASSET requires a separate input of atmospheric compensation parameters, as well as a library of material emissivities. For each image pixel, the algorithm computes N temperature vectors for N emissivities in the library. The emissivity that results in a retrieved temperature vector that is most invariant with wavelength is chosen, using standard deviation of the temperature vector as the criterion. The estimated temperature of the pixel is the mean of the temperature vector. The emissivity of the pixel is updated using the pixel temperature, and may differ from the library emissivity due to noise, mixed pixels, natural spectral variability, and inadequate atmospheric compensation (Hayashi and Sharp, 2002). The authors of ASSET point out that over or underestimating the magnitude of the emissivity introduces a slope into the

temperature vector due to the changing shape of the Planck function at different temperatures. This provides a potential method to improve the temperature and emissivity estimation.

2.2.6   Estimating Downwelling Radiance

The estimation of downwelling radiance is probably the most difficult part of the atmospheric compensation and surface parameter retrieval process. In order to estimate the downwelling radiance, the emissivities need to be determined. However, it is the emissivities, along with the LSTs, that the retrieval process is solving for. Rather than trying to directly estimate the downwelling radiance using a scene-derived method, it is more practical to use physics-based modeling to arrive at the estimate. The ARTEMISS algorithm applies a LUT of atmospheric spectra generated using MODTRAN. Another approach for estimating the downwelling radiance is based on expressing the downwelling radiance as a function of upwelling radiance. The method used by (Tonooka, 2001) in the gray-pixel (GP) algorithm is described below. The downwelling radiance is estimated as a quadratic function of the upwelling radiance at nadir view for each channel i using

$$L_i^{\downarrow} = a_i + b_i L_i^{\uparrow} + c_i L_i^{\uparrow 2}. \tag{2.34}$$

The regression coefficients $a_i, b_i,$ and c_i were determined using regression analysis of 964 atmospheric profiles. The root mean square errors (RMSEs) of the downwelling radiance estimated using equation 2.34 for ASTER's TIR channels 10 to 14 are 0.064, 0.038, 0.021, 0.031, and 0.034 W/m^2/sr/μm, respectively (Tonooka, 2001). A quadratic function is used to help account for nonlinearity. For view angles at other than nadir, the upwelling radiance at nadir view can be calculated from the estimated transmittance and
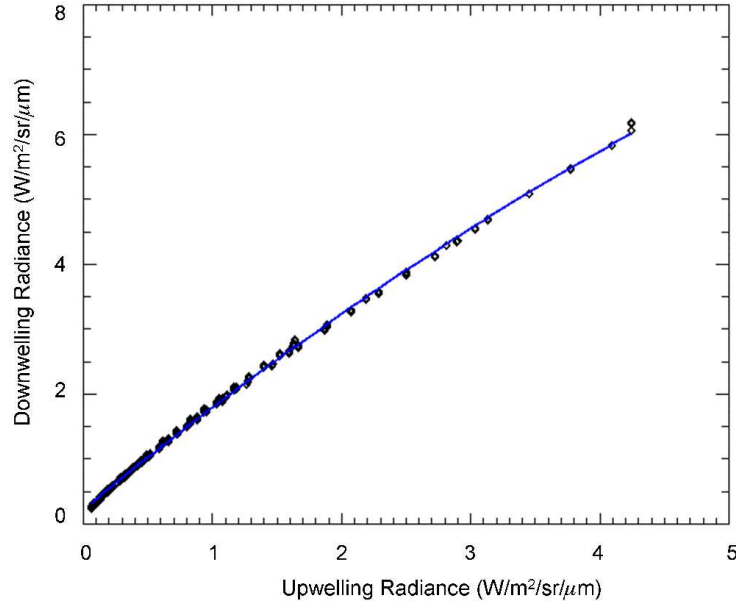
Figure 2.10: Downwelling radiance versus upwelling radiance for a SEBASS band at 9.07170 μm.

upwelling radiance with

$$L_i^\uparrow (\theta = 0) \cong L_i^\uparrow (\theta) \frac{1 - \tau_i (\theta)^{\cos \theta}}{1 - \tau_i (\theta)}, \tag{2.35}$$

assuming that the mean temperature is independent of θ (Tonooka, 2001).

As a simple test of the upwelling radiance to downwelling radiance relationship for this dissertation, 726 MODTRAN simulations were run using six standard MODTRAN atmospheric profiles, and 11 scaling variations of both ozone and water vapor. A plot of the downwelling radiance versus the upwelling radiance value for a particular SEBASS resampled band is shown in Figure 2.10. Second-degree polynomials were fitted for each band, and the coefficients were stored in a LUT. In practice, a different set of coefficients needs to be determined for a given sensor altitude.

2.2.7   Summary of the reviewed algorithms

A summary of the reviewed algorithms is given in Table 2.3. Of the atmospheric compensation and hybrid algorithms reviewed (ISAC, AAC, and ARTEMISS), the ISAC algorithm is the simplest and most widely applicable algorithm. The ISAC algorithm uses a data-derived approach, AAC is model-based, and ARTEMISS is a hybrid algorithm which uses the results from ISAC to select from a library of model-based results. The AAC algorithm offers no significant advantage over the ISAC algorithm, and it is more sensitive to spectral miscalibration issues. The main advantage of the ARTEMISS algorithm is that it accounts for $L_d(\lambda)$. However, as a result of using radiative transfer model results directly as the compensation spectra, it is sensitive to sensor noise and artifacts. The disadvantage of neglecting $L_d(\lambda)$ in the ISAC algorithm may be overcome by the use of a $L_d(\lambda)$ LUT as described in the GP algorithm. The error in estimating $L_d(\lambda)$ from $L_u(\lambda)$ at the edges of the TIR window and in the ozone region may be minimized by additional LUTs that vary the ozone and water vapor amounts in the radiative transfer modeling.

The approach for temperature/emissivity separation in ASTER's TES algorithm relies heavily on an empirical relationship that is limited to natural materials. The ASSET algorithm assumes that the materials in the scene are well represented by a library of emissivity spectra, and does not account for the spatial scaling issue between laboratory measurements and sensor data. The ISSTES algorithm is fast and simple, and like all the temperature/emissivity separation algorithms, it requires accurate atmospheric compensation spectra.

The approach presented in the next chapter is based on a hybrid of the ISAC, ISSTES, and $L_d(\lambda)$ LUT algorithms. A modification to the ISAC algorithm is needed to address the requirement that the image is dominated by blackbody features, and an iterative framework is necessary to adjust the initial estimated compensation spectra and

remove the blackbody assumption.

Table 2.3: Summary of the reviewed hyperspectral algorithms

Algorithm	Advantages	Disadvantages
ISAC	Data-derived approach for estimating $\tau(\lambda)$, $L_u(\lambda)$, and LST • insensitive to sensor calibration issues • produces smooth brightness temperature spectra	Requires an image dominated by black-bodies with a spread in LSTs • neglects $L_d(\lambda)$ • assumes a spatially homogeneous atmosphere over the sensor FOV
AAC	Model-based approach for estimating $\tau(\lambda)$ and $L_u(\lambda)$	Sensitive to sensor calibration issues • requires surface materials with a smooth and high emissivity near the water absorption band • neglects $L_d(\lambda)$ • assumes a spatially homogeneous atmosphere over local regions
ARTEMISS	Performs both atmospheric compensation and T/E separation • accounts for $L_d(\lambda)$ • fast and simple	Uses radiative transfer model results directly as the compensation spectra • sensitive to sensor noise and artifacts • assumes a spatially homogeneous atmosphere over the sensor FOV
$L_d(\lambda)$ LUT	Model-based estimation of $L_d(\lambda)$ from $L_u(\lambda)$	Large computational and storage overhead • separate LUT required for each sensor altitude • difficult to estimate $L_d(\lambda)$ in ozone and WV absorption regions
ASTER's TES	Simultaneous estimation of LST and LSE	MMD empirical relationship not applicable to man-made surfaces • assumes atmospherically compensated data and available $L_d(\lambda)$ estimate
ASSET	Based on a simple assumption of flat brightness temperature spectra using a library of material emissivities	Spatial scaling issue between laboratory emissivity measurements and sensor data • assumes the materials in the scene are well represented by the emissivity library • assumes atmospherically compensated data
ISSTESS	Simultaneous estimation of LST and LSE • data-driven approach • fast and simple	Errors in the estimated atmospheric spectra directly affect the smoothness assumption • assumes atmospheric compensation spectra are available

Chapter 3

Approach

3.1 Issues with current algorithms

The current algorithms in the literature can be classified into three categories: atmospheric compensation (ISAC, AAC), temperature / emissivity separation (ASTER TES, ISSTES, ASSET), and hybrid end-to-end algorithms (ARTEMISS). The atmospheric compensation techniques reviewed do not account for downwelling radiance. An empirical relationship based on radiative transfer modeling is used to scale relative values to absolute atmospheric transmittance and upwelling radiance (ISAC) or to estimate the atmospheric terms from the transmittance ratio and path radiance difference (AAC). ISAC requires a scene dominated by near-blackbody features, and any errors caused by the unaccounted reflected downwelling term will carry over to the retrieved atmospheric terms (Young et al., 2002). AAC requires a scene with surfaces that have a smooth and high emissivity near the water absorption band. This assumption means that AAC does not work well for man-made surfaces.

All of the reviewed temperature / emissivity separation algorithms assume that the at-
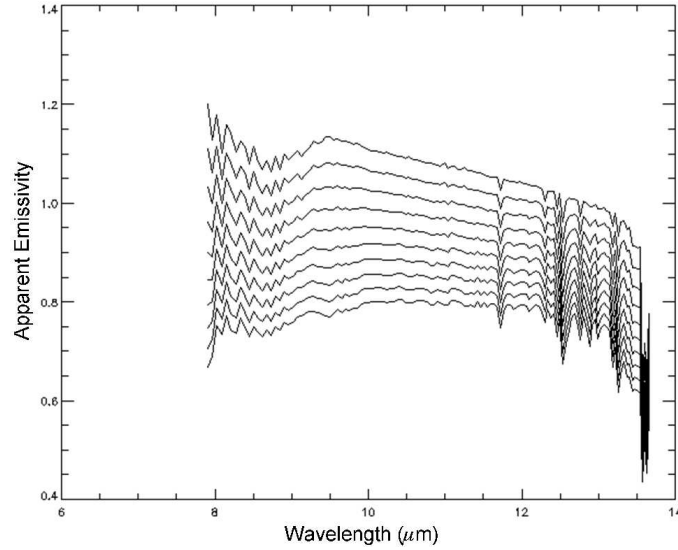
Figure 3.1: ISSTES for a stressing case, $\triangle T_s = 2$ K.

mosphere has been compensated for already by using the surface-leaving radiance as their input. The performance of ASTER's TES algorithm depends largely on the empirical relationship between the minimum emissivity and its maximum-minimum difference. This relationship does not apply to man-made surfaces. The smoothness assumption is used in both ISSTES and ASSET, but in different ways. ISSTES is an iterative search for the smoothest retrieved emissivity related to varying the LST estimate, while ASSET applies a library of spectral emissivities to each pixel and assigns it the emissivity corresponding to the smoothest brightness temperature vector. The ISSTES algorithm is a simple and effective approach for temperature / emissivity separation. However, like the rest of the algorithms in this category, its performance is limited by the accuracy of the atmospheric compensation performed externally. An example of the effects of improper atmospheric compensation on the ISSTES algorithm is shown in Figure 3.1. The family of curves represents a variation of the LST estimate by 2 K. When the estimated atmospheric pa-

rameters are incorrect, the ISSTES algorithm may fail. In this case, none of the possible ISSTES emissivities are correct as they contain residual atmospheric effects. While the emissivities may be spectrally smoothed using polishing or other methods, the computed spectral smoothness for a given temperature may not correspond to the correct LST.

The ISSTES algorithm is used in ARTEMISS for temperature / emissivity separation, and its performance will be limited by the accuracy of the atmospheric compensation. The ARTEMISS approach to atmospheric compensation uses a radiative transfer code (RTC). The main advantage of RTCs is that a wide variety of conditions can be simulated by varying the atmospheric conditions (Prata et al., 1995). The disadvantage is that the characterization of the instrument's spectral filter function must be accurate. A spectral misregistration can amplify the effects of the atmosphere on the surface emission spectrum. The results are model dependent and are based on correlations that may not exist in the atmosphere (Young et al., 2002). The accuracy of RTCs is limited by assumptions used to calculate line parameters. Some molecular absorption line parameters are still not precisely known, and not all of the molecular species are taken into account by the models. CFCs are rarely taken into account because no detailed description is available (Prata et al., 1995). A precise calculation of the radiative transfer requires an accurate knowledge of the atmospheric structure.

3.2   Assumptions

In order to regularize the retrieval problem, it is necessary to simplify the problem and constrain the parameters with some assumptions. These assumptions are summarized in Table 3.1.

In addition to the N spectral emissivities plus one surface temperature to solve for

Table 3.1: Assumptions in the approach

- Spatially homogeneous atmosphere over the image
- The estimated atmospheric compensation spectra is only applicable
  to the same image used to derive them
- Solar contribution is negligible in the TIR
- No clouds in the image, or a cloud mask is available
- No emission sources reflected into line of sight
  (such as clouds, buildings, trees)
- Flat surface (geometrical effects of the surface and elevation are ignored)
- Lambertian surface
- Near-nadir sensor viewing angle (view angle $\leq 30\,°$)
- Near-blackbody features are available in the image,
  with a spread in surface temperatures
- No mixed pixels
- The mean value of the $\overline{\tau(\lambda)L_d(\lambda)}$ term in the RTE is approximated by
  the product of the mean values of $\tau(\lambda)$ and $L_d(\lambda)$

---

per pixel with N spectral measurements, the atmospheric compensation spectra must also be estimated. This effectively means that $4N + 1$ values must be solved per pixel given N spectral measurements. The assumption of a spatially homogeneous atmosphere over the image allows the same atmospheric spectra $\tau(\lambda)$, $L_u(\lambda)$, and $L_d(\lambda)$ to be applied to every pixel in the image. This assumption greatly reduces the number of values to solve for. The appropriateness of the assumption will depend on the atmospheric stability over the sensor FOV. A non-uniform atmosphere may require a segmentation of the image into locally uniform atmospheric regions similar to the approach used in the AAC algorithm. However, the resulting LST and LSE maps may exhibit artificial discontinuities around the borders of the segments. Each image segment may also have a smaller range of surface temperatures that increases the difficulty of estimating the atmospheric spectra.

The estimated atmospheric spectra $\tau(\lambda)$, $L_u(\lambda)$, and $L_d(\lambda)$ are representative of the

atmosphere only for the image data from which they were derived. The primary objective of the retrieval algorithm is to estimate the land surface parameters of temperature and emissivity. The estimated atmospheric spectra are intended only to compensate for atmospheric effects as necessary for the model to fit the observed radiance data. In other words, the estimated atmospheric spectra may not necessarily agree with a radiative transfer code result using real atmospheric profile soundings for the same image data.

In the 8 - 14 μm TIR spectral region, the surface emitted radiance dominates the solar reflected component. The RTE used in the retrieval model is simplified by neglecting the solar component. Scattering effects are also neglected, assuming no volcanic eruptions are nearby.

The assumption of a cloud-free sky is important for land surface parameter retrieval in the TIR. In addition to violating the assumption of a spatially homogeneous atmosphere over the image, clouds are also a source of radiation that can be reflected from the land surface towards the sensor. The retrieval model does not account for other emission sources, such as buildings or trees, that are reflected into the sensor line of sight in order to avoid complex geometric modeling specific to each image. The impact of neglecting emission sources that are reflected towards the sensor depends on the temperature of the source and the emissivity of the reflecting surface. The retrieval error will be largest for sources that are hotter than the surrounding land surface reflecting off a low emissivity surface into the sensor line of sight.

A flat land surface is assumed to avoid complex geometric modeling when no *a priori* information is available on the surface structure and elevation. It is assumed that the atmospheric path difference due to a change in elevation within the image is negligible, or that the image can be segmented into regions of constant elevation. Plowed fields, forest canopies, and sloped surfaces are some examples of where a flat surface assumption may
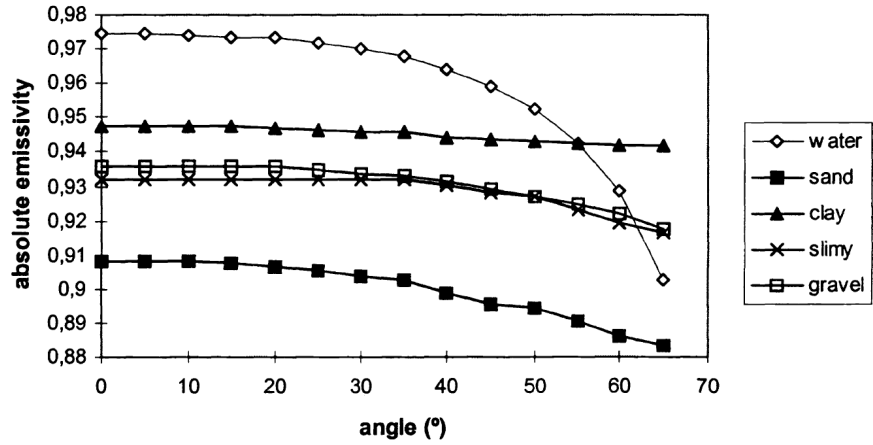
Figure 3.2: The angular variation of emissivity for various materials in the TIR. (Sobrino et al., 1998)

fail. The retrieved emissivities from these surfaces may not match laboratory measurements (leaf measurements for a forest canopy), or even the retrieved emissivity for the same material in the image with a different geometric structure. However, the estimated effective emissivity may be useful enough for material classification.

The RTE model assumes that the land surface is flat and opaque, and that it approximates a Lambertian reflector of the downwelling radiance. The Lambertian assumption simplifies the model by avoiding geometric calculations. The assumption does not hold for surfaces such as dry grass, yellow loamy sand, slate stone shingle, and white marble (Dash et al., 2002). The emissivities for most materials in the TIR have a decreasing trend with increasing view angles. The angular dependence of the surface emissivity for various materials in the 8 - 14 μm spectral window is shown in Figure 3.2. In general, the Lambertian assumption for surfaces is valid for near-nadir conditions (view angle $\leq$ 30 $^\circ$).

The assumption that blackbody features (emissivities with little spectral contrast and

values from about 0.97 to 1.00) are available in the image data is useful for regularizing the retrieval problem. The assumption simplifies the estimation of the atmospheric $\tau(\lambda)$ and $L_u(\lambda)$ spectra using the image pixels where the reflected downwelling radiance component is minimal by linearizing the RTE. A sufficient spread in surface temperatures is required to avoid an unstable linear regression when estimating the atmospheric $\tau(\lambda)$ and $L_u(\lambda)$ spectra. Compared to the ISAC algorithm, the retrieval model used here does not require that blackbody features dominate the image because the downwelling radiance and emissivity values are eventually estimated for each pixel.

Spectrally pure image pixels are assumed in the absence of sub-pixel temperature and emissivity information. The effect of mixed pixels will depend on the sensor resolution and the variability of the land surface. Finally, the mean value of the $\overline{\tau(\lambda)L_d(\lambda)}$ term in the RTE is approximated by the product of the mean values of $\tau(\lambda)$ and $L_d(\lambda)$. The high degree of correlation between the $\tau(\lambda)$ and $L_d(\lambda)$ spectra, along with the spectral resolution of a hyperspectral sensor that may not be able to resolve the atmospheric absorption or emission lines, combine to affect the accuracy of the approximation (Young et al., 2002). The error in the approximation has not been quantified for the $\overline{\tau(\lambda)L_d(\lambda)}$ term.

3.3   Approach (OLSTER)

In general, solutions to the retrieval of surface parameters can be non-unique and unstable. Non-unique solutions occur when different combinations of the surface and atmospheric parameters produce the same observation. The direct approach to surface parameter retrieval is not practical given the ill-posed nature of the problem. Solving for the exact solution in the presence of measurement noise can lead to unstable solutions. Instead, a
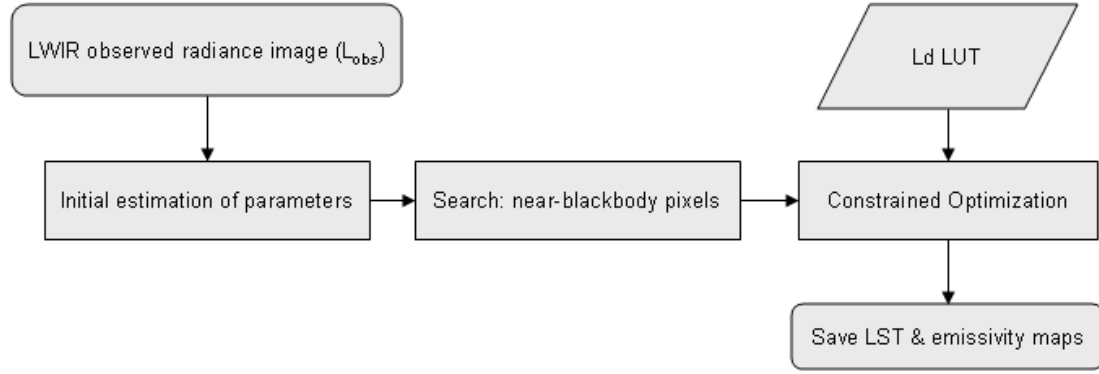
Figure 3.3: The main steps of the OLSTER algorithm

set of possible solutions should be determined, and constraints can be applied to obtain the optimal solution. The approach developed here, optimized land surface temperature and emissivity retrieval (OLSTER), uses an iterative technique to solve the nonlinear retrieval problem. The OLSTER algorithm introduces a new method for finding near-blackbody pixels based on scene-derived methods, and also an iterative method for retrieving surface parameters using constrained optimization. Unlike the temperature / emissivity separation methods in the literature, this approach does not assume that perfect atmospheric compensation has been performed during preprocessing, and does not require spectral polishing of retrieved emissivities. The main steps include initialization, a search for near-blackbody pixels, and an iterative constrained optimization, shown in Figure 3.3. The following subsections provide more detail on each of the steps in the OLSTER approach.

3.3.1 Initialization

The initialization step of the OLSTER algorithm is based on the ISAC algorithm. An in-scene approach is appropriate at this starting point given the lack of knowledge of surface

and atmospheric parameters. The purpose of this step is to provide an initial estimate of the atmospheric transmittance and upwelling radiance. The details of the initialization step are given in Table 3.2.

The first step is to convert observed radiance (L_{obs}) to brightness temperature. The most–hits band or reference wavelength is defined as the band with the highest brightness temperature total for all pixels. The brightness temperature at the reference wavelength is the initial LST estimate for each pixel. The LST estimate is used to calculate the Planck blackbody radiance (L_{bb}) per pixel. A least-squares regression of L_{obs} versus L_{bb} for each band is performed, with the slope and intercept as the initial estimates for unscaled atmospheric transmittance and upwelling radiance, respectively. Only the pixels with a maximum brightness temperature at the reference wavelength are included in the scatter plot.

The departure from the ISAC approach here is that a linear least-squares regression is used instead of fitting a line to the upper edge of each L_{obs} vs. L_{bb} scatter plot. The points at the top edge of the scatter plot may not necessarily represent near-blackbody pixels if there are large errors in the estimated LST which leads to a large error in the calculated L_{bb}.

The ISAC algorithm also assumes a scene dominated by blackbody pixels. The ISAC atmospheric parameter results for image data with scenes that do not meet this assumption will provide a poor starting point for the OLSTER algorithm. A solution for this case is to remove low-emissivity pixels (step 3 in Table 3.2) before estimation of the atmospheric parameters. The low-emissivity pixels are determined using the shape and range of values of the mean-removed brightness temperatures. Near-blackbody pixels are assumed to have a relatively flat mean-removed brightness temperature, and therefore pixels with a range of mean-removed brightness temperature values greater than the median for the

image are removed. In general, determining whether or not a scene requires this step is difficult. In practice, the OLSTER algorithm should run the image data for both cases sequentially and compare the final objective function values at the end to determine which case to use.

Another difference from the ISAC algorithm is that the atmospheric parameters are not scaled based on MODTRAN runs, radiosonde data, or water vapor absorption bands. The estimated transmittance is rescaled to have values smaller than one using

$$\hat{\tau}(\lambda) = \frac{\hat{\tau}'(\lambda)}{\hat{\tau}'(\lambda)\mid_{max}} 0.999, \tag{3.1}$$

and the estimated upwelling radiance is iteratively rescaled to have nonnegative values using

$$\hat{L}_u(\lambda) = \hat{L}'_u(\lambda) + \left(\frac{\text{abs}(\hat{L}'_u(\lambda)\mid_{min})}{\text{max}(\hat{L}'_u(\lambda)\mid_{anti-corr}) + 1} \right) \hat{L}'_u(\lambda)\mid_{anti-corr}, \tag{3.2a}$$

$$\hat{L}'_u(\lambda)\mid_{anti-corr} = 1 - \frac{\hat{L}'_u(\lambda)}{\hat{L}'_u(\lambda)\mid_{max}}, \tag{3.2b}$$

where terms with a prime represent unscaled estimates, and where max denotes the maximum value over all spectral channels.

The spectral scaling equations were modified from (Young et al., 2002), but do not scale to known values for a single spectral band or the water vapor absorption band. The scaling approach that is used here rescales the atmospheric parameters if necessary to ensure physical values. The atmospheric parameters are then further refined in an iterative optimization step described later in subsection 3.3.4. The scaling value of 0.999 in equation 3.1 was chosen based on the requirement of a maximum atmospheric transmittance value of one and to avoid a slow convergence in the optimization step. The iterative addi-

Table 3.2: Initialization of the OLSTER algorithm

1.	Compute the brightness temperature spectrum per pixel, $T_B(L_{obs}(x,\lambda),\lambda)$
2.	Estimate $\hat{T}_s(x)$ per pixel using $T_B(L_{obs}(x,\lambda),\lambda)\mid_{max}$
3.	Remove low-emissivity pixels using the shape of $T_B(L_{obs}(x,\lambda),\lambda)$, if necessary
4.	Compute the Planck radiance per pixel, $\hat{L}_{BB}(\hat{T}_s(x),\lambda)$
5.	Estimate the $\hat{\tau}(\lambda)$ and $\hat{L}_u(\lambda)$ spectra via $L_{obs}(\lambda)$ versus $\hat{L}_{BB}(\lambda)$ linear regressions; $\hat{\tau(\lambda)}$ = slope, and $\hat{L}_u(\lambda)$ = intercept
6.	Rescale $\hat{\tau}(\lambda)$ and $\hat{L}_u(\lambda)$ to be physical, if necessary

tion of the anti-correlated estimated upwelling radiance (equation 3.2b) to the estimated upwelling radiance in equation 3.2a primarily adjusts low upwelling radiance values. The anti-correlated estimated upwelling radiance is similar to the estimated atmospheric transmittance. This approach is preferred to adding a constant bias to the estimated upwelling radiance, which may reduce the estimated transmittance values in later steps if a large bias is required for a nonnegative upwelling radiance estimate.

3.3.2   Search for near-blackbody pixels

The estimation of the atmospheric transmittance and upwelling radiance is complicated by the reflected downwelling radiance term in the radiative transfer equation and by the attenuation of the surface emitted radiance by emissivity. However, for near-blackbody pixels, the reflected downwelling radiance is small compared to the at-sensor radiance, and the surface emitted radiance is closely approximated by L_{bb}. These two properties motivate the search for the near-blackbody pixels to improve the estimation of the atmospheric parameters.

This step of the approach simply classifies the image pixels as either near-blackbody or lower-emissivity pixels recursively until a stopping condition is satisfied. The details

of this step are given in Table 3.3. The spectral shape of L$_{obs}$, compensated with the estimated atmospheric transmittance and upwelling radiance and converted to brightness temperature, is key to the classification. Ideally, the brightness temperature should be spectrally flat for every pixel if the estimated atmospheric parameters are correct and if the spectral emissivities were all constant and equal to one. In practice, the result of the atmospheric compensation is that some pixels are overcompensated, and some undercompensated. The pixels that are best compensated have emissivities that approximate the mean emissivity value of the scene, and are characterized by a relatively flat, mean-removed, atmospherically compensated brightness temperature, $T_B\left(\frac{L_{obs}(x,\lambda)-\hat{L}_u(\lambda)}{\hat{\tau}(\lambda)}, \lambda\right)$. Since the initialization step assumes blackbody pixels, the atmospheric parameters from the least-squares regression on the scatter plots of L$_{obs}$ versus L$_{bb}$ will compensate the pixels with the mean scene emissivity best. An example of this is shown in Figure 3.4. A test image of 1000 pixels with a temperature range of 270 K to 310 K and graybody emissivities from 0.9 to 1 was created to test the search for near-blackbody pixels. After estimating the atmospheric transmittance and upwelling radiance in the initialization step, the observed radiance was compensated with the estimated atmospheric parameters, converted to brightness temperature and its mean subtracted. A random sample of seven pixels from the test image was chosen for display purposes. The mean-removed spectral brightness temperature that is flat with values near zero is for a graybody emissivity of about 0.95. The near-blackbody pixels have a concave down shape, and the graybody pixels with an emissivity of about 0.9 have a concave up shape. The approach used to determine the concavity of each mean-removed, atmospherically compensated brightness temperature is to take its second derivative with respect to the wavelength of each spectral channel, and then average the second derivative values over all the bands.

Classification of near-blackbody pixels based on concavity in one iteration is not

Table 3.3: Method for classifying near-blackbody and lower-emissivity pixels

1. Compensate $L_{obs}(x, \lambda)$ with $\hat{\tau}(\lambda)$ and $\hat{L}_u(\lambda)$ from the modified ISAC algorithm and convert to brightness temperature, $T_B(\frac{L_{obs}(x,\lambda) - \hat{L}_u(\lambda)}{\hat{\tau}(\lambda)}, \lambda)$

2. Compute the concavity and correlation with $\hat{\tau}(\lambda)$ metrics on the mean-removed brightness temperatures

3. Classify pixels with positive correlation and negative concavity metrics as near-blackbody pixels, and the remaining pixels as low-emissivity

4. Update the $\hat{T}_s(x)$ and $\hat{L}_{BB}(\hat{T}_s(x), \lambda)$ for the near-blackbody pixels with $\hat{T}_s(x)$ set equal to the maximum compensated brightness temperature, $T_B(\frac{L_{obs}(x,\lambda) - \hat{L}_u(\lambda)}{\hat{\tau}(\lambda)}, \lambda)$

5. Update the $\hat{\tau}(\lambda)$ and $\hat{L}_u(\lambda)$ spectra using $L_{obs}(\lambda)$ versus $\hat{L}_{BB}(\hat{T}_s(x), \lambda)$ linear regressions on the near-blackbody pixels

6. Go to step 1 until the stopping conditions are satisfied
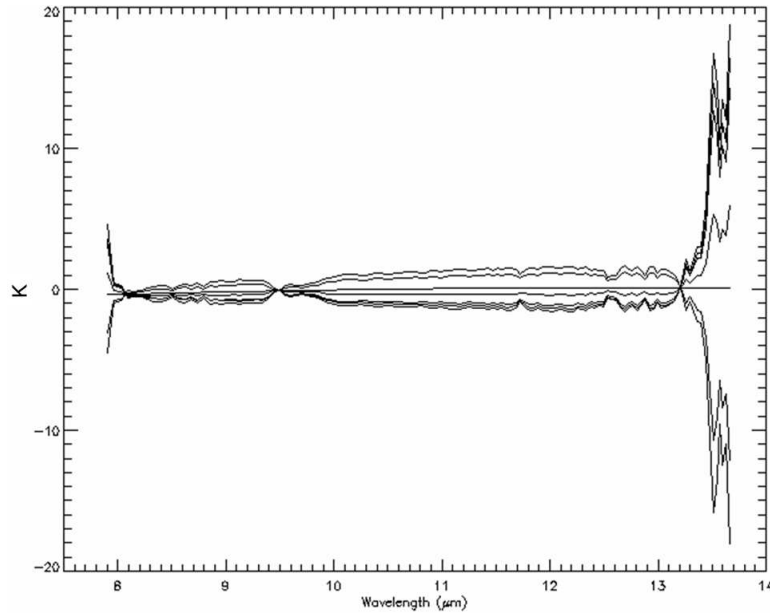
Figure 3.4: Mean-removed $T_B(\frac{L_{obs}(x,\lambda) - \hat{L}_u(\lambda)}{\hat{\tau}(\lambda)}, \lambda)$ spectra for graybody pixels with emissivities from 0.9 to 1.0. The blackbody pixels have a concave down spectra, the low emissivity pixels are concave up, and the pixels with an emissivity of 0.95 are spectrally flat.

straightforward. A plot of mean emissivity, averaged over 8 - 14 μm, versus concavity of the mean-removed brightness temperature after atmospheric compensation for graybody pixels is shown in Figure 3.5. The pixels with the scene average emissivity of 0.95 roughly have zero concavity. The higher emissivity pixels are more scattered due to errors in the estimated LSTs and atmospheric parameters. Instead of classifying near-blackbody pixels, the low emissivity pixels should be removed from the working set of pixels iteratively. Pixels with a positive concavity are classified as lower-emissivity pixels, and the rest are near-blackbody pixels. Then the LSTs of the near-blackbody pixels are updated by using the atmospheric parameter estimates, $\hat{\tau}(\lambda)$ and $\hat{L}_u(\lambda)$, for compensation (step 4 in Table 3.3). This updates L_{bb} for estimating the atmospheric parameters in a modified ISAC step, and the process repeats until a certain number of near-blackbody pixels remain. The iterations should be stopped when there are no further changes in the estimated atmospheric parameters or $\hat{T}_s$, the range of $\hat{T}_s$ values is determined to be too small, or when a certain percentage of the total pixels in the TIR image remain. The current implementation stops the iterative search when less than ten percent of the total number of pixels in the image remain in the near-blackbody pixels set. In general, the shape of the mean emissivity versus brightness temperature concavity scatter plot remains the same for each iteration, except that the range of emissivities is reduced for each iteration.

In addition to the concavity metric used to classify near-blackbody and lower-emissivity pixels, another metric based on the correlation between the estimated atmospheric transmittance and the spectral brightness temperature can be used. It is similar to concavity in that it classifies the pixels based on the spectral shape of the spectral brightness temperature. Since the low emissivity pixels have an atmospherically compensated and mean-removed spectral brightness temperature with a concave up shape, a negative correlation between the estimated atmospheric transmittance and the spectral brightness temperature
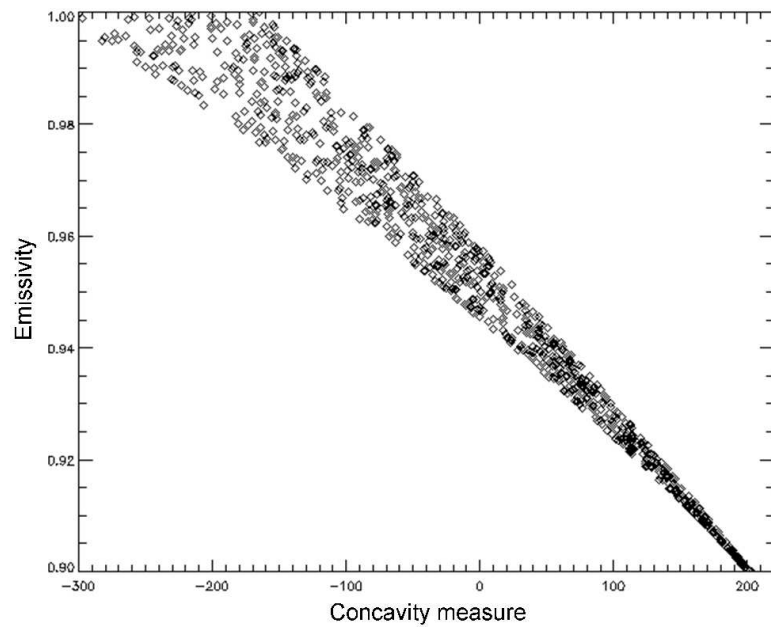
Figure 3.5: Emissivity value vs. concavity that is used to iteratively remove the lower-emissivity emissivity pixels (positive concavity).
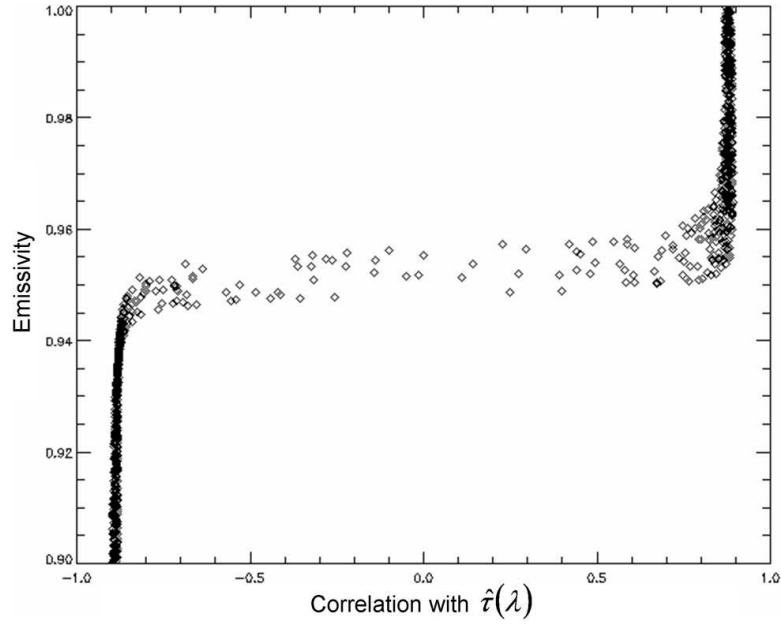
Figure 3.6: Graybody emissivity versus correlation with $\hat{\tau}(\lambda)$.

can be used to classify lower-emissivity pixels. An example for the graybody emissivity synthetic scene is shown in Figure 3.6. The approach in the OLSTER algorithm uses both concavity and correlation metrics to classify the image pixels. Pixels with both positive correlation and negative concavity metrics are classified as near-blackbody pixels, and the remaining pixels are classified as low-emissivity. The use of both metrics allows for a more robust classification than is possible with only a single metric.

The search for near-blackbody pixels was also tested using emissivities from the ASTER spectral library instead of graybodies. A synthetic image was created with 11,850 pixels and LSTs from 260K to 320K. A plot of the average emissivity over the LWIR window versus concavity of the mean-removed brightness temperature after atmospheric compensation is shown in Figure 3.7. A similar plot for average emissivity over the LWIR window versus the correlation with the estimated atmospheric transmittance is shown in

Figure 3.8. The following describes both figures. All 11,850 pixels are plotted in the upper left. At each iteration, all pixels with a positive concavity and a negative correlation are classified as lower-emissivity pixels. After one iteration, the number of near-blackbody pixels was reduced to 5,898, shown in the upper right plot. The rest of the pixels were labeled as lower-emissivity pixels. The next iteration reduced the number of near-blackbody pixels to 1,661, shown in the lower left plot, and the last iteration had 1,080 near-blackbody pixels, shown in the lower right plot. A further iteration reduced the number of near-blackbody pixels to 380, and is not shown. The pixels classified as lower-emissivity at each iteration were generally the same using either concavity or correlation, except for about four or five pixels, for this particular test image.

Even for perfect blackbody pixels, the estimated atmospheric transmittance and up-welling radiance will not be correct unless the transmittance is one and the upwelling radiance is zero for at least one band. Any influence from the atmosphere will result in an error in the estimation of LST when the observed radiance is converted to brightness temperature. This in turn leads to inaccuracies in L_{bb} used to estimate the atmospheric parameters in the regression. A constrained optimization approach that includes the down-welling radiance is used to overcome this problem.

3.3.3   Downwelling radiance

Plots of downwelling radiance versus upwelling radiance for six bands are shown in Figure 3.11. The effect of ozone variation is seen for the band at 9.44 μm. A separation of the six default MODTRAN atmospheres is seen for the band at 7.90 μm, and for other bands at the edge of the LWIR window, which are not shown. A separate LUT for each model atmosphere is used to avoid errors in predicting downwelling radiance from upwelling radiance.
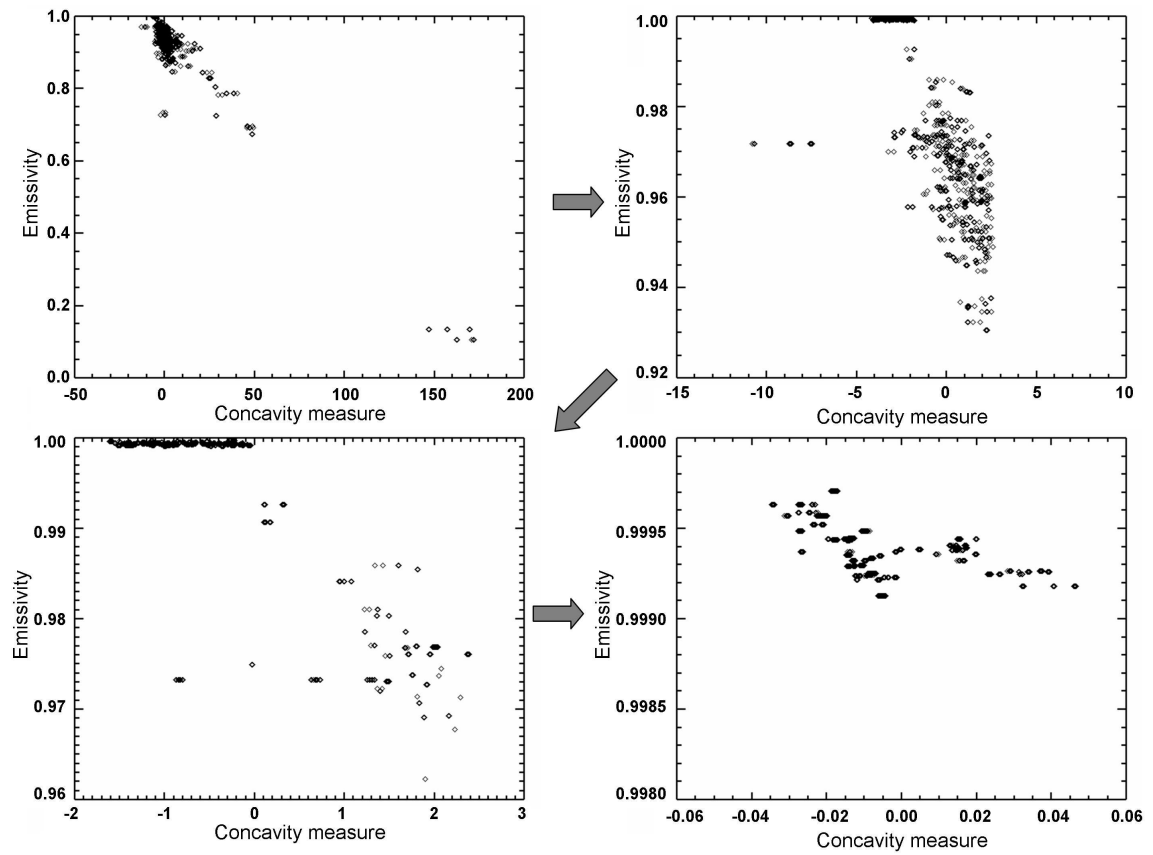
Figure 3.7: Search for near-blackbody pixels on ASTER's spectral library of emissivities using concavity.
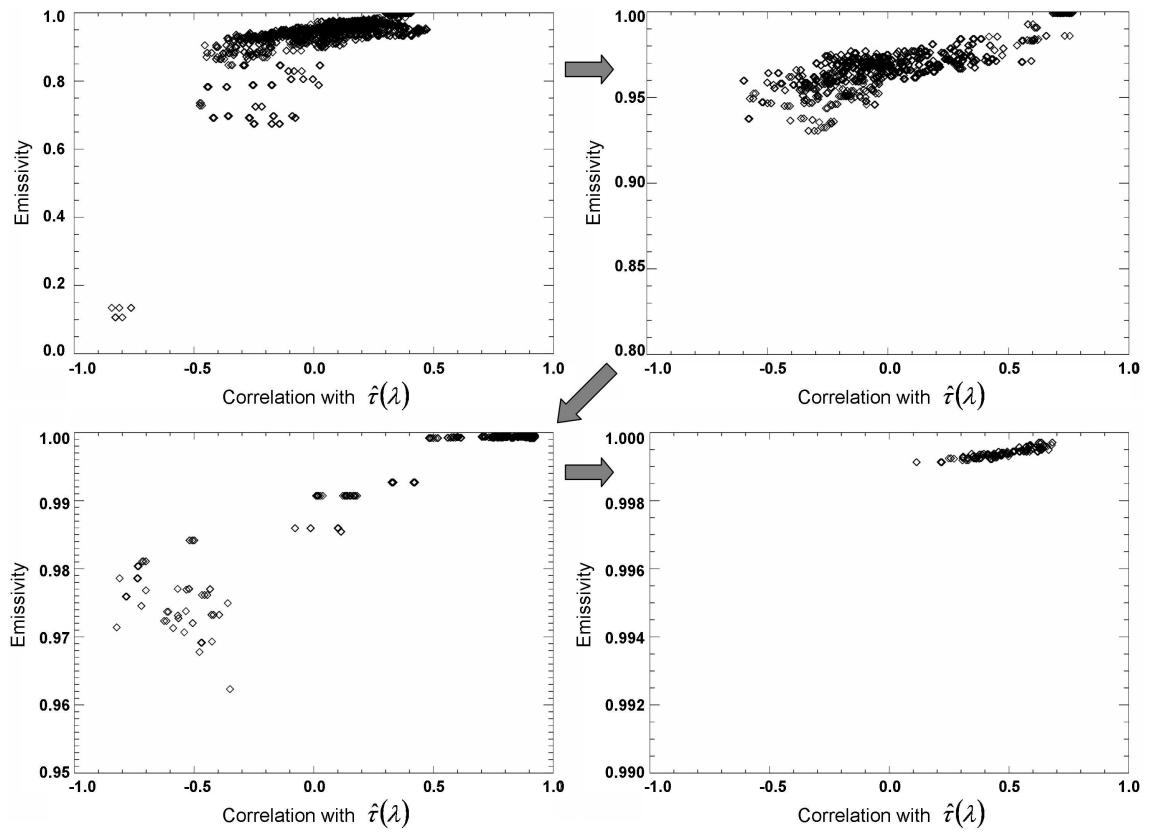
Figure 3.8: Search for near-blackbody pixels on ASTER's spectral library of emissivities using correlation with $\hat{\tau}(\lambda)$.

Six downwelling radiance lookup tables for the sensor altitude of 2km and nadir view were created for the synthetic image with ASTER library emissivities. The estimated physically-scaled upwelling radiance for the near-blackbody pixels are used to estimate downwelling radiance via stored LUTs of regression coefficients. Each LUT was used to predict a downwelling radiance, and the RTE was solved for emissivity on the near-blackbody pixels. The selection of one of the six LUTs to use is based on the maximum to minimum difference of the estimated emissivities $[\hat{\varepsilon}(x,\lambda) \mid_{max} - \hat{\varepsilon}(x,\lambda) \mid_{min}]$. The LUT resulting in the smallest maximum to minimum difference for the near-blackbody pixels is chosen.

OLSTER is currently using sixty six downwelling radiance lookup tables for the sensor altitudes of 2, 6, and 10km at nadir view. There are eleven ozone and eleven water vapor scaling factors from 0.4 to 2.4 in 0.2 increments used to vary the ozone and water vapor amounts. The locations of the radiosonde launches are shown in Figure 3.9, and the range of temperature and water vapor values are shown in Figure 3.10. Worldwide radiosonde data and the MODTRAN default profiles are used to create the LUTs. The range of corresponding upwelling radiance values are also stored with the LUTs, and are used to select a set of LUTs. The set is further reduced to five LUTs by computing the corresponding emissivity spectra for each LUT and selecting the five LUTs with the smallest maximum to minimum difference for the near-blackbody pixels. Each of the five LUTs will be tested sequentially in the optimization loop before selecting the final LUT.

3.3.4 Optimization of the atmospheric parameters

After predicting the downwelling radiance using the LUT of regression coefficients, initial estimates of the atmospheric parameters are available. The remaining parameter to estimate is the spectral emissivity per pixel. The RTE can be solved for emissivity using
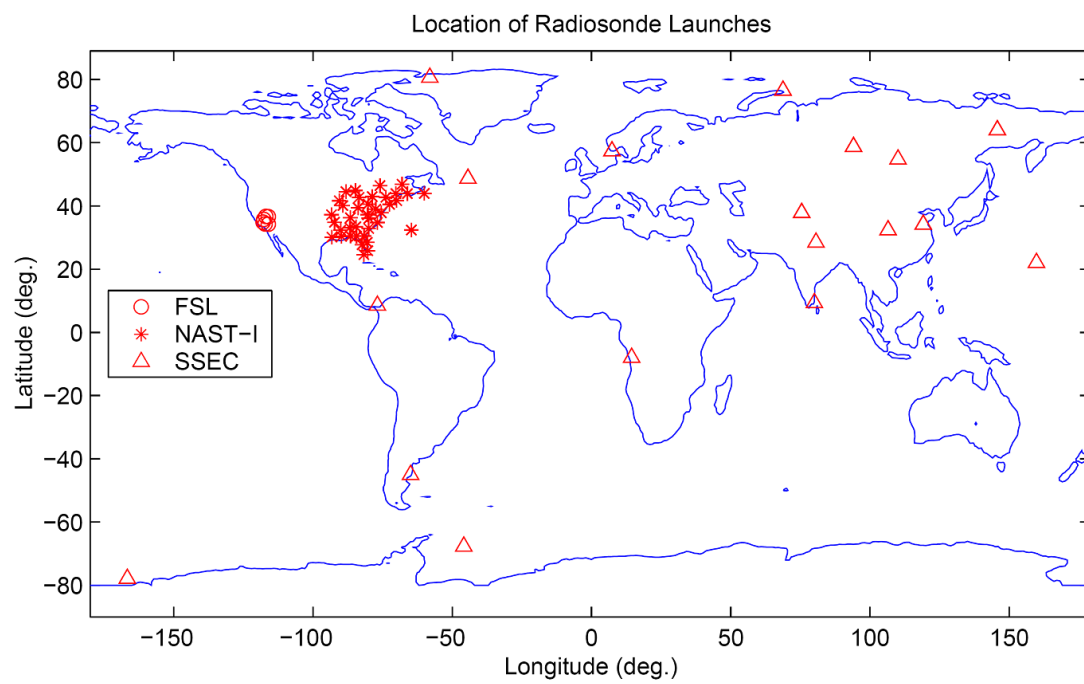
Figure 3.9: Location of radiosonde launches (Hernandez-Baquero, 2000).
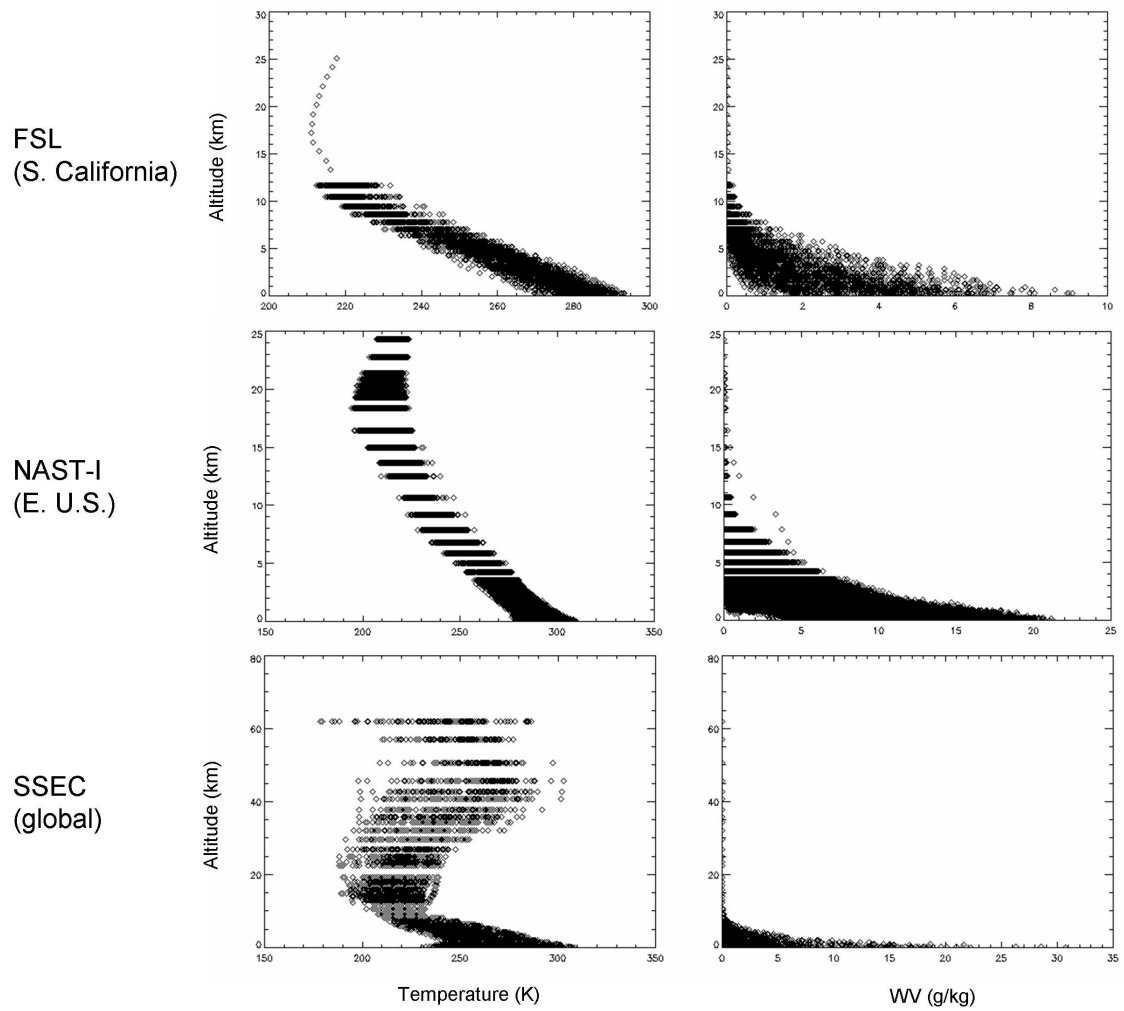
Figure 3.10: Range of temperature and water vapor values for the radiosondes.
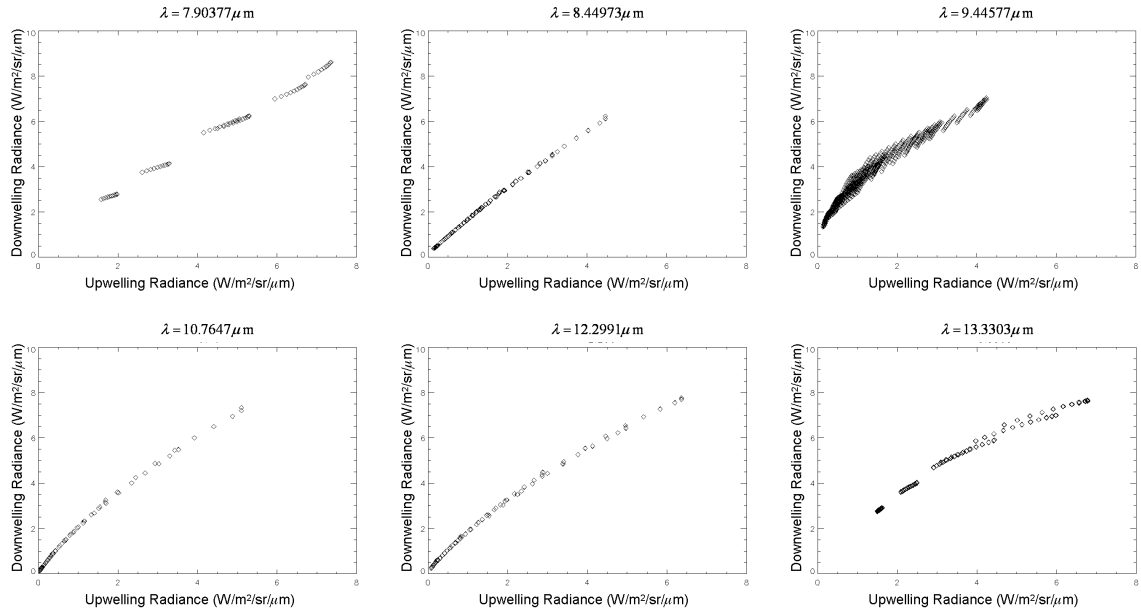
Figure 3.11: Downwelling radiance versus upwelling radiance ($W/\text{m}^2/\text{sr}/\mu$m) for the indicated bands.

the LSTs estimated from brightness temperature, which will result in values close to one. This is expected because blackbody surfaces have been assumed so far. A procedure is required to adjust the atmospheric parameters in order to move away from the blackbody assumption. The method used in this approach is to iteratively optimize the atmospheric transmittance and upwelling radiance. After each optimization, the estimates for downwelling radiance, LST, and emissivity are updated. Each iteration is required to return values that are physically possible and the process is stopped when no further progress is made.

A literature search for an optimization tool that maintains feasibility and allows for nonlinear constraints led to a class of algorithms known as nonlinear programming (NLP). In particular, the generalized reduced gradients (GRG) method is appropriate for the optimization of atmospheric parameters. GRG is comparable to the Simplex method of linear

programming if the problem and constraints are linear, and similar to a gradient search for an unconstrained problem. The GRG method is useful for the surface parameter retrieval problem because it can handle nonlinear functions, allows boundary values to be defined for the parameter values, and is widely available. One version of the algorithm (Lasdon et al., 1978), has been implemented as the Constrained_minimum function in IDL 6.1 (Research Systems, 2005).

Generalized reduced gradients

The generalized reduced gradients algorithm is an iterative direct search method that solves for the optimal solution of a given model or problem while satisfying any given constraint equations. Each iteration in the GRG search reduces the value of the objective function. One advantage of the GRG algorithm for nonlinear problems is that the variables are continuously adjusted during the search to satisfy the constraints. This ensures that the final point is feasible, even if the algorithm stops before reaching the optimal solution (Luenberger, 1973).

The GRG algorithm was developed by Abadie and Carpentier at Electricite de France in 1969 as an extension to Wolfe's reduced gradient method (Abadie and Carpentier, 1969). The GRG algorithm generalizes the reduced gradient method to allow for a nonlinear objective function and nonlinear constraints. Nonlinear programming algorithms, including GRG, have been used for optimization of nonlinear networks, such as electric power flow, as well as for economic planning (Lasdon and D.Waren, 1980).

The basic idea of GRG is that the problem is linearized about an initial feasible point in a reduced space using the first-order terms of a Taylor series expansion. The problem variables are partitioned into basic variables and not-basic variables, with the number of basic variables equal to the number of constraints. The constraint equations are then

Table 3.4: A basic GRG algorithm

1.	Initialization: define optimization parameters, start from a feasible solution
2.	Compute the Jacobian of the constraints
3.	Partition the variables into basic and not-basic variables
4.	Compute the reduced gradient
5.	Stop if the current point is optimal
6.	Use the reduced gradient to find a search direction
7.	Perform a linesearch to find a new solution and restore feasibility
8.	Update the solution with the result of the linesearch Go to step 2

solved for the basic variables in terms of the not-basic variables. This reduces the model problem to an optimization problem of the not-basic variables. The objective function is now a function of the not-basic variables only. The search direction for the solution is derived from the reduced gradient. A line search is performed along the constraint surface by changing the not-basic variables in the negative direction of the reduced gradient and then adjusting the basic variables to maintain feasibility. GRG solves the original problem by generating a sequence of reduced problems. The main steps of the GRG algorithm are given in Table 3.4.

Step1 The GRG optimization is initialized by defining the optimization parameters. These parameters are the convergence tolerance (ϵ stop or `epstop`), the feasibility tolerance (`epfeas`), and the number of consecutive iterations (`nstop`). The default values for these parameters are provided in Table 3.5. When the optimality conditions are satisfied to within `epstop` in step 5 of the GRG algorithm, the current point is considered optimal and the algorithm is stopped. The algorithm is also stopped if the change in the objective function is stalled for over `nstop` iterations. The `epfeas` parameter is used in

Table 3.5: GRG Notation

Variable	Value or definition
m	number of constraints
n	number of variables
$n - m$	degrees of freedom of the system, also the reduced set of variables
X	n-dimensional vector of the variables
g	m-dimensional vector of the constraint functions
$g_{m+1}(X)$	objective function
x_b , y , s	basic variables, feasible, dependent , m unconstrained, implicitly determined by the independent variables, state or solution variables
x_{nb}, x , d	not-basic variables, independent, reduced set of $n - m$ decision variables, to be divided into x_n and x_s
x_n	nonbasic variables, the not-basic variables at one of their bounds
x_s	superbasic variables to be changed, not-basic variables between bounds, independent variables of the reduced problem
d_s	search direction for the superbasic variables
J	Jacobian matrix of the constraints
B , $\partial g / \partial y$	basis matrix from the columns of J, nonsingular $m \times m$
λ, π , p	Lagrange multipliers
$F(x)$	reduced objective function
$\nabla F, \partial f / \partial x_{nb}$	reduced gradients
`epstop`, ϵ	stopping or convergence tolerance (default $= 10^{-4}$)
`nstop`	consecutive iteration counter (default $= 3$)
`epfeas`	feasibility tolerance (default $= 10^{-4}$)

step 7 of the GRG algorithm. During the feasibility restoration, the equality constraints may not always be satisfied exactly, and `epfeas` is used to define an acceptable tolerance. The notation used for the GRG algorithm by different authors in the literature is often incongruous. The GRG notation used here is summarized in Table 3.5, and closely follows that of (Lasdon et al., 1978) and (Papalambros and Wilde, 2000).

After defining the optimization parameters, the GRG algorithm starts with an initial solution vector, $\hat{X}$, that is feasible, and preferably close to the optimal point. If any constraints are not feasible, a phase I procedure is started and the objective function is replaced with the sum of the violated constraints. Otherwise the GRG algorithm enters a phase II procedure (optimization) with a feasible solution and continues. The phase I procedure attempts to find a feasible point by solving an auxiliary piecewise linear programming problem (Windward Technologies and Optimal Methods, 1997). The value of the objective function after a phase I procedure is usually larger (worse) than the initial starting point, but it will be a feasible point. The details of a phase I procedure will not be presented. The general optimization problem is stated as:

$$\text{minimize} \quad g_{m+1}(X), \tag{3.3a}$$

$$\text{subject to} \quad 0 \leq g_i(X) \leq \mathsf{ub}(n+i), \qquad i = 1, 2, \ldots, m, \tag{3.3b}$$

$$\mathsf{lb}(i) \leq X_i \leq \mathsf{ub}(i), \qquad i = 1, 2, \ldots, n. \tag{3.3c}$$

The n-dimensional vector X represents the n variables that are being optimized, and the g_i functions are assumed differentiable. There are m constraints and g_{m+1} is the objective function.

The problem needs to be restated because GRG only deals with equalities. The inequality constraints in equations 3.3b and 3.3c are converted to equality constraints by

adding m slack variables, one for each of the m constraints. The optimization problem with equality constraints is stated as:

$$\text{minimize} \quad g_{m+1}(X), \tag{3.4a}$$

$$\text{subject to} \quad g_i(X) - X_{n+i} = 0, \qquad\qquad i = 1, 2, \ldots, m, \tag{3.4b}$$

$$\mathsf{lb}(i) \le X_i \le \mathsf{ub}(i), \qquad\qquad i = 1, 2, \ldots, n + m, \tag{3.4c}$$

$$\mathsf{lb}(i) = \mathsf{ub}(i) = 0, \qquad\qquad i = 1, 2, \ldots, n, \tag{3.4d}$$

$$\mathsf{lb}(i) = 0, \qquad\qquad i = n + 1, n + 2, \ldots, n + m. \tag{3.4e}$$

The first n elements in X are the variables that are being optimized, and the variables $X_{n+1}, \ldots, X_{n+m}$ are the new slack variables for the constraints. The values of the slack variables are greater than or equal to zero.

Step2 The next step is to compute the Jacobian of the constraints, J. The Jacobian is a matrix of the partial derivatives of the constraints with respect to the variables, and it is defined as:

$$J \triangleq \begin{bmatrix} \partial g_1/\partial x_1, & \ldots, & \partial g_1/\partial x_n \\ \vdots & \ddots & \vdots \\ \partial g_m/\partial x_1, & \ldots, & \partial g_m/\partial x_n \end{bmatrix} = \frac{\partial g}{\partial x}. \tag{3.5}$$

An approximation to the Jacobian matrix can be obtained using finite differencing. The Jacobian matrix needs to be evaluated for the current solution at each iteration.

Step3 The original problem, equation 3.3, is simplified to a reduced problem about $\hat{X}$ by partitioning the variables. The solution $\hat{X}$ satisfies the constraints in equation 3.3. The columns of the Jacobian matrix are partitioned into basic and not-basic portions,

$$J = [B, N], \tag{3.6a}$$

$$\hat{X} = (x_b, x_{nb}), \tag{3.6b}$$

where B is a submatrix of size $m \times m$,

$$B = \left(\frac{\partial g}{\partial x_b} \right). \tag{3.7}$$

The variables are partitioned by selecting m basic variables so that the basis matrix B is nonsingular (invertible) at $\hat{X}$. The remaining $n - m$ variables are labeled not-basic.

There are many possible choices for the set of basic variables. The basic variables should not be close to their bounds in order to avoid an early termination of the linesearch in step 7 (Lasdon and Smith, 1992). The basis matrix is required to be nonsingular because its inverse is used to compute the reduced gradient in the next step, as well as to maintain feasibility in step 7. The basis matrix should also be well conditioned, meaning that a small change in the matrix produces a small change in the solution. This is important because the inverse of a well conditioned matrix does not amplify estimation error. This improves the accuracy in solution for the Lagrange multipliers in step 4 and in the Newton iteration of the linesearch in step 7 (Lasdon and Smith, 1992). The basis selection procedure is based on complete pivoting.

The GRG algorithm uses the binding constraints to solve for the basic variables in terms of the remaining variables. The binding constraint functions are written as

$$g_i(x_b, x_{nb}) = 0, \qquad i = 1, 2, \ldots, m. \tag{3.8}$$

A constraint g_i is binding (holds as an equality) if it is within a tolerance ϵ of its bounds,

$$|g_i - \mathrm{ub}(n+i)| < \epsilon \qquad \text{or} \qquad |g_i - \mathrm{lb}(n+i)| < \epsilon. \tag{3.9}$$

The constraint equations can be used to eliminate the basic variables by solving equation 3.8 in terms of x_{nb}. This reduces the objective function to a function of the not-basic variables only,

$$g_{m+1}\big(x_b(x_{nb}), x_{nb}\big) = F(x_{nb}) \equiv F(x), \tag{3.10}$$

and the original problem is now unconstrained:

$$
\begin{aligned}
&\text{minimize} && F(x), \\
&\text{subject to} && \mathrm{l} \leq x \leq \mathrm{u}.
\end{aligned}
\tag{3.11}
$$

Step4   The partial derivative of the reduced objective function with respect to x is called the reduced gradient, $\triangledown F$. The reduced gradient provides the direction to search for an improvement to the current solution in step 6 of the GRG algorithm. By definition, the reduced gradient values for basic variables are zero (Windward Technologies and Optimal Methods, 1997). The derivation of the reduced gradient starts by expanding equation 3.10 in a Taylor series about x and including only the first-order terms,

$$\frac{\partial F}{\partial x}\mathrm{d}x_{nb} = \frac{\partial g_{m+1}}{\partial x_b}\mathrm{d}x_b + \frac{\partial g_{m+1}}{\partial x_{nb}}\mathrm{d}x_{nb}. \tag{3.12}$$

Similarly, equation 3.8 is approximated by a first-order Taylor series expansion

$$\frac{\partial g}{\partial x_b}\mathrm{d}x_b + \frac{\partial g}{\partial x_{nb}}\mathrm{d}x_{nb} = 0, \tag{3.13}$$

and rewritten using equation 3.7 as,

$$B\mathrm{d}x_b + \frac{\partial g}{\partial x_{nb}}\mathrm{d}x_{nb} = 0. \tag{3.14}$$

Equation 3.14 is solved for $\mathrm{d}x_{nb}$,

$$\mathrm{d}x_b = -B^{-1}\frac{\partial g}{\partial x_{nb}}\mathrm{d}x_{nb}, \tag{3.15}$$

and substituted into equation 3.12,

$$\frac{\partial F}{\partial x}\mathrm{d}x_{nb} = -\frac{\partial g_{m+1}}{\partial x_b}B^{-1}\frac{\partial g}{\partial x_{nb}}\mathrm{d}x_{nb} + \frac{\partial g_{m+1}}{\partial x_{nb}}\mathrm{d}x_{nb}. \tag{3.16}$$

Finally, the expression for the reduced gradient $\triangledown F$ is obtained by eliminating $\mathrm{d}x_{nb}$ from equation 3.16,

$$\frac{\partial F}{\partial x} = \frac{\partial g_{m+1}}{\partial x_{nb}} - \frac{\partial g_{m+1}}{\partial x_b}B^{-1}\frac{\partial g}{\partial x_{nb}}. \tag{3.17}$$

The reduced gradient can also be expressed as

$$\frac{\partial F}{\partial x} = \frac{\partial g_{m+1}}{\partial x_{nb}} - \lambda\frac{\partial g}{\partial x_{nb}}, \tag{3.18}$$

where λ is the Lagrange multiplier,

$$\lambda = \frac{\partial g_{m+1}}{\partial x_b}B^{-1}. \tag{3.19}$$

Step5 The GRG algorithm performs two tests on the current $\hat{X}$ to determine if it is optimal. The first test evaluates the Karush-Kuhn-Tucker (KKT) optimality conditions. The second test checks the progress of the objective function and determines if it has stalled. If the KKT conditions are satisfied to within the `epstop` tolerance, or if the fractional

change in the objective function is less than `epstop` for `nstop` consecutive iterations, then the current $\hat{X}$ is considered optimal and the GRG algorithm stops. Otherwise, a search direction is generated and GRG starts a one dimensional search for a new solution.

The KKT criteria define the necessary optimality conditions. The KKT conditions apply to the general nonlinearly constrained problem,

$$\text{minimize} \quad f(x), \quad\quad\quad\quad\quad\quad\quad\quad\quad\quad (3.20a)$$

$$\text{subject to} \quad h(x) = 0 \quad\quad \text{(equality constraints)}, \quad\quad (3.20b)$$

$$g(x) \leq 0 \quad\quad \text{(inequality constraints)}. \quad\quad (3.20c)$$

The Lagrangian for the optimality condition at a solution point x is written as

$$\Lambda(x, \lambda, \mu) = f(x) + \sum_i \lambda_i h_i(x) + \sum_j \mu_j g_j(x), \quad\quad (3.21)$$

and the KKT first-order conditions are

$$\nabla\Lambda(x, \lambda, \mu) = \nabla f(x) + \sum_i \lambda_i \nabla h_i(x) + \sum_j \mu_j \nabla g_j(x) = 0, \quad\quad (3.22a)$$

$$\forall i, \mu_i \geq 0, \quad\quad\quad\quad\quad\quad\quad\quad\quad\quad (3.22b)$$

$$\sum_j \mu_j g_j(x) = 0. \quad\quad\quad\quad\quad\quad\quad\quad\quad\quad (3.22c)$$

The partial derivative with respect to x of the gradient of the Lagrangian, equation 3.22a, states that at the optimal solution point p, $-\nabla f(p)$ is entirely contained in the subspace spanned by the $\nabla g_i(p)$ normals and the $\nabla h_j(p)$ normals. The partial derivatives with respect to the multipliers λ and μ states that the constraints must be satisfied at the optimal point. For the inequality constraints, the gradient of the objective function, ∇f, must

point towards the feasible side of the inequality constraints. This condition is satisfied by restricting the sign of the multiplier μ to be positive in equation 3.22b. The complementary slackness condition, equation 3.22c, states that $\mu_j = 0$ for inactive constraints (when $g_j(x) < 0$).

Step6   The computation of a search direction, d_s, requires the selection of the variables to be adjusted, the superbasic variables, as well as the direction of change for the superbasic variables. The not-basic variables, x_{nb}, are divided into superbasic variables x_s and nonbasic variables x_n. The not-basic variables which are at one of their bounds are labeled nonbasic variables, and the not-basic variables that are between their bounds are labeled as superbasic variables.

The search direction is computed as

$$d_s = -\left(\frac{\partial F^2}{\partial x^2}\right)^{-1}\frac{\partial F}{\partial x} = -H^{-1}\nabla F. \tag{3.23}$$

In practice, the inverse Hessian matrix in equation 3.23 is approximated using a quasi-Newton method based on the Broyden-Fletcher-Goldfarb-Shanno update formula.

Step7   The final step in the GRG algorithm is the linesearch along d_s to minimize the reduced objective function. The problem is stated as

$$\min_{\alpha>0} \quad F(\hat{x} + \alpha d_s). \tag{3.24}$$

A list of positive values for α is chosen to bracket the local minimum of $F(\hat{x} + \alpha d_s)$ approximately. In order to evaluate the reduced objective function for each α, the basic

variables x_b need to be determined by solving the constraint equations

$$g_i(x_b, \hat{x} + \alpha d_s) = 0, \qquad i = 1, 2, \ldots, m. \qquad (3.25)$$

The system is solved using Newton's method using the inverse basis matrix B^{-1}. The return to the constraint surface may not be exact. Instead, the constraint equations are satisfied to within a feasibility tolerance, `epfeas`. If an estimated basic variable reaches a bound, then that variable becomes a nonbasic variable. A basis change occurs and a superbasic variable becomes basic.

The line search operates by doubling the initial step size until a local minimum of the reduced objective function is bracketed. Then the step size is reduced until an improved minimum is found (Lasdon et al., 1978). The new solution $\hat{X}$ is set to $\hat{x} + \alpha d_s$ and the GRG algorithm returns to step 2.

An illustration of GRG's linesearch and return to feasibility is shown in Figure 3.12. In this example, there are three variables and one constraint, so the value of n equals three and the value of m equals one. The variables are represented by the axes x_1, x_2, and x_3, and the constraint is represented by the surface $h = 0$. According to the partitioning rules in step 3, m of the variables are made basic (labeled s_1 in Figure 3.12 for state or solution variable) and $n - m$ of the variables are not-basic (labeled d_1 and d_2 for decision variables).

The linesearch adjusts the current solution x_k towards x'_{k+1} by moving along the tangent to the constraint surface at x_k. This is accomplished by adjusting the not-basic variable vector from d_k to d_k+1 in the d_1, d_2 plane and then adjusting the basic variable vector $\mathrm{d}x_b$ (labeled $\partial s'_{k+1}$ in Figure 3.12) according to equation 3.15. This is a return to feasibility to satisfy the equality constraint to within the `epfeas` tolerance. An additional move from the point x'_{k+1} to x_{k+1} on the constraint surface is needed for a nonlinear constraint.
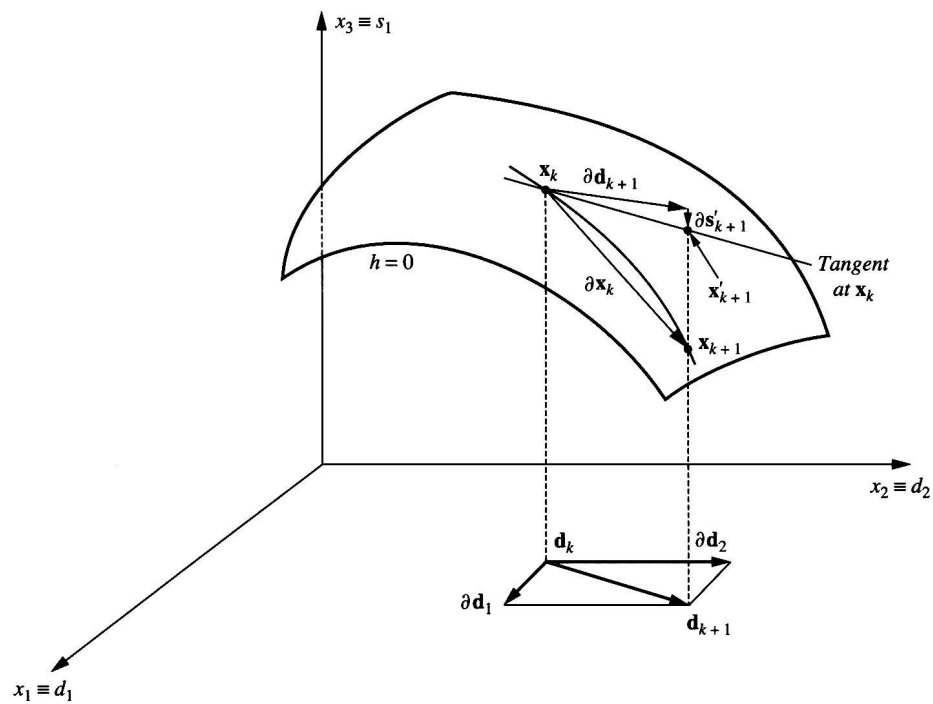
Figure 3.12: A GRG example for three variables (x_1, x_2, and x_3) and one nonlinear constraint, (surface $h = 0$) (Papalambros and Wilde, 2000).

Optimization approach

The GRG algorithm for the surface parameter retrieval problem was implemented using the IDL function Constrained_min (Research Systems, 2005). The variables to be adjusted are either the transmittance and upwelling radiance scaling factors in the initial GRG loop (used with equations 3.1 and 3.2a), or the estimated atmospheric transmittance and upwelling radiance for each band in the final GRG loop. The upper and lower bounds for the variables and the constraints are listed in Table 3.6. The determination of the values for the bounds is balanced by the need to return a physical solution while avoiding constraints that are too strict which results in an early termination of the GRG optimization. Bounds which are too loose can significantly increase the computation time. One way to avoid this is to update the bounds at the beginning of each iteration using the minimum and maximum values of the estimated variables and constraints, plus or minus a tolerance as listed in Table 3.6.

The objective function to be minimized is based on the spectral smoothness of each near-blackbody emissivity. The equation for the objective function is

$$F = \sum_{i=0}^{nBB-1} \left(\hat{\varepsilon}_{\lambda,i}\mid_{s.dev}\right)\left[\hat{\varepsilon}_{\lambda,i}\mid_{max} -\hat{\varepsilon}_{\lambda,i}\mid_{min}\right], \tag{3.26}$$

where $\hat{\varepsilon}_{\lambda,i}$ is the ith near-blackbody emissivity with λ bands. The values for $\hat{\varepsilon}_{\lambda,i}$ are computed by solving the radiative transfer equation for emissivity using equation 2.26. The objective function multiplies the difference between the largest and the smallest value of each $\hat{\varepsilon}_{\lambda,i}$ by its sample standard deviation over all spectral bands and sums the computed values over all near-blackbody pixels. The definition of spectral smoothness used in the objective function is different than the spectral smoothness defined in the ISSTES algorithm, equation 2.27. For the objective function, the ideal shape of each near-blackbody

Table 3.6: Parameters and boundary values for GRG optimization.

| Variable	Value or definition
$\hat{X}$	array of the variables to be optimized; the number of array elements is two for the first GRG loop using scaling factors $[\hat{X}_{ScaleTr}, \hat{X}_{ScaleLu}]$, or twice the number of sensor channels for the final GRG loop $[\hat{X}_{Tr}, \hat{X}_{Lu}]$
$\hat{X}_{ScaleTr}$	atmospheric transmittance scaling factor
	[the larger of $\left(\hat{\tau}(\lambda)\mid_{max} -0.1\right)$ and 0.5] $\leq \hat{X}_{ScaleTr} \leq$ [the smaller of $\left(\hat{\tau}(\lambda)\mid_{max} +0.005\right)$ and 0.9999]
$\hat{X}_{ScaleLu}$	upwelling radiance scaling factor
	$\text{abs}\left(\frac{\hat{L}_u(\lambda)\mid_{min}}{\hat{\tau}(\lambda)\mid_{max}}\right) \leq \hat{X}_{ScaleLu} \leq \text{abs}\left(\frac{\hat{L}_u(\lambda)\mid_{min}}{\hat{\tau}(\lambda)\mid_{max}}\right) + 1$
$\hat{X}_{Tr}$	atmospheric transmittance
	$0.01 \leq \hat{X}_{Tr} \leq$ [the smaller of $\left(\hat{\tau}(\lambda)\mid_{max} +0.005\right)$ and 0.9999]
$\hat{X}_{Lu}$	upwelling radiance ($\text{Wm}^{-2}\text{sr}^{-1}\mu\text{m}^{-1}$)
	[the larger of $\left(\hat{L}_u(\lambda)\mid_{min} -0.001\right)$ and 0.01] $\leq \hat{X}_{Lu} \leq 9.00$
$\hat{X}_{Ld}$	downwelling radiance regression coefficient (a_i term only in equation 2.34)
	$-0.1(\hat{X}_{Ld}) \leq \hat{X}_{Ld} \leq 0.05(\hat{X}_{Ld})$
Gbnd	Upper and lower bounds for the constraint functions
$\hat{g}_{Ld}$	downwelling radiance bounds
	$0.02 \leq \hat{g}_{Ld} \leq 10.00$ ($\text{Wm}^{-2}\text{sr}^{-1}\mu\text{m}^{-1}$)
$\hat{g}_{\varepsilon_{nBB}}$	bounds on the near-blackbody emissivities
	[the larger of $\left(\hat{\varepsilon}(\lambda)\mid_{min} -0.01\right)$ and 0.90] $\leq \hat{g}_{\varepsilon_{nBB}} \leq$ [the smaller of $\left(\varepsilon(\lambda)\mid_{max} +0.005\right)$ and 1]
F	objective function,
	based on the spectral smoothness of each estimated ε_{nBB} and summed over the working set of near-blackbody pixels
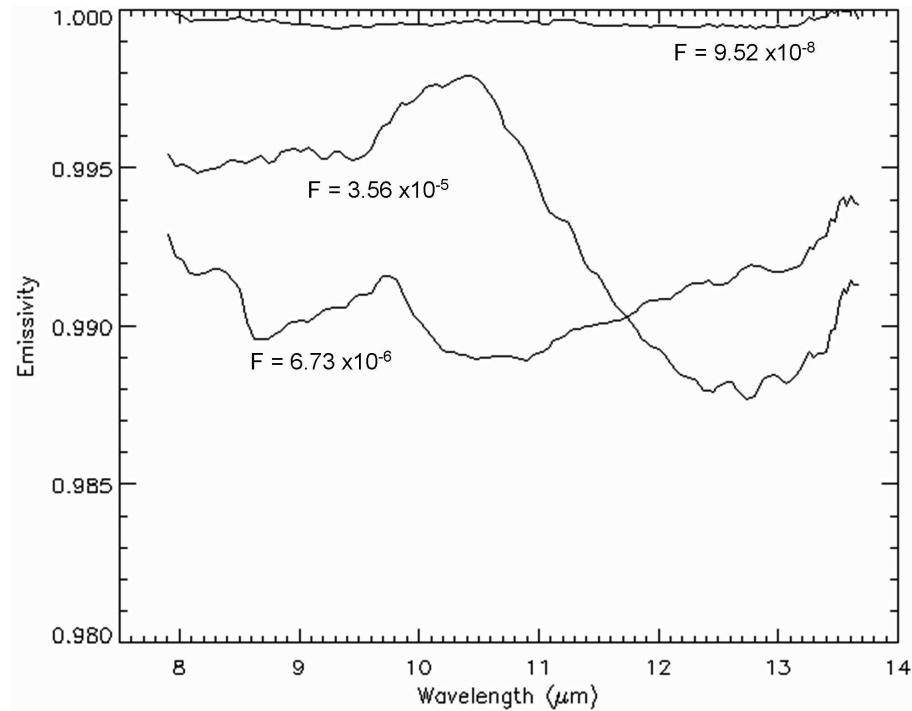
Figure 3.13: Objective function values for three sample emissivities.

emissivity is both spectrally smooth and flat. The objective function values for three sample emissivity spectra are shown in Figure 3.13. The emissivity spectra at the top has the smallest range of values and a relatively small standard deviation, so it has the lowest objective function value. In practice, the objective function values are summed over all the near-blackbody pixels according to equation 3.26.

The flowchart in Figure 3.14 shows the approach used to retrieve the surface parameters. The initial GRG loop adjusts the atmospheric parameter scaling factors. This step is designed to determine which of the five downwelling radiance LUTs to use (each LUT case is run sequentially) based on the maximum to minimum difference of the estimated emissivities as described in subsection 3.3.3. More importantly, adjusting the atmospheric
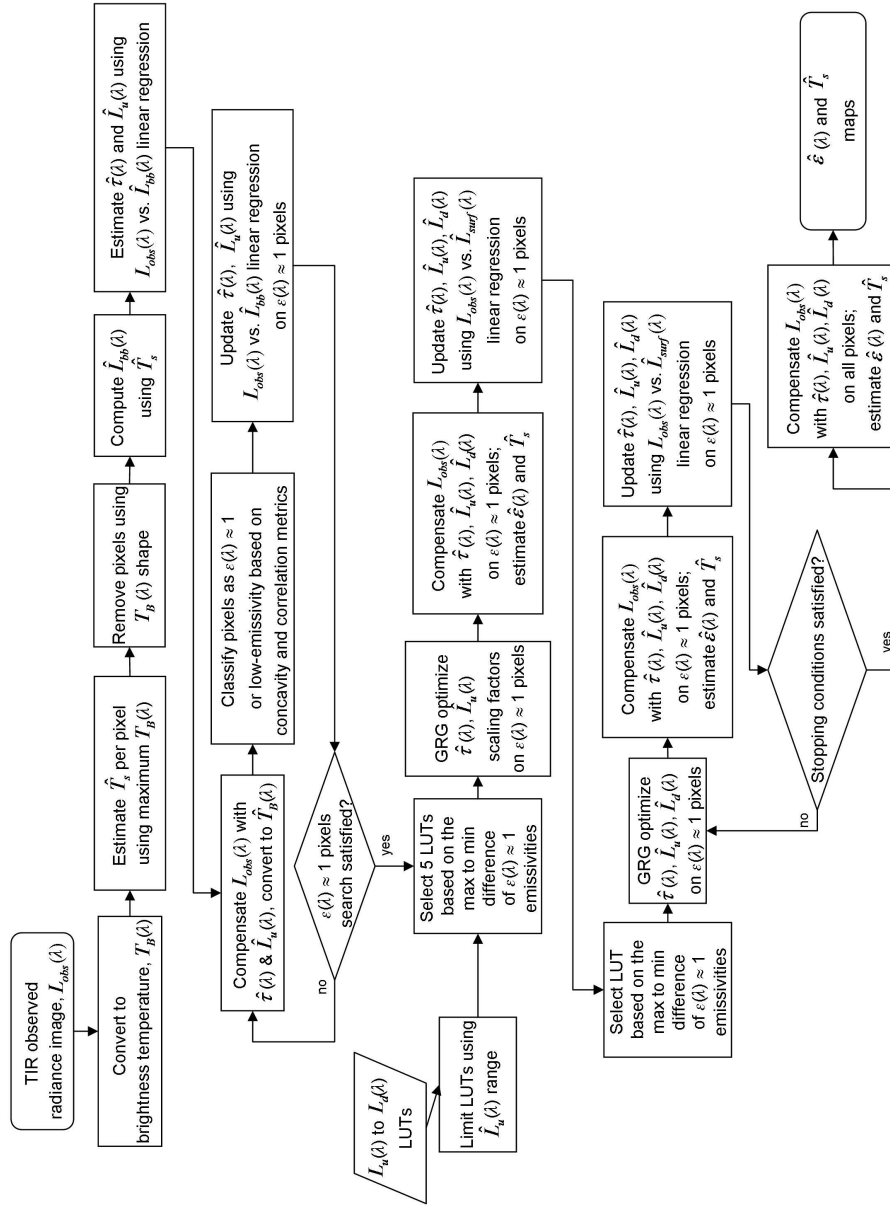
Figure 3.14: OLSTER flowchart.

parameters using scaling factors allows the final GRG loop to primarily optimize the spectral shape of the atmospheric parameters rather than both shape and absolute value. The initial GRG loop using scaling factors should provide the final GRG loop with a better starting point and allow it to converge faster. The steps in the initial and final GRG loops are listed in Tables 3.7 and 3.8, respectively.

Table 3.7: Steps in the initial GRG loop.

	For each of the five $\hat{L}_d(\lambda)$ LUTs on the working set of pixels,
1.	Adjust $[\hat{X}_{ScaleTr}, \hat{X}_{ScaleLu}]$ scaling factors using GRG
2.	Estimate $\hat{T}_s$ and $\hat{\varepsilon}(x, \lambda)$ using ISSTES
3.	Recompute the atmospheric compensation spectra using a L_{obs} vs. L_{surf} linear regression per spectral channel
4.	Go to step 1 and repeat for one more iteration if the objective function value has decreased

The optimization of the atmospheric transmittance and upwelling radiance in both initial and final GRG loops is performed on the near-blackbody set of pixels. In order to reduce the computational memory requirement for the final GRG loop (which has to optimize twice the number of sensor channel variables instead of two scaling factors), one hundred of the near-blackbody pixels with a spectrally-flat estimated emissivity ($[\hat{\varepsilon}(x, \lambda)\,|_{max} - \hat{\varepsilon}(x, \lambda)\,|_{min}] < 0.05$) are randomly selected as the working set of pixels.

The input for the GRG optimization includes the parameters shown in Table 3.6, the default values of `epstop` and `nstop` shown in Table 3.5, and a line search limit variable, `limser`, which terminates the GRG optimization after one thousand searches. The constraint equations estimate the downwelling radiance using the adjusted upwelling radiance and the downwelling LUT, and then determine the maximum and minimum emissivity values of the near-blackbody pixels. At the end of the GRG optimization, if the

Table 3.8: Steps in the final GRG loop (on the working set of pixels).

1.	Adjust $[\hat{X}_{Tr}, \hat{X}_{Lu}]$ using GRG
2.	Adjust $\hat{X}_{Ld}$ using GRG
3.	Adjust $[\hat{X}_{Tr}, \hat{X}_{Lu}]$ using GRG
4.	Estimate $\hat{T}_s$ and $\hat{\varepsilon}(x, \lambda)$ using ISSTES
5.	Recompute the atmospheric compensation spectra using a L_{obs} vs. L_{surf} linear regression per spectral channel
6.	Go to step 1 if the objective function value has decreased (limit of 4 iterations)

value of the objective function increases or if GRG fails to converge, the atmospheric parameters are reset to their values prior to the optimization. Otherwise, the result of the GRG optimization is a new estimate of the atmospheric parameters, as well as an initial estimate of the working set of near-blackbody emissivities. The remaining parameter in the radiative transfer equation that was not adjusted in the optimization is LST.

The LSTs and emissivities of the working set of near-blackbody pixels are simultaneously adjusted using the ISSTES algorithm. Equation 2.26 is solved for spectral emissivity for each pixel from the working set using an ensemble of temperature values about the current LST estimate and the GRG-adjusted atmospheric parameters. The temperature corresponding to the most spectrally-smooth emissivity becomes the new LST estimate for that pixel.

The next step is to refine the atmospheric parameters that were adjusted in the GRG optimization. This step is especially important in the final GRG loop since the $\hat{\tau}(\lambda)$, $\hat{L}_u(\lambda)$, and $\hat{L}_d(\lambda)$ parameters were allowed to vary independently from one band to another during the GRG optimization. The adjusted GRG atmospheric parameters may exhibit small spectral "spikes" that are the direct result of using an objective function that attempts to retrieve spectrally-flat and smooth near-blackbody emissivities. A linear

regression of the observed radiance versus the surface-leaving radiance for the working set of pixels is used to produce a refined estimate for each band of the atmospheric parameters. The surface-leaving radiance values are determined by equation 2.11 using the estimated emissivity and LST for the working set of pixels as well as $\hat{L}_d(\lambda)$. Refinement of the GRG atmospheric parameters in general will cause the estimated working set of near-blackbody emissivities to become unsmooth and even unphysical. This is actually a useful result because it provides new points for adjusting the working set of LSTs using the ISSTES algorithm. An iterative approach is used for both the initial and final GRG loops to adjust the current solution towards the optimal solution. The purpose of the first iteration is to nudge the atmospheric parameters away from a blackbody pixel assumption, while additional iterations are required to reach an optimal solution for the parameters.

The GRG algorithm can only locate the nearest local optimum solution from the starting point while satisfying the constraint equations. Finding the global optimum requires running the algorithm from multiple starting points and determining if the different starting points converge around the same feasible solution. While this does not guarantee a global optimum, it does provide more confidence for a global solution (Windward Technologies and Optimal Methods, 1997).

The optimization problem needs to be properly scaled by keeping the values of the constraint functions and variables within three orders of magnitude of each other. This is important because the GRG algorithm assumes that the objective function is equally sensitive to each variable or constraint (Singh and Sarkar, 1992). The GRG algorithm is also affected by scaling issues from the accumulation of roundoff error (Frontline Systems, 2000). The values of the constraint functions and variables should be large enough so that the computational errors on the order of the value of `epstop` are not significant (Windward Technologies and Optimal Methods, 1997). The range of variables in the surface

parameter retrieval optimization problem are given in Table 3.6.

For both the initial and final GRG loops, the stopping condition is when no further progress is made in reducing the GRG objective function. If a new iteration results in an objective function that is larger than the one from the previous iteration, the optimized variables from the new iteration are discarded and the saved variables from the previous iteration are returned. A limit is also placed on the number of allowed iterations to prevent a runaway process. Two iterations are allowed for the initial GRG loop to adjust scaling factors, and the final GRG loop is limited to four iterations.

The final step is to run the ISSTES algorithm on all the pixels from the image to estimate LSTs and emissivities. The LST and LSE results are the final products of the OLSTER algorithm. The LST and LSE results are saved to disk, along with the estimated atmospheric parameters, the index or locations of the near-blackbody pixels, the filenames that were opened by OLSTER, and the GRG log files.

3.4   Summary of the approach

A summary of the approach is given in Table 3.9. The OLSTER algorithm performs atmospheric compensation and surface temperature and emissivity retrieval on hyperspectral TIR imagery. An iterative approach is used to update initial parameter estimates based on the classification of near-blackbody pixels. A model-based $L_u(\lambda)$ to $L_d(\lambda)$ LUT and GRG optimization are used to gradually remove the blackbody assumption. Physical values for the estimated parameters are maintained by rescaling the atmospheric compensation spectra if necessary and by the boundary values on the GRG constraint functions.

The OLSTER algorithm is based on the ISAC, $L_u(\lambda)$ to $L_d(\lambda)$ LUT, and ISSTES algorithms. The new components introduced in OLSTER include a search for near-blackbody

Table 3.9: Summary of OLSTER

Key features:	• Iterative approach to atmospheric compensation
	• GRG optimization used to account for $L_d(\lambda)$ and gradually
	   remove the blackbody assumption
	• Direct use of radiative transfer model results as
	   compensation spectra is avoided
	• Implemented in IDL
	• Automated

Based on:	• ISAC algorithm for the initial estimation of $\tau(\lambda)$, $L_u(\lambda)$, and LST • GP algorithm's $L_u(\lambda)$ to $L_d(\lambda)$ LUT • ISSTES algorithm for temperature/emissivity separation
Novel approach:	• Search for near-blackbody pixels based on compensated brightness temperature • GRG optimization of the atmospheric compensation spectra

pixels, and GRG optimization of the atmospheric compensation spectra. OLSTER is coded in IDL and does not require a user to stop the iterations. The next chapter describes the experiments used to test (as well as to debug) the OLSTER IDL program on both simulated data and real image data.

Chapter 4

Experiment

The OLSTER algorithm as described in the previous chapter has been implemented in IDL. Currently, the IDL program consists of nine procedures and functions that are compiled and run from the command line using a batch file. The required inputs for running the program include the at-sensor hyperspectral radiance image, the sensor's spectral response function, the sensor altitude, and the downwelling radiance LUT corresponding to the sensor altitude. The program provides a status update which includes the number of near-blackbody pixels, range of the estimated LSTs and emissivities, the selected $\hat{L}_d(\lambda)$ LUT, the value of the objective function and run time. In addition, a report file is generated at the end of each GRG optimization. The file records the values of important parameters such as the objective function, step size, number of infeasible constraints, and the norm of the reduced gradient for each iteration. The values of these parameters are useful for monitoring the progress of the optimization and to determine if the optimization was performed correctly or if the solution is degenerate.

4.1 Initial test scene

A hyperspectral radiance image was created to test and debug the IDL program. The test image does not contain any spatial features. Instead, the image is simply an array of surface parameters propagated through a uniform atmosphere. The surface emissivities used in the image include rocks, soils, water, vegetation, and man-made materials from the ASTER spectral library (ASTER, 1999). A total of 395 materials were selected from the spectral library. The values for the LSTs were generated by randomly assigning three different temperatures, from 260 K to 320 K, to each material. Then each of the temperatures were randomly varied by up to $\pm$ 0.5 K, creating ten temperature values. In all, there are thirty temperatures for each material, for a total of 11,850 pixels. The surface is assumed to be flat and opaque.

The values for the atmospheric parameters were generated using the MODerate spectral resolution atmospheric TRANsmittance algorithm version 4, MODTRAN4 (Berk et al., 1999). The radiosonde data used in the MODTRAN simulation is an atmospheric profile over Southern California, obtained from the NOAA Forecast Systems Laboratory (FSL) database (FSL, 2005). The sensor altitude in MODTRAN was set to 2 km, with a nadir viewing angle, and the results from the atmospheric band model radiation transport code were resampled to 128 SEBASS sensor bands.

The values for the surface parameters and the resampled atmospheric parameters were substituted into the radiative transfer equation to generate the at-sensor radiance for 11,850 pixels. The image has no added noise or sensor artifacts for this initial test, and each pixel is spectrally pure. The atmosphere is assumed to be spatially uniform and cloud-free over the image.

The upwelling radiance to downwelling radiance LUT in the OLSTER algorithm is based on MODTRAN runs for a sensor altitude of 2 km. There are eleven variations

of the scaling factors of the vertical water vapor column and of the vertical ozone column for each of the six standard reference atmospheric profiles available in MODTRAN, giving a total of 726 MODTRAN runs. The scaling factors vary from 0.5 to 1.5 in increments of 0.1, and multiply the default values of water vapor column and ozone column in MODTRAN. In order to avoid values of relative humidity above 100%, MODTRAN redistributes the water number density at each profile altitude to other levels as necessary (Berk et al., 1999). The upwelling and downwelling radiance MODTRAN results were resampled to the SEBASS sensor bands. The LUT consists of regression coefficients for each standard reference atmosphere in MODTRAN as described in section 2.2.6.

The search for near-blackbody pixels selects 380 pixels from this image, and at the end of the optimization loop, the number increases to about 1500 pixels with a minimum emissivity of 0.97 or more. At the start of the optimization loop, the atmospheric parameters $\hat{\tau}(\lambda)$ and $\hat{L}_u(\lambda)$ are near their upper and lower bounds, respectively. After each iteration of the optimization loop, the values of at least one of the $\hat{\tau}(\lambda)$ and $\hat{L}_u(\lambda)$ parameters move further away from those bounds. The value of the objective function usually decreases after each iteration. On very few occasions, the value increases or GRG fails to find a feasible solution. In general, after OLSTER resets the atmospheric parameters to the previous feasible values, the objective function continues to decrease in value.

The OLSTER algorithm selects a downwelling radiance LUT to use for each iteration of the optimization loop. The LUTs that were usually selected are the Mid-Latitude Summer (MLS, $45°$ North Latitude) and Sub-Arctic Summer (SAS, $60°$ North Latitude). While the LUT selection based on the MLS reference atmosphere in MODTRAN4 made sense given that the atmospheric profile for the test image was from the FSL database for Southern California, the selection of the SAS LUT was initially unexpected. In practice, the most appropriate downwelling radiance LUT may not be selected, especially for the

first few iterations of the optimization loop, in order to satisfy the constraints.

While multiple starting points for the GRG optimization have not yet been implemented in OLSTER, the selection of the working set of pixels from the near-blackbody set (section 3.3.4) generates slightly different starting points for each run of the retrieval algorithm. In general, running the entire algorithm numerous times with different pixels in the working set produced similar results for the retrieved parameters.

The processing time on the test image is about five hours on a Sun Blade 1000 running SunOS 5.9 with 1024 MB of memory. The preprocessing steps and the search for near-blackbody pixels are completed in less than 10 minutes, while the final GRG optimization loop accounts for the rest of the processing time. The processing time primarily depends on the number of variables to optimize, which affects the size of the Jacobian matrix that must be evaluated for the current solution at each iteration.

Initially, the termination status report from the GRG optimization did not return the ideal status that the KKT conditions are satisfied to within the `epstop` tolerance. Instead, the termination status reported was:

> Noisy and nonsmooth function values,
>
> possible singularity or error in the function evaluations.

A closer look at the GRG report file shows a steady decrease in the value of the objective function for about the first twenty five line searches. Then the optimization appears to be stalled with only fractional decreases in the value of the objective function for the next one hundred twenty five line searches. The step size taken was incrementally smaller for these line searches. The GRG termination status and the report file indicate that additional work is needed on the objective function and proper scaling of parameter values. The objective function, equation 3.26, balances the requirement that the near-blackbody emissivities need to be both spectrally smooth and flat. This nonlinearity in the objective

function may be the cause of the noisy and nonsmooth values after each adjustment of the GRG variables. Another possible cause of this termination status is improper scaling of the variables. While the variables are within three orders of magnitude, it is possible that the values are not large enough to avoid computational roundoff error on the order of the value of the `epstop` tolerance. The benefits of achieving the ideal termination status include increased confidence in the solution values and reduced processing time by avoiding stalled iterations with very small step sizes.

The current approach that is used in the final GRG optimization loop limits the number of line searches to avoid a stalled state. The limit is currently set to the number of spectral channels in the dataset. Each iteration of the optimization loop first adjusts the atmospheric transmittance and upwelling radiance values per spectral channel, then adjusts the regression coefficients per spectral channel to estimate the downwelling radiance, and finally readjusts the transmittance and upwelling radiance values. This optimization approach works well for the initial test scene, as well as the synthetic test scenes and real sensor data that are described in the next few sections.

4.2   Synthetic test data

A set of synthetic test data was created for the purpose of characterizing the sensitivity of the OLSTER, ARTEMISS, and ISSTES algorithms to sensor noise, altitude, and spectral miscalibration. Additional synthetic test data was created to test scene – specific conditions for the special cases of night temperatures as well as a desert environment.

The sensor observed radiance value per pixel for the synthetic test data set was computed using equation 2.12. A material was selected from the ASTER spectral emissivity library (ASTER, 1999) and assigned a surface temperature. The atmospheric transmit-

tance, upwelling radiance, and downwelling radiance were computed by MODTRAN (Berk et al., 1999) using an atmospheric radiosonde profile from the FSL database (FSL, 2005), and resampled to 128 SEBASS sensor bands.

The sensor altitude for each case was set to 2km, 6km, and 10km, except for the sensor spectral miscalibration study, which was performed for a sensor altitude of 2km. A total of 357 materials from the ASTER spectral library were included. Water and vegetation materials (except for dry grass) were excluded for the desert case, leaving 345 materials. Surface temperature values were 24.5 $^\circ$ C $\pm$ 20, and 20 C $^\circ$ $\pm$ 4 for water and vegetation pixels. Temperatures for the night case were from 9 to 14 $^\circ$ C. Each synthetic test image contains 19,200 pixels.

Analysis of the sensitivity of the algorithms to sensor noise was performed by adding spectrally correlated noise derived from SEBASS imagery to the synthetic test images. The procedure is outlined in Table 4.1. A comparison of the covariance matrices of the estimated and synthetic correlated noise is shown in Figure 4.1. Structured noise (vertical striping) is not modeled by this process (Peterson et al., 2004). Structured noise is band specific and spatially varying.

The sensor spectral miscalibration study was performed for a sensor altitude of 2km and sensor spectral response shifts of $\pm$ 25, 12.5, 6.25, and 3.125 nm (uniform shifts for all channels). This is equivalent to physical movement of the position of a dispersion grating in a sensor system during launch or maintenance.

The OLSTER run times for all the cases were approximately 5 to 6 hours on a Sun Blade 1000 running SunOS 5.9 with 1024 MB of memory. The ARTEMISS run times were about forty minutes on the same computer with a database of 7,975 MODTRAN atmospheric LUT entries.

Table 4.1: Process for adding spectrally correlated noise. Modified from (Peterson et al., 2004).

1.	Select a uniform region of interest (ROI) (center pond in Figure 4.3)
2.	Minimum noise fraction (MNF) forward transform the ROI
3.	Select and keep bands with eigenvalues greater than 2 (46 bands out of 128)
4.	Inverse MNF transform the selected bands
5.	Obtain the zero mean dark scan estimate (DSE) by subtracting the inverse MNF result from the image ROI
6.	Perform a principal components analysis (PCA) on the DSE to decorrelate, save PCA statistics
7.	Create a synthetic noise cube of the same image dimensions as the synthetic scene by using the standard deviation of each PC to generate synthetic Gaussian distributed noise
8.	Perform an inverse PCA on the synthetic noise cube using the saved statistics of forward PCA in order to correlate the noise spectrally
9.	Add noise directly to the synthetic image band by band
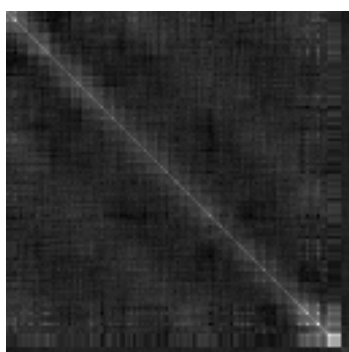
(a) Input covariance matrix of the estimated dark scan
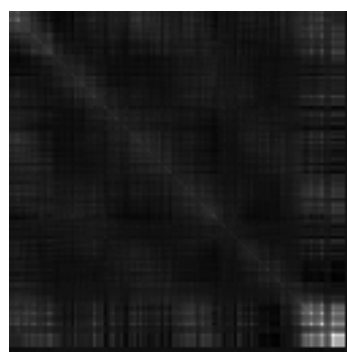
(b) Output synthetic covariance matrix

Figure 4.1: Covariance matrices of the estimated and synthetic correlated noise.

Figure 4.2: AHI data.

4.3 AHI data

The Airborne Hyperspectral Imager (AHI) sensor (Lucey et al., 1998) is a helicopter – borne LWIR hyperspectral imager from 7.5 to 11.5 μm in 256 spectral bands. The sensor was designed to detect buried landmines from the air.

AHI data taken over a chemical plant in Texas on April 19, 2004 was available for processing in OLSTER. The chemical plant is shown in Figure 4.2. There is no ground truth available for this data, but the sensor altitude was 1524 m. For this study, 200 bands were selected from the 256 bands, and were binned down to 50 bands to improve the signal to noise ratio. The 2 km sensor altitude downwelling radiance LUT was used for the OLSTER algorithm.

Figure 4.3: SEBASS image over an industrial area.

4.4 SEBASS data

Hyperspectral imagery from the Spatially Enhanced Broadband Array Spectrograph System (SEBASS) sensor (Kirkland et al., 2002) was available for two locations, an industrial scene, and the Megacollect scene near Rochester, NY. The SEBASS sensor is a line scanner that operates in the LWIR from 7.5 to 13.6 μm.

4.4.1 Industrial scene

The SEBASS image of an unidentified industrial area is shown in Figure 4.3. No ground truth information is available for this image. The sensor altitude is also unknown. The 6 km sensor altitude downwelling radiance LUT was used for the OLSTER algorithm.
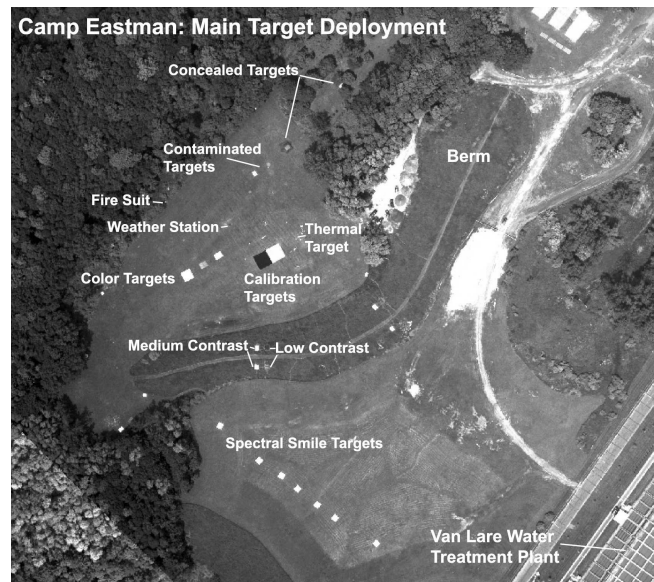
Figure 4.4: Targets for the Megacollect scene near Rochester, NY. Imaged using RIT's WASP sensor. (Raqueno et al., 2005)

4.4.2 Rochester scene

The other SEBASS image was taken on June 7, 2004, around 10:35 am local time at a sensor altitude of 1,043 m, as part of the RIT DIRS Megacollect (Raqueno et al., 2005). Two 25 ft x 25 ft canvas calibration tarps, one gray and one black, are included in the scene. A small heated thermal target, located just north of the large calibration tarps, consists of a heating coil element weaved back and forth across a styrofoam slab, and covered with black roofing material.

This data set also contains collected ground truth for the calibration tarps and the thermal target. The layout of the targets is shown in Figure 4.4. Temperature measurements are available from multiple contact thermocouples and a staring IR radiometer. Emissivity measurements were made with a D&P Instruments model 102F.

4.5   Experiment summary

An initial experiment designed to test and debug the OLSTER IDL program was created using a synthetic test image with no added noise or sensor artifacts. The test image contains a wide range of surface temperatures and emissivity spectra from the ASTER spectral library. A second set of synthetic test images was created to evaluate the sensitivity of the OLSTER, ARTEMISS, and ISSTES algorithms to sensor noise, spectral miscalibration, sensor altitude, night temperatures, and a desert environment.

LWIR data is available from two different hyperspectral sensors, AHI and SEBASS. The SEBASS Megacollect scene is accompanied by ground truth measurements of surface temperature and emissivity for three targets, and is important for the validation of the OLSTER algorithm. The results of the experiments are presented in the next chapter.

Chapter 5

Results

5.1 Initial test scene

The numerical simulation of the initial test scene using the OLSTER algorithm produced reasonable results for the atmospheric and surface parameters. Feasible values for the retrieved parameters were ensured in part by the GRG optimization constraints. There are no large discontinuities or spikes in the atmospheric parameters or the retrieved emissivities, and the overall spectral shapes of the atmospheric parameters are correctly estimated by the retrieved values.

The retrieved $\hat{\tau}(\lambda)$ is shown in Figure 5.1 along with the truth values. The values for the retrieved $\hat{\tau}(\lambda)$ are slightly higher over all the bands than the truth values, with an error of less than 0.003. The error plot for $\hat{\tau}(\lambda)$ is shown in Figure 5.2. The error is not uniform over all bands, with a spectral shape semi-correlated to the estimated transmittance itself. The percent error for the retrieved $\hat{\tau}(\lambda)$ is shown in Figure 5.3, with errors less than about 0.3 %.

The retrieved $\hat{L}_u(\lambda)$ values in Figure 5.4 are lower than the truth values. The absolute

value of the error is less than 0.04 $W/\text{m}^2/\text{sr}/\mu$m. The error in Figure 5.4 appears to be highly correlated to the estimated upwelling radiance itself. The normalized percent error (normalized by dividing $\hat{L}_u(\lambda)$ and $L_u(\lambda)$ by $L_u(\lambda)\mid_{max}$) is shown in Figure 5.3.

The spectral shape of both the transmittance and upwelling radiance retrieval error changes very little from the start of the optimization loop to the final iteration. The major difference between the iterations is the bias error. This is important because it shows that the GRG optimization could not completely eliminate the atmospheric compensation errors, and suggests that the downwelling radiance LUT was inappropriate or that the LST estimates were not accurate enough for the optimization, or both. The retrieval error is minimal at the edges of the LWIR window in Figures 5.2 and 5.4. However, in the context of the change in bias with each iteration, the transmittance and upwelling radiance error may be more correctly interpreted as having a positive bias of about 0.003 for the transmittance error, and a negative bias of about 0.035 $W/\text{m}^2/\text{sr}/\mu$m for the upwelling radiance, with the largest estimation error at the edges of the LWIR window for both estimation errors. A positive transmittance bias of 0.003 corresponds to a change in brightness temperature of approximately + 0.18 K, and a negative upwelling radiance bias of 0.035 $W/\text{m}^2/\text{sr}/\mu$m corresponds to a change in brightness temperature of approximately - 0.22 K. These equivalent errors in brightness temperature assume a surface temperature of about 300 K, an emissivity of one, wavelength at 10 μm, and a blackbody radiance of about 9.5 $W/\text{m}^2/\text{sr}/\mu$m.

The retrieved $\hat{L}_d(\lambda)$ is shown in Figure 5.7. In general, the spectral shape of the downwelling radiance in the image is very well approximated. Figure 5.8 shows almost no bias in the $\hat{L}_d(\lambda)$ error. However, there are large errors in the 9.5 – 10.3 μm region and at the edges of the LWIR window below 8.2 μm and above 13.0 μm. The errors are about an order of magnitude higher compared to the upwelling radiance retrieval error. The error
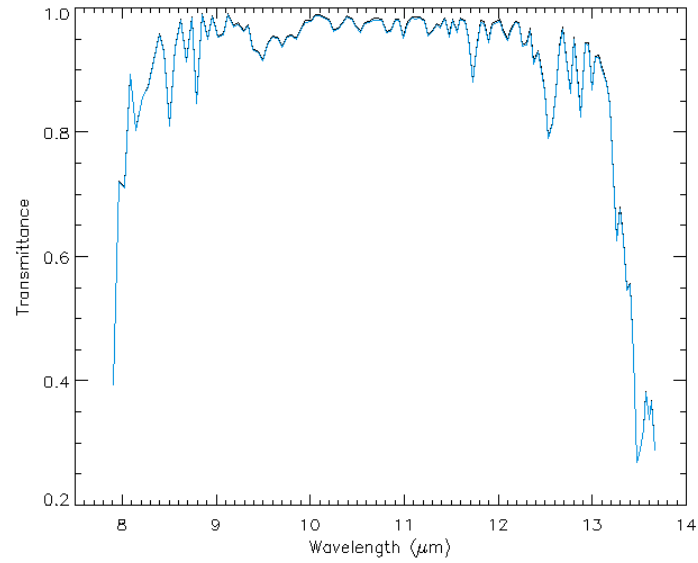
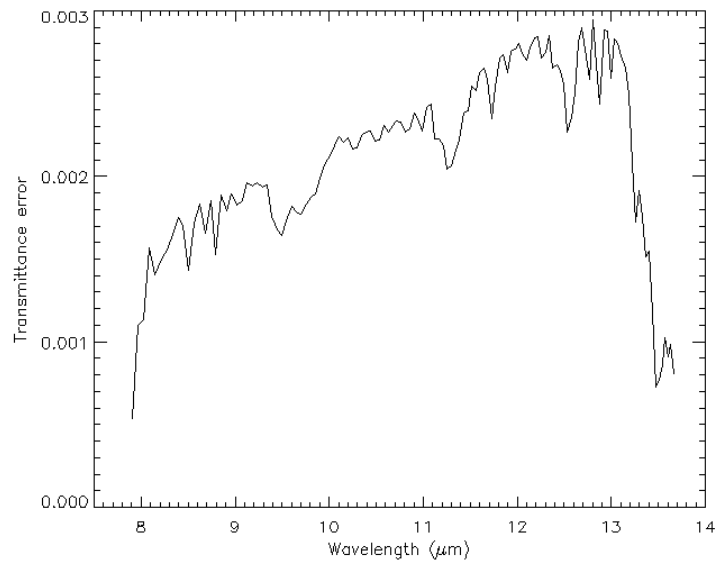Figure 5.1: Retrieved transmittance (black) and truth (blue) spectra.

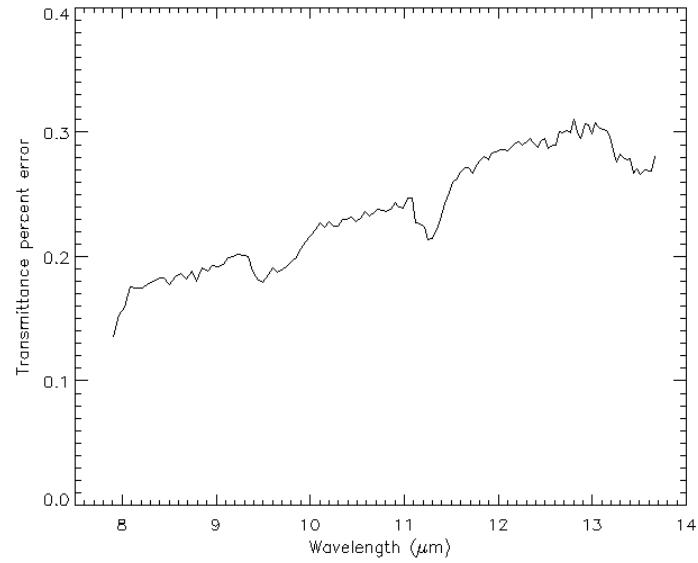Figure 5.2: Retrieved atmospheric transmittance error.

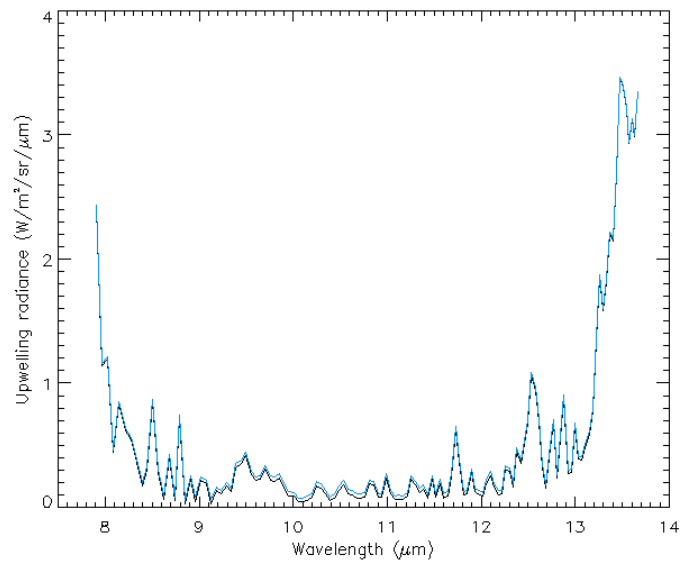Figure 5.3: Retrieved atmospheric transmittance percent error.

Figure 5.4: Retrieved upwelling radiance (black) and truth (blue) spectra.
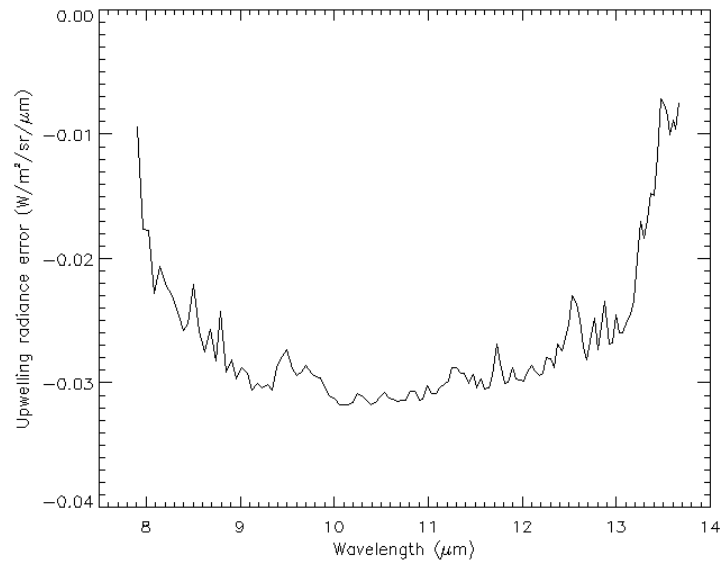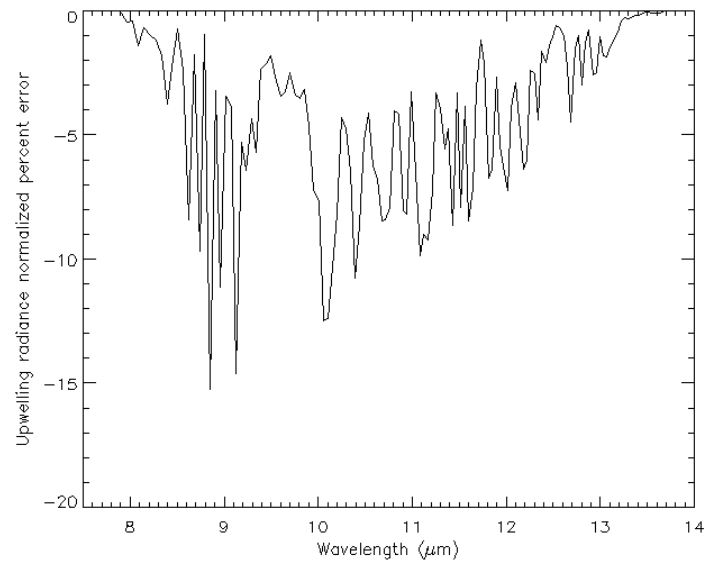
Figure 5.5: Retrieved upwelling radiance error.

Figure 5.6: Retrieved upwelling radiance normalized percent error.
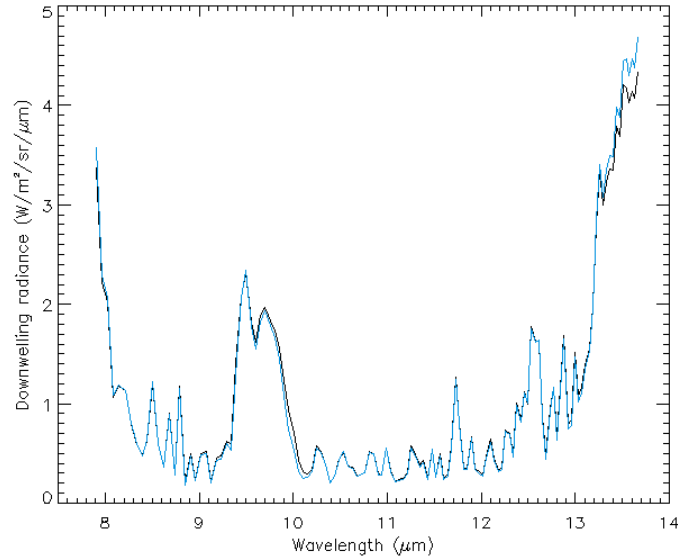
Figure 5.7: The retrieved downwelling radiance (black) and truth (blue) spectra.

in the 9.5 – 10.3 μm region is most likely related to ozone concentration, while the error at the edges of the LWIR window are related to water vapor concentration. The second-order polynomial coefficients used in the downwelling radiance LUT have difficulty encompassing the entire range of ozone and water vapor concentration variations, as shown in Figure 3.11 for their respective spectral regions. Variations of only the reference atmospheric profiles in MODTRAN4 may not be sufficient for creating a general downwelling radiance LUT. The $\hat{L}_d(\lambda)$ normalized percent error is shown in Figure 5.9, with errors generally less than about 2 % outside of the ozone region. The effect of the $\hat{L}_d(\lambda)$ error will depend on the surface emissivity. A downwelling radiance bias of $\pm\,0.1\ W/\mathrm{m}^2/\mathrm{sr}/\mu$m corresponds to a change in brightness temperature of approximately $\pm\,0.06$ K, assuming a surface temperature of about 300 K, an emissivity of 0.9, and wavelength at 10 μm.

The LST estimation error for the set of near-blackbody pixels is shown in Figure 5.10. The retrieved temperatures are higher than the truth values, with errors less than 0.25 K.
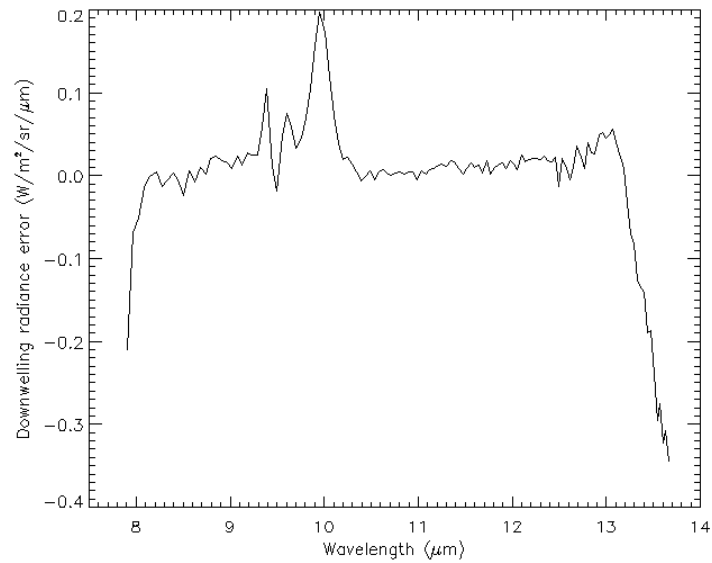
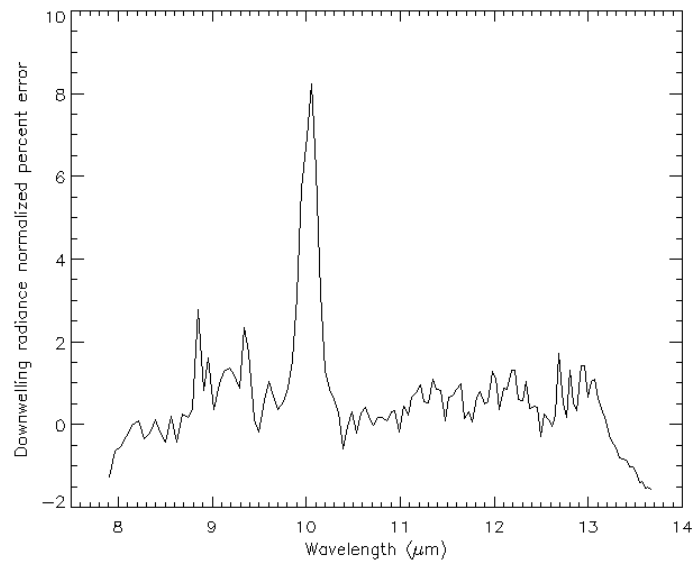Figure 5.8: Retrieved downwelling radiance error.

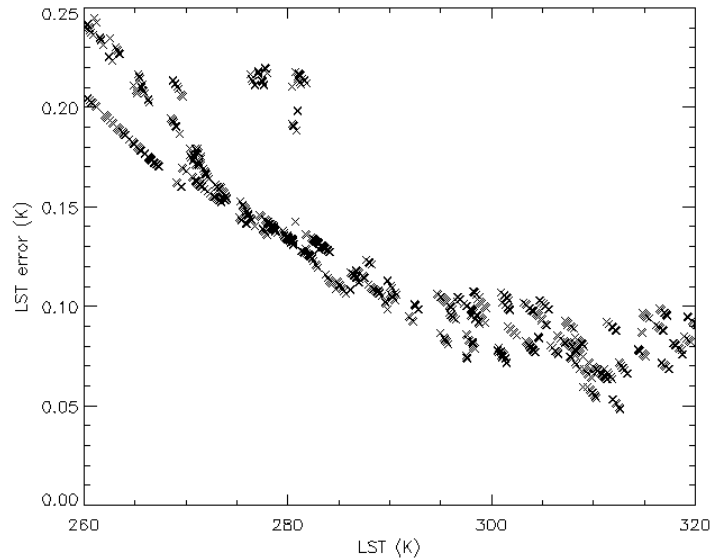Figure 5.9: Retrieved downwelling radiance normalized percent error.

Figure 5.10: LST error with respect to actual surface temperature for the near-blackbody pixels.

With the exception of a few localized clusters of LST estimation errors, the LST error is inversely proportional to the increase in the actual surface temperature. The likely explanation is that even for near-blackbody pixels, a higher surface temperature increases the surface emitted radiance contribution to the at-sensor radiance, resulting in an improved LST estimate. The clusters of LST estimation errors higher than the general trend are from the last addition to the near-blackbody pixels after the final iteration of the optimization loop. Simply restated, these pixels were not part of the GRG optimization, but rather low-emissivity pixels that were reclassified as near-blackbody at the end of the OLSTER algorithm because their minimum emissivity values are greater than 0.97.

The LST estimation error for the set of lower-emissivity pixels is shown in Figure 5.11. Most of the LST estimates for the low-emissivity pixels are too high. The scatter plot shows a noticeable increase in LST error as the minimum emissivity value
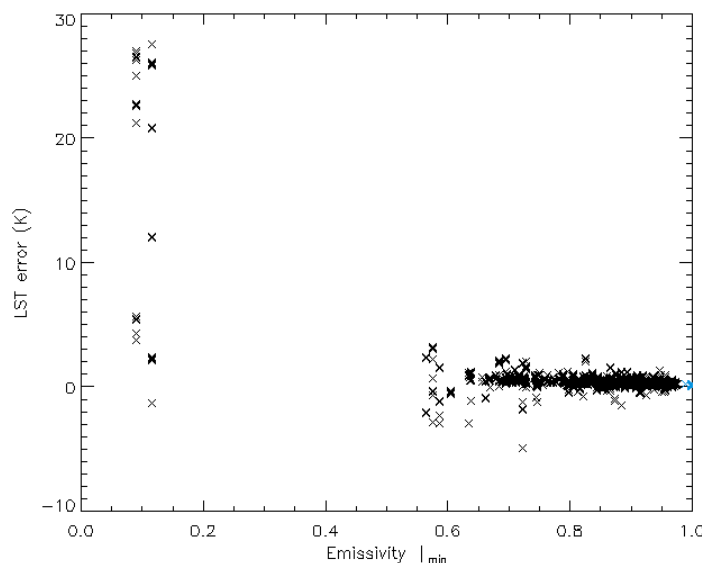
Figure 5.11: LST error with respect to the minimum library emissivity values for lower-emissivity pixels (black) and near-blackbody pixels (blue).

decreases. The various metal targets with a minimum emissivity less than 0.2 have a large range of LST error from about 2 to 28 K. The large range of LST error for the metal targets may be related to the downwelling radiance error, which has a large influence on very low emissivity pixels. The low emissivity pixels are also less sensitive to a change in the estimated LST compared to a pixel with a higher emissivity due to the reflected downwelling radiance term dominating the sensor reaching radiance. This makes the estimation of LST very difficult for the ISSTES algorithm on low emissivity pixels. The LST error is mostly within 2 K for targets with a minimum emissivity above 0.60, shown in Figure 5.12.

Figure 5.13 shows the mean and standard deviation errors for the estimated near-blackbody emissivities. The mean error is less than 0.001 over the LWIR window. The standard deviation at each band is about ± 0.001, with larger errors at the edges of the
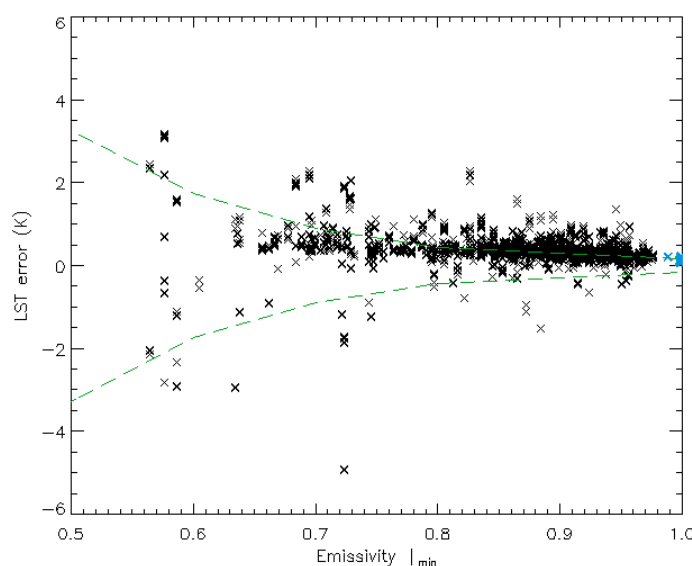
Figure 5.12: LST error for lower-emissivity pixels (black) and near-blackbody pixels (blue), excluding the metal surfaces. The standard deviation is indicated by the dashed lines.

LWIR window. A random sample of the estimated near-blackbody emissivities is shown in Figure 5.14. In general, the spectral shapes of the emissivities are correct, with some bias errors.

The retrieval error for the lower emissivity pixels in Figure 5.15 is much larger than for the near-blackbody pixels, with a mean bias of about -0.005 and a standard deviation of about $\pm$ 0.015 over most of the LWIR window. There are noticeable errors around the ozone absorption band and at the edges of the LWIR window that are associated with the downwelling radiance LUT. A few of the retrieved emissivities are shown in Figures 5.16 and 5.17. In general, the spectral shapes of the ASTER library emissivities are well approximated. However, in Figure 5.16 there are a few retrieved emissivities with errors where the atmospheric parameters were over-compensated and the LST overestimated.
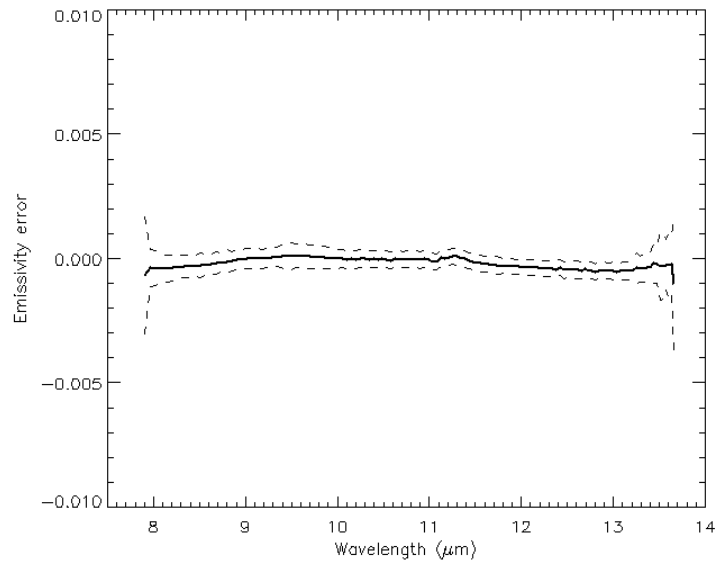
Figure 5.13: The mean (solid) and standard deviation (dashed) emissivity error for near-blackbody pixels.
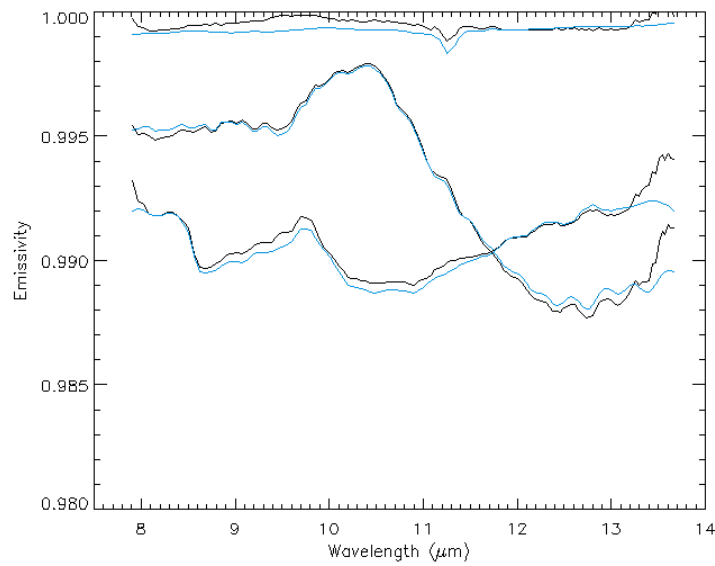

Figure 5.14: Retrieved emissivity (black) and truth (blue) for three random pixels from the near-blackbody set.
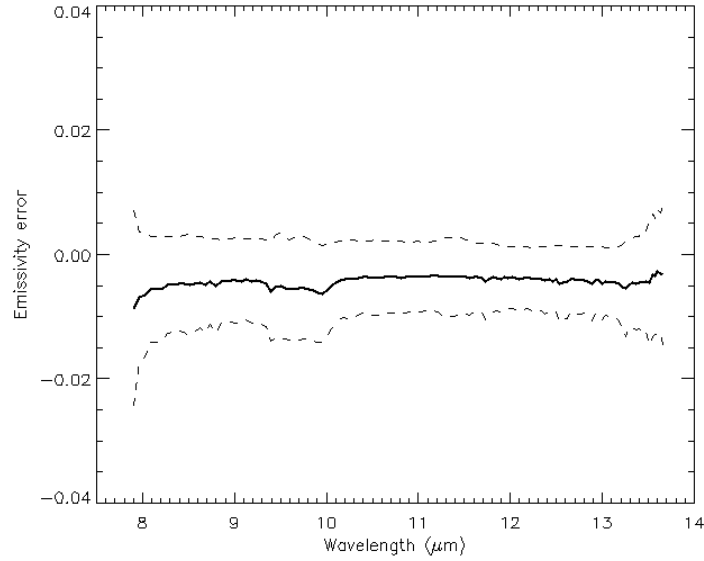
Figure 5.15: The mean (solid) and standard deviation (dashed) emissivity error for lower-emissivity pixels.

Again, these errors are more obvious at the edges of the LWIR window and around the ozone absorption band.

The results from a spectral angle mapper (SAM) classification on the retrieved emissivities are shown in Figure 5.18. The SAM classification measures the spectral angle in radians between each retrieved emissivity vector and a corresponding reference emissivity vector in the spectral library according to

$$\alpha = \cos^{-1}\left(\frac{t \cdot r}{\|t\| \cdot \|r\|}\right), \tag{5.1}$$

where t is the test spectrum and r is the reference spectrum. A small α value indicates high spectral similarity. The pattern of the classification error is similar to the LST error plots, with large errors for the low emissivity metals. Excluding the metals, the retrieved
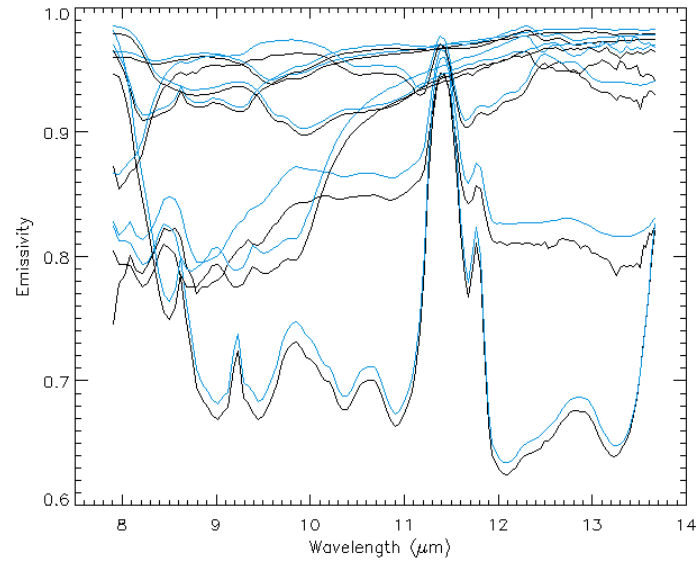
Figure 5.16: Retrieved emissivity (black) and truth (blue) for seven random pixels from the lower-emissivity set.
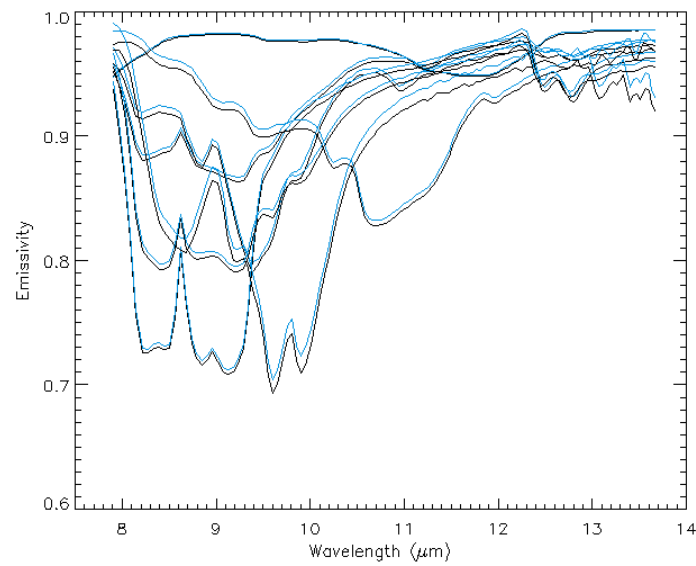

Figure 5.17: Retrieved emissivity (black) and truth (blue) for seven random pixels from the lower-emissivity set.

emissivities are spectrally similar to the reference emissivities in the ASTER library and are well within the ENVI default classification threshold of 0.10 radians. The classification threshold is noted here for the purpose of providing a reference only. In practice, the SAM classification threshold is user-adjusted.

The range of emissivity values for this initial test scene is in general more complex than what would be expected for an actual scene from an airborne sensor, where metal surfaces will have a higher emissivity due to weathering, surface roughness and contamination with natural materials (dust and dirt). Also, the range of simulated LSTs in this test scene is very broad and generally unrealistic (260 K to 320 K). A wide range of emissivity values and surface temperatures were selected for the initial test scene in order to determine potential limitations of the OLSTER algorithm. The results in the next section are from synthetic scenes with a smaller range of surface temperatures and have emissivity values higher than 0.6 to better represent actual scenes.

5.2   Synthetic test scene

The results for the synthetic test scenes are presented in this section in the form of LST, LSE, and SAM error plots. The mean error and standard deviation are shown for the no noise added, 3000:1 SNR, 1000:1 SNR, 500:1 SNR, 100:1 SNR, night temperatures (cold surface), and desert (no water or vegetation) cases. The errors at sensor altitudes of 2 km, 6 km, and 10 km are shown for each case.

5.2.1   OLSTER results

The OLSTER retrieved LST errors for the synthetic test scenes are shown in Figure 5.19. OLSTER LST errors are within about 1 K down to a SNR level of 500:1. Errors increase
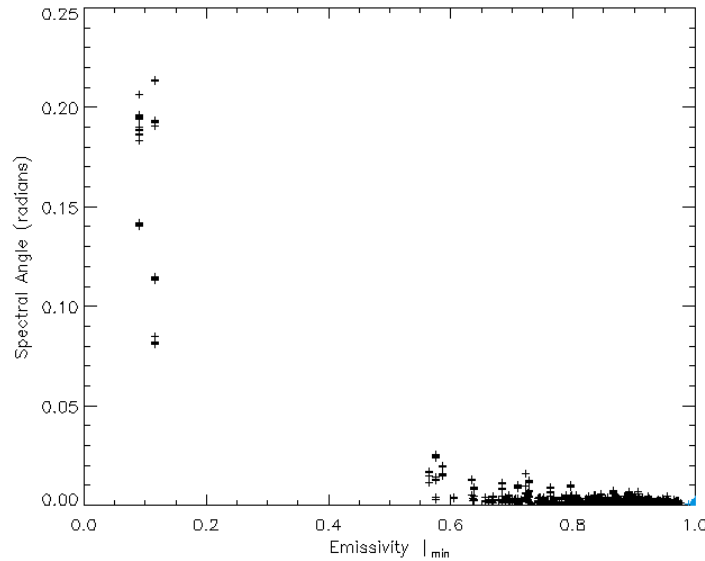
Figure 5.18: Spectral angle in radians between retrieved emissivities and library emissivities. The lower-emissivity pixels are in black, and the near-blackbody pixels are in blue.

for the desert case, night temperatures, and a SNR of 100:1. The desert case represents a violation of the OLSTER algorithm's assumption of some near – blackbody pixels in each scene. The poor starting point for the atmospheric parameters for the desert case is difficult to overcome using the GRG optimization.

The OLSTER retrieved LSE errors for the synthetic test scenes are shown in Figure 5.20. OLSTER LSE errors are within about 0.01 down to a SNR level of 1000:1. The SAM results, shown in Figure 5.21, represent the spectral angle between the retrieved LSE and the actual emissivity for the synthetic scenes. SAM values of less than 0.01 radians generally result in the correct material identification. This level is achieved for a SNR of at least 500:1.

Higher values for atmospheric transmittance at lower sensor altitudes provides a better
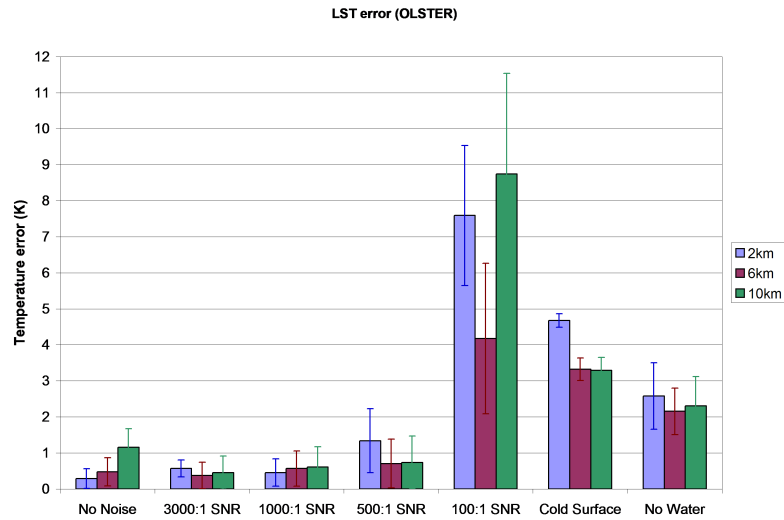
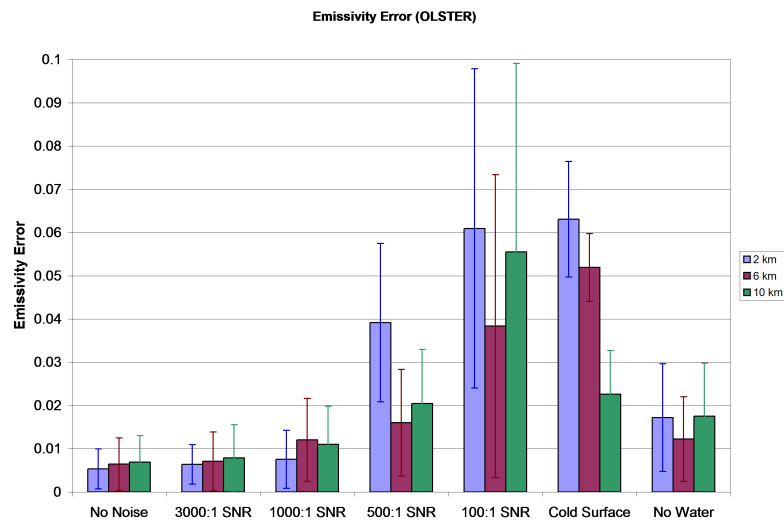Figure 5.19: OLSTER retrieved LST error.

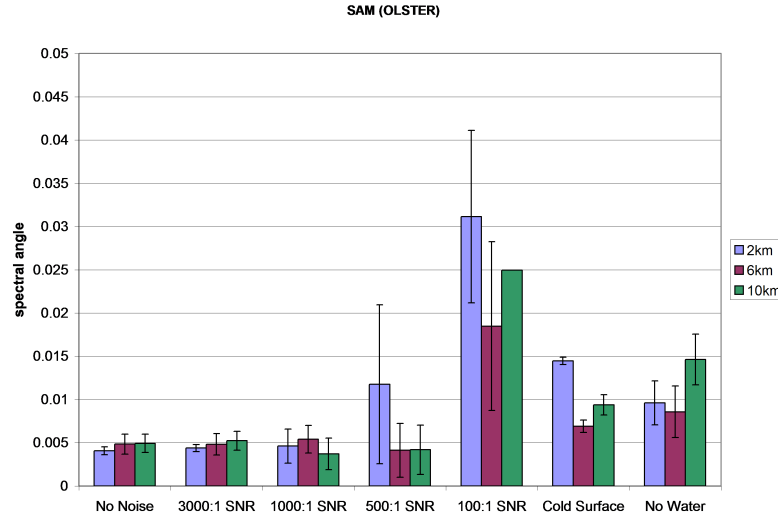Figure 5.20: OLSTER retrieved LSE error.

Figure 5.21: OLSTER retrieved SAM error.

SNR for the surface emitted radiance, which should result in smaller errors at lower sensor altitudes. This is not necessarily the case with the data – driven OLSTER algorithm, which selected different sets of near – blackbody pixels at each sensor altitude for the same test case. These different starting points lead to the varied results in the sensitivity to the sensor altitude. The 2 km sensor altitude, 500:1 SNR case in particular included a large number of low-emissivity pixels into the set of near – blackbody pixels. The data – driven approach also has difficulties with night temperatures, where the signal from the upwelling and reflected downwelling radiance from a potentially warmer atmosphere will dominate the signal from the surface emitted radiance. A night radiosonde profile was not available for the synthetic test scene. The bottom layer of the FSL radiosonde profile used for the test scene is about 10 K warmer than the simulated night LSTs.

5.2.2   ARTEMISS results

The atmospheric parameter database of MODTRAN results for the ARTEMISS algorithm used in this study contains 66 radiosonde profiles (MODTRAN provided, FSL, SSEC, and NAST-I databases) with 11 water vapor (WV) and 11 ozone scaling variations, for a total of 7,986 LUT entries. The entries with a WV scaling factor of 1 (no scaling) from the FSL radiosonde used to generate the synthetic scenes were removed from the LUT for the ARTEMISS test, leaving 7,975 LUT entries available for ARTEMISS.

The ISSTES results in the next subsection represent the best possible results for ARTEMISS, in which the actual MODTRAN atmosphere is selected for every run. In practice, the ARTEMISS results should lie somewhere between the results presented in this subsection and the ISSTES results, depending on the size and variability of the atmospheric parameter database of MODTRAN results and how well the actual atmosphere in a scene can be represented by a given database.

The ARTEMISS LST results, shown in Figure 5.22, exceed an error of 5 K for all cases. However, the LST error does not increase with higher levels of added noise, even down to 100:1 SNR. With the exception of the 100:1 SNR case at 2 km and for the night scene, the LST errors are generally smaller for a lower sensor altitude. The ARTEMISS LSE errors, shown in Figure 5.23, follows the same pattern with LSE error of 0.1 or higher for all cases.

The SAM values for the ARTEMISS results in Figure 5.24 show a large spectral angle of 0.02 radians or more for all cases, representing poor material identification results using a SAM classifier. The ARTEMISS results overall suggest the potential for small LST and LSE mean errors, regardless of the sensor SNR, if the atmospheric parameter database of MODTRAN results contains a very close match to the actual atmospheric parameters.

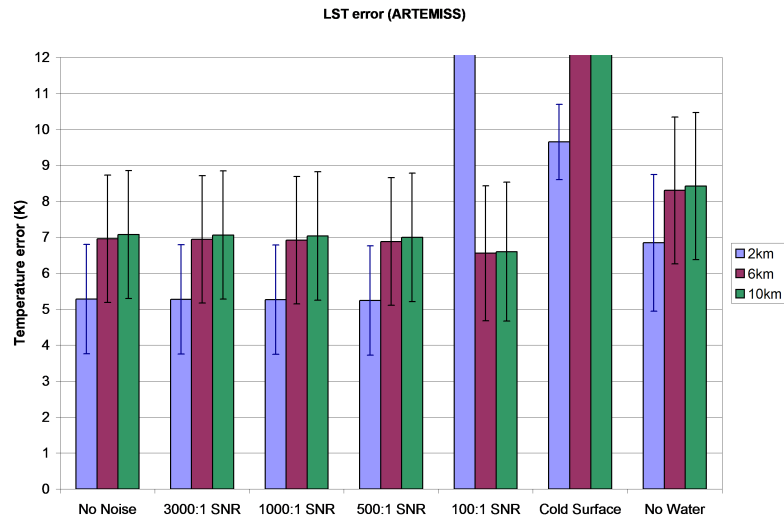A repeat of the ARTEMISS experiment was performed without excluding any entries

LST error (ARTEMISS)

Figure 5.22: ARTEMISS retrieved LST error.
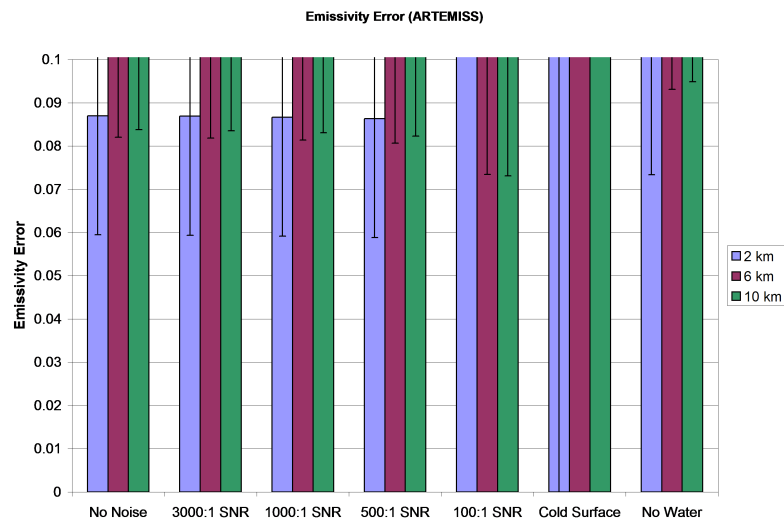
Emissivity Error (ARTEMISS)

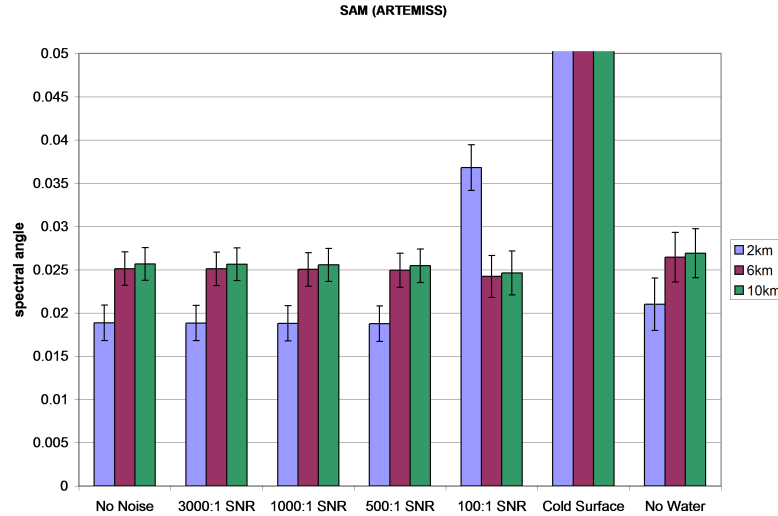Figure 5.23: ARTEMISS retrieved LSE error.

Figure 5.24: ARTEMISS retrieved SAM error.

from the TLD database. This experiment represents an ideal case for the ARTEMISS algorithm when the actual atmospheric properties for the scene are modeled and included in the TLD database. The results are shown in Figures 5.25, 5.26, and 5.27. The LST, LSE and SAM error results are much lower than for the excluded LUT case, with mean LST errors of about 1K, mean LSE errors of less than 0.02, and SAM values of less than 0.01 radians for all test cases except the simulated night (cold surface) case and the 1 km 100:1 SNR case. It should be noted that ARTEMISS did not select the exact atmospheric compensation spectra from the MODTRAN TLD database. In general, the correct radiosonde was selected, with an incorrect ozone scaling of 1.2 instead of 1.0 (no scaling). The large errors for the simulated night (cold surface) case and the 1 km 100:1 SNR case are caused by a poor ISAC estimate of the atmospheric transmittance in the selection of candidates from the TLD database.
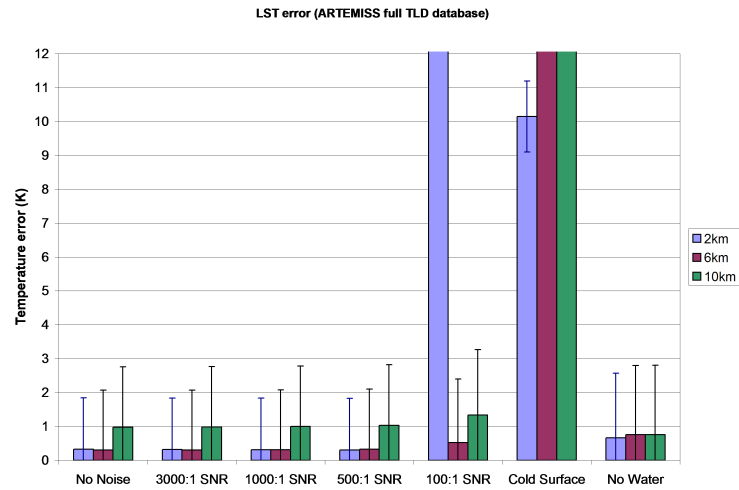
Figure 5.25: ARTEMISS retrieved LST error. The ARTEMISS TLD database includes the atmospheric spectra used to generate the synthetic scenes.
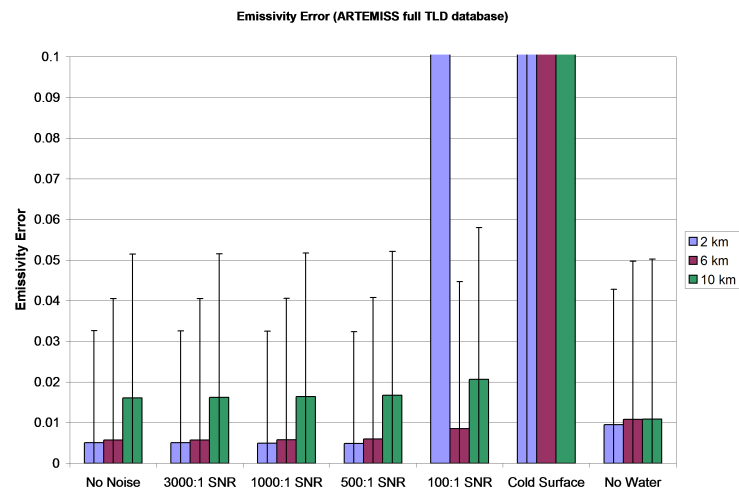

Figure 5.26: ARTEMISS retrieved LSE error. The ARTEMISS TLD database includes the atmospheric spectra used to generate the synthetic scenes.
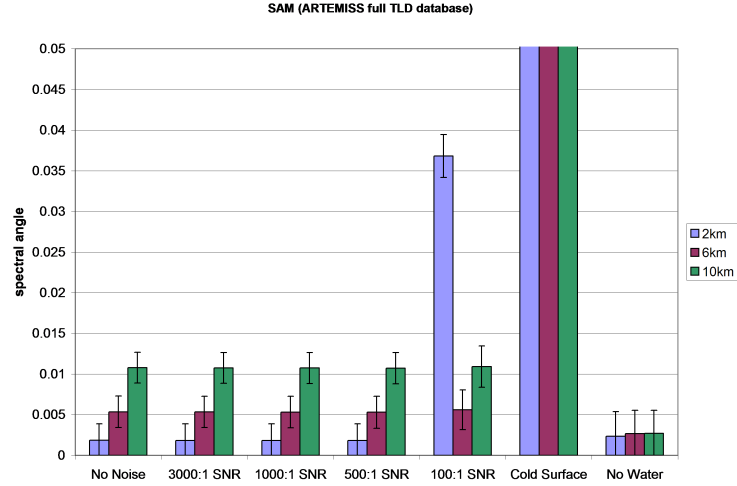
Figure 5.27: ARTEMISS retrieved SAM error. The ARTEMISS TLD database includes the atmospheric spectra used to generate the synthetic scenes.

5.2.3 ISSTES results

The ISSTES results represent the best case for the ARTEMISS and OLSTER algorithms of a perfect atmospheric compensation. A near perfect atmospheric compensation would require selecting an entry in the atmospheric parameter LUT that exactly matches the actual atmosphere for ARTEMISS, and an ideal starting point and optimization by OLSTER.

The ISSTES LST errors in Figure 5.28 are all well under 1 K. A comparison of the desert case (no water or vegetation) with the no noise case shows an increase in LST errors with lower emissivities in a scene. The ISSTES algorithm is relatively insensitive to sensor noise and night temperatures, and a general trend of smaller LST errors with a lower sensor altitude is observed. The ISSTES LSE errors in Figure 5.29 are about 0.01 or
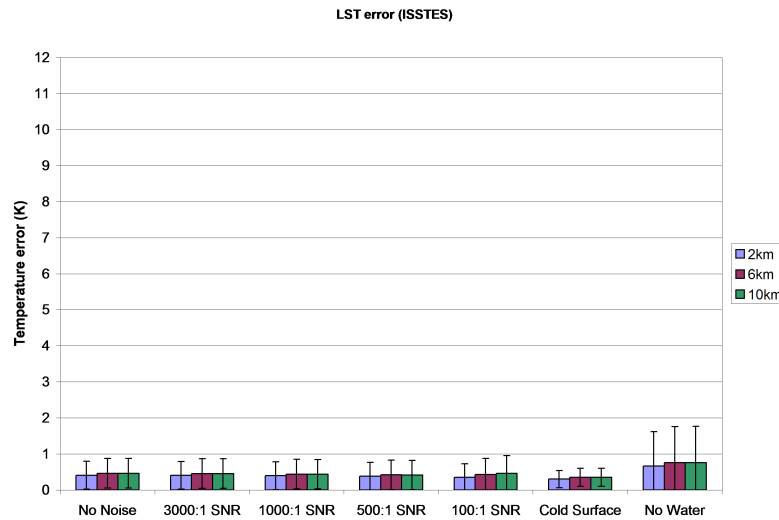
Figure 5.28: ISSTES retrieved LST error.

smaller for all cases. The SAM results in Figure 5.30 are all well under the ideal threshold of 0.01 radians.
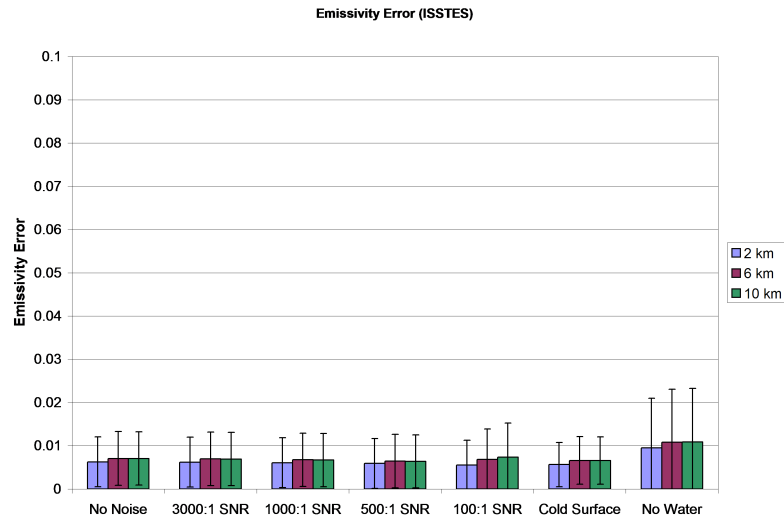
Figure 5.29: ISSTES retrieved LSE error.
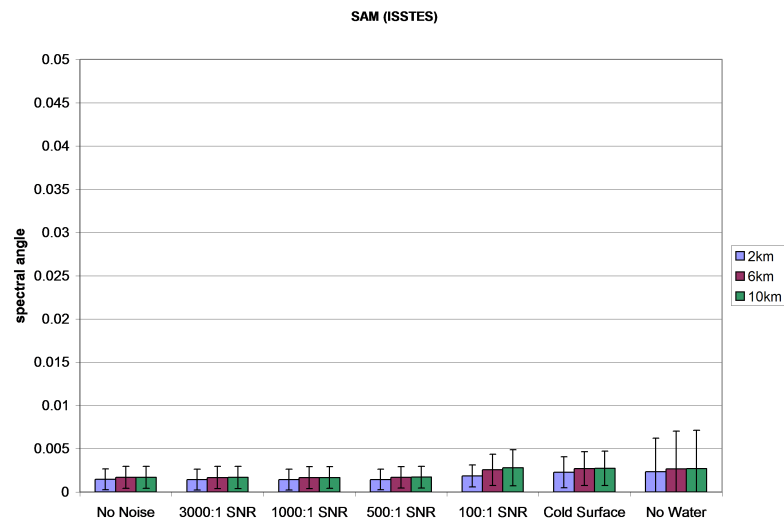
Figure 5.30: ISSTES retrieved SAM error.
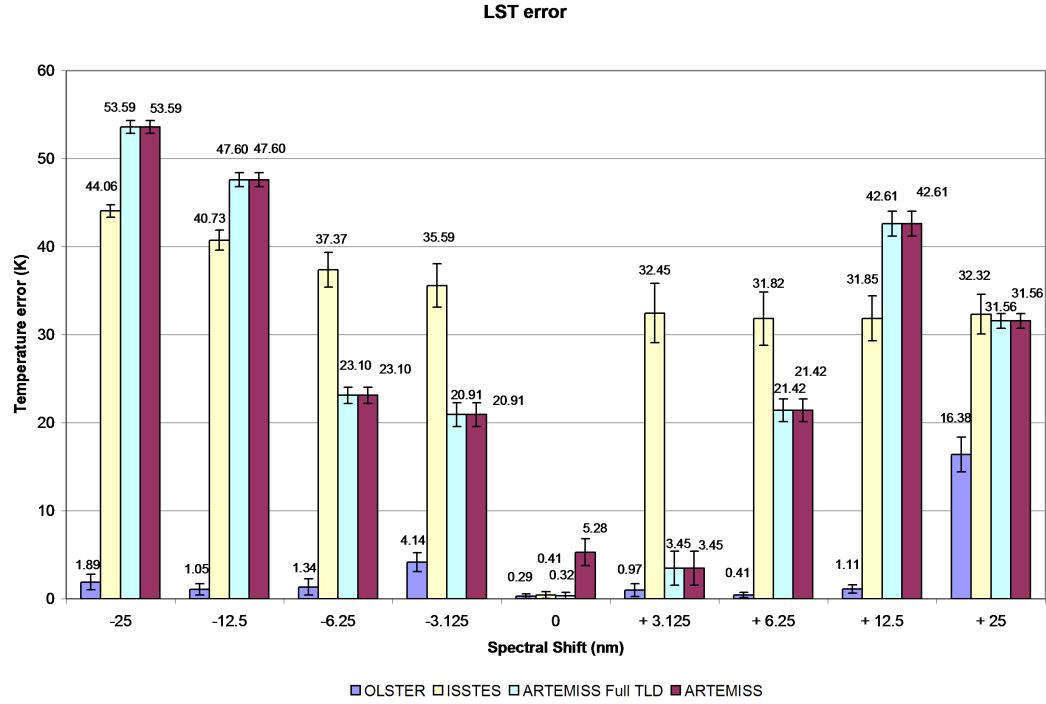
Figure 5.31: Spectral miscalibration LST error.

5.2.4 Spectral miscalibration results

The LST and LSE errors for the 2 km sensor spectral miscalibration study are shown in Figures 5.31 and 5.32, respectively. OLSTER errors are much lower than for the ARTE-MISS or ISSTES algorithms. OLSTER is capable of retrieving LSTs to within 1 K, with the exception of spectral shifts of + 3.125 nm and ± 25 nm. The smallest LST error using ARTEMISS is 3.45 K at a spectral shift of + 3.125 nm. The lowest LSE error using OLSTER is 0.01 at + 6.25 nm and +12.5 nm spectral shifts.

The SAM results, shown in Figure 5.33, are within about 0.01 radians for OLSTER

except for the + 25 nm spectral shift. The SAM classifier should be able to correctly identify materials given the small spectral angle between the OLSTER retrieved LSE and the spectral library.

Errors for all algorithms appear to be specific for a given spectral shift. A small shift does not always produce smaller errors than a larger shift. The algorithm results depend on whether a shift in the spectral response of the sensor occurs at a particular edge of an atmospheric spectral feature. The ARTEMISS results are the same for both the full TLD database and the partial TLD database, with the exception of the zero shift (no spectral miscalibration) case.

The OLSTER and ARTEMISS algorithms in general outperform the ISSTES algorithm for the sensor spectral miscalibration case. The primary goal of the OLSTER and ARTEMISS algorithms is to retrieve accurate land surface parameters, which requires an accurate compensation of the atmospheric parameters. However, for data with sensor spectral miscalibration issues, the optimal atmospheric compensation spectra to use may not match the physical atmospheric parameters that may be measured by a radiosonde profile over the scene. The OLSTER and ARTEMISS algorithms are effectively absorbing the spectral miscalibration errors in the atmospheric compensation spectra. The optimization of the atmospheric compensation spectra per spectral channel allows OLSTER to achieve better LST and LSE results than ARTEMISS.
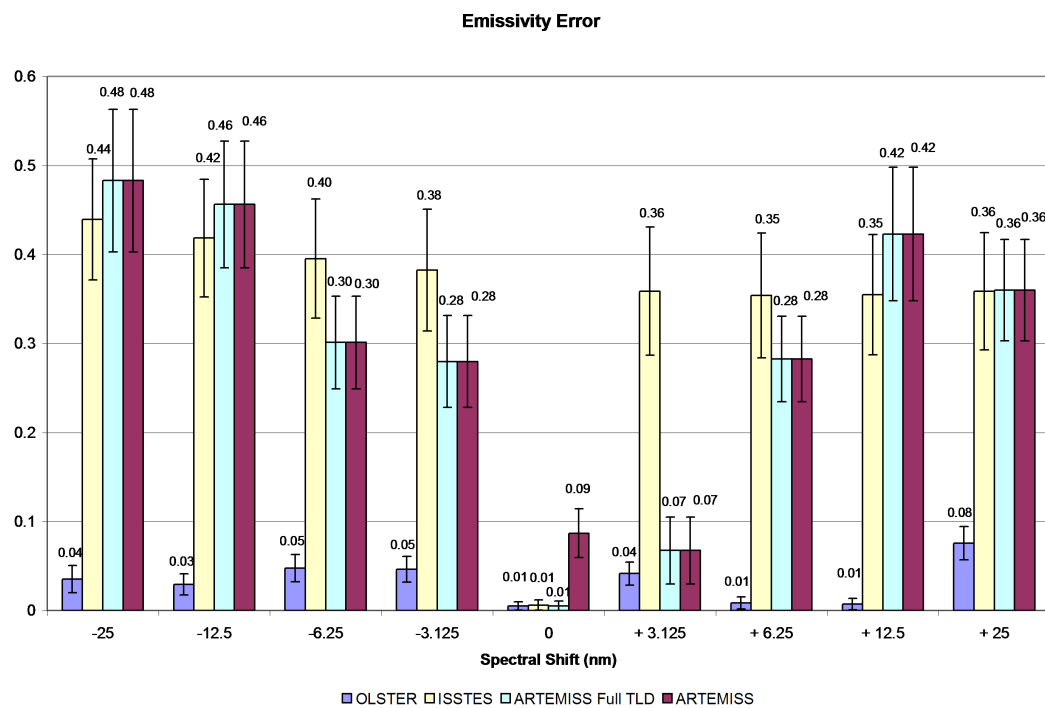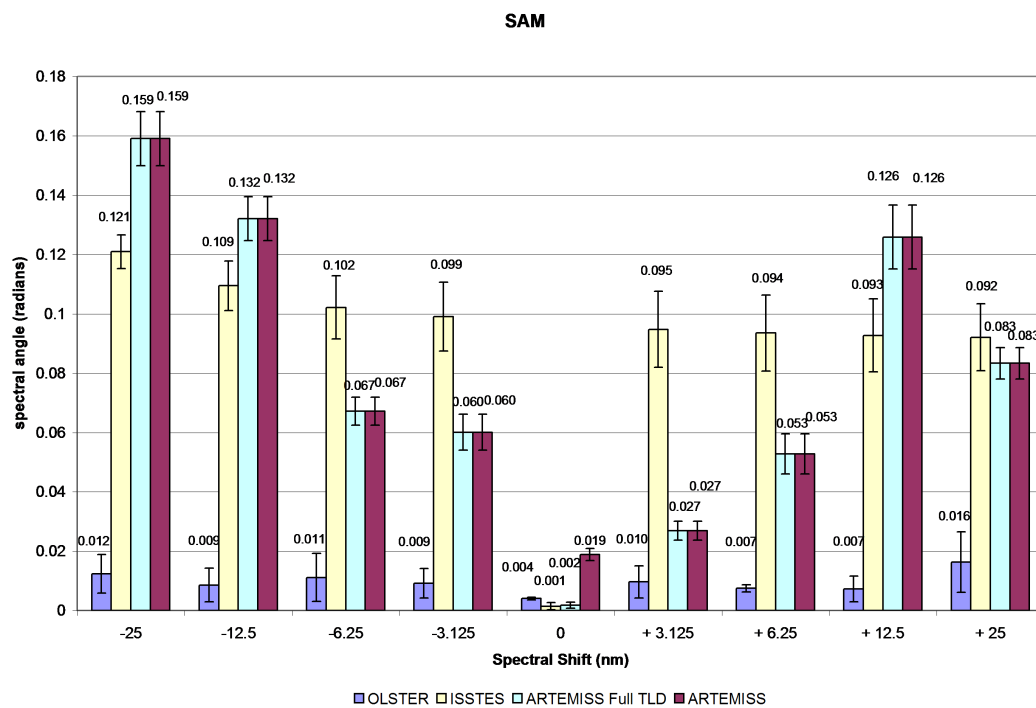
Figure 5.32: Spectral miscalibration LSE error.

Figure 5.33: Spectral miscalibration SAM error.

5.3   AHI data

The OLSTER results for the AHI data are shown in Figure 5.34. While no ground truth information is available for this image, the test on the AHI data demonstrates that the OLSTER algorithm can be applied to various sensor data.

The LST results in Figure 5.34(a) in general show relatively cooler surface temperatures for the canal and pipes, and hotter temperatures for the buildings and roofs. The minimum emissivity value of about 0.98 for the canal is appropriate. The sensor noise is apparent in the minimum emissivity results in Figure 5.34(b). The SAM results in Figure 5.34(c) are mostly within 0.01 radians.

A region with a minimum emissivity value of 0.65 and a SAM value of 0.02 radians is visible in Figures 5.34(b) and 5.34(c). The spatial shape of the region suggests that it could be a plume. The retrieved emissivity spectra (not shown) for the pixels in this region have a general shape of the estimated atmospheric transmittance for the entire scene with some additional spectral structure in the $9-10$ μm region. However, the binned spectral bands (from 256 bands to 50) can not resolve sharp spectral features to compare with known gases.

(a) LST map (b) Minimum emissivity per pixel (c) SAM map comparing the OLSTER results to the ASTER spectral library
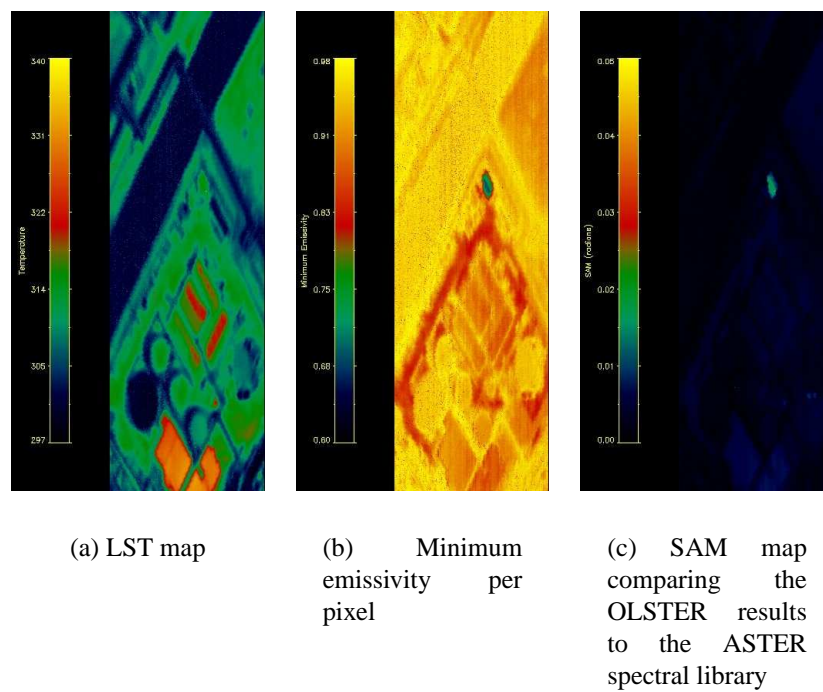
Figure 5.34: OLSTER results for the AHI data.

5.4 SEBASS data

5.4.1 Industrial scene

The sequence of images in Figure 5.35 shows the pixels classified as near – blackbody pixels at various steps in the OLSTER algorithm. The first step in Figure 5.35(a) shows the pixels that the modified ISAC algorithm selected based on the range of values over the LWIR window for each pixel. Pixels with a range less than the median for all image pixels are shown in red. This modification to the ISAC algorithm is required for this image since high emissivity pixels do not dominate this desert industrial scene. The first step correctly selected the pond pixels. It also incorrectly selected pixels in the industrial area in what appears to be shadow areas.

The second step in the selection of near – blackbody pixels uses both the correlation with $\hat{\tau}(\lambda)$ and the concavity metrics as described in subsection 3.3.2. This step correctly removed most of the low emissivity pixels in the industrial area, as well as some pixels in the center and right ponds, as shown in Figure 5.35(b). The pixels in the ponds that were removed may be affected by the sensor structured noise pattern along the scan track.

The final step eliminates low emissivity pixels from the set of near – blackbody pixels based on the initial LSE estimates. This step removed all of the low emissivity pixels in the industrial area, as shown in Figure 5.35(c). Additional pond pixels were also removed, which are also associated with the sensor structured noise pattern along the scan track.

The OLSTER retrieved atmospheric transmittance, upwelling radiance, and downwelling radiance spectra are shown in Figures 5.36, 5.37, and 5.38, respectively. The general shape and values of the atmospheric compensation spectra appear comparable to a MODTRAN run for a Mid-Latitude Summer profile. However, the spectra are not as smooth as expected, particularly around 8.8 μm and in the spectral regions from 12.2 –

(a) ISAC step

(b) Classified using both correlation and concavity metrics
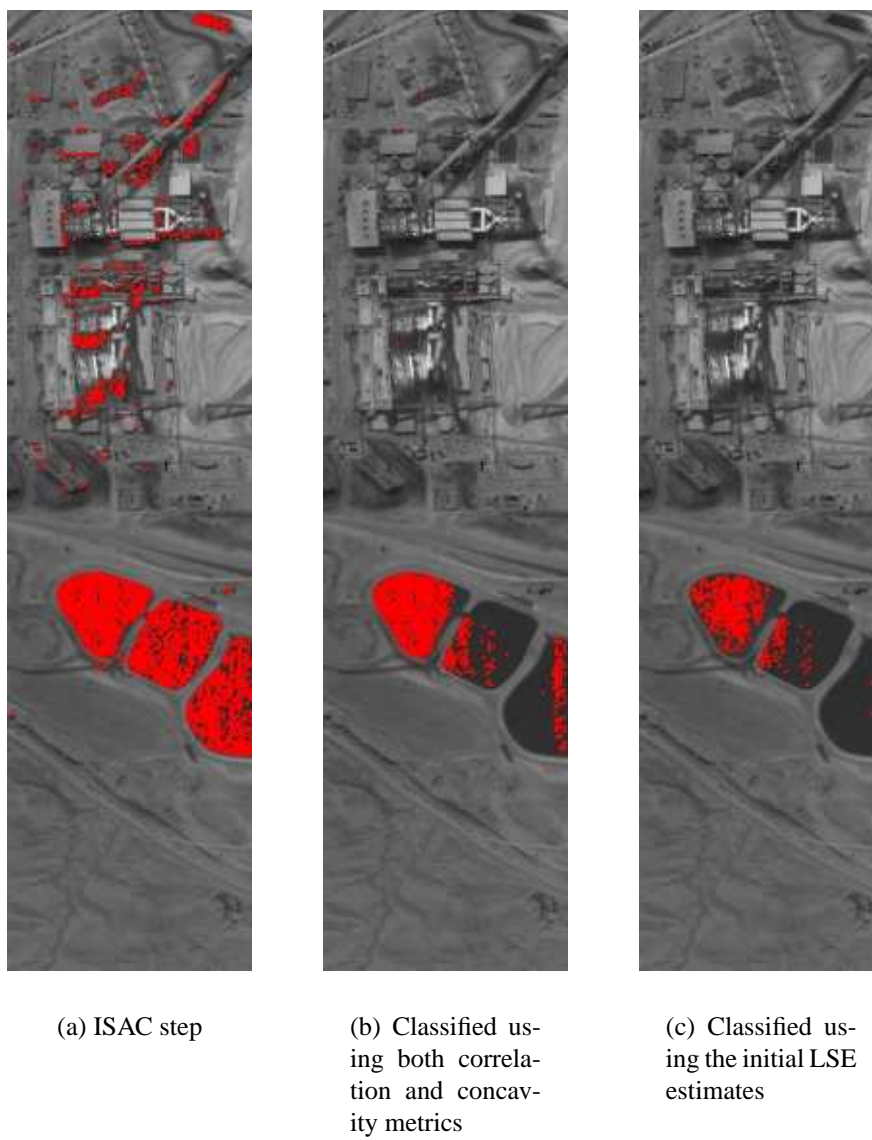
(c) Classified using the initial LSE estimates

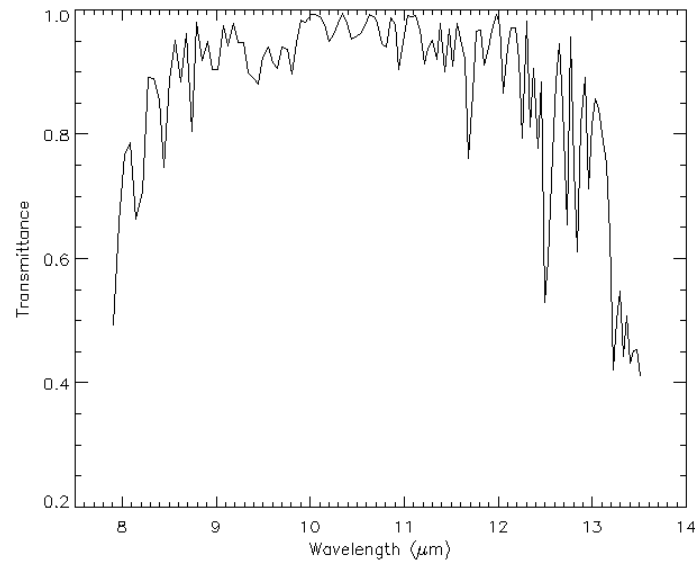Figure 5.35: OLSTER classification of near-blackbody pixels.

Figure 5.36: OLSTER retrieved transmittance for the industrial SEBASS scene.

12.8 μm and from 13.2 –13.6 μm.

The OLSTER retrieved LST maps are shown in Figure 5.39. Ground truth temper-atures are not available for this scene. The water ponds and shadow areas are relatively cooler than the rest of the scene, while some of the buildings and an area on the right side are the hottest. A vertical line can be seen on the left side of the LST map along the scan track, which is caused by structured sensor noise.

A segment of the LST map is shown in Figure 5.39(b). The displayed temperatures are thresholded at 300 K in order to view the thermal structure of the ponds. The left pond has LSTs that are warmer along the bottom edge. This warm pond appears to flow into the cooler center pond. The flow pattern can be seen as it enters the center pond.

The right pond contains a hot source at a point on the bottom left side of the pond. The warm water from the hot source does not appear to flow along the edge as it does in the left pond, but rather it diffuses over the entire pond. This suggests that the right pond
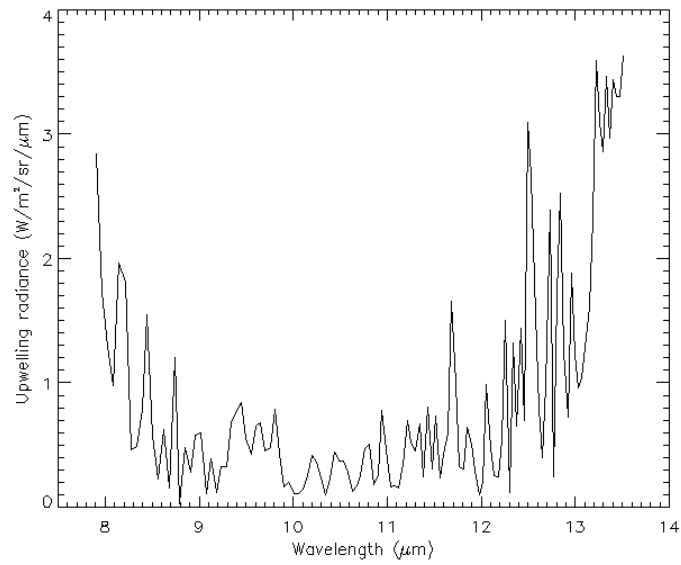
Figure 5.37: OLSTER retrieved upwelling radiance for the industrial SEBASS scene.
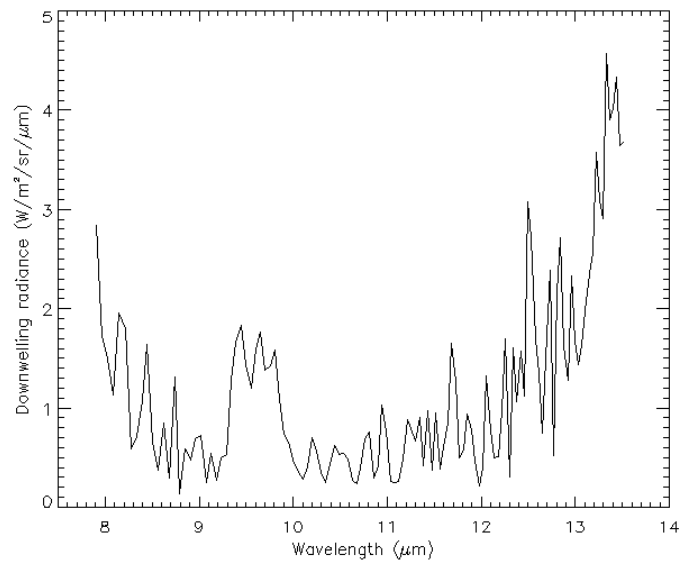

Figure 5.38: OLSTER retrieved downwelling radiance for the industrial SEBASS scene.

is enclosed and does not flow into another pond. However, the entire pond is not visible in the SEBASS image and no ground truth is available to verify this claim.

The minimum emissivity map and SAM results are shown in Figure 5.40. The minimum emissivity per pixel over the LWIR of the left pond and most of the center pond is higher than 0.96 and is appropriate for water. However, the upper right portion of the center pond and all of the pixels in the right pond have a minimum emissivity that is low for water. This appears to be caused by structured sensor noise, as a spatial region of larger errors along the scan track (vertical) on the right edges of the minimum emissivity and SAM maps can be seen. A column of low emissivity values on the left side of the minimum emissivity map is also visible and corresponds to the same line that is visible in the LST map.

The SAM values are mostly within 0.01 radians for most of the image, especially for the ponds and other natural surfaces. SAM values of less than 0.01 radians generally indicate a good match between the OLSTER LSE and the spectral emissivity from the ASTER library. Most of the spectral library is comprised of natural materials.

The SAM classification maps for four material classes are shown in Figure 5.41. Pixels with a SAM value of less than 0.01 radians for a particular class are shown in yellow. The ponds were correctly classified as water, except for the right edge of the right pond. Again, this is mostly due to the sensor noise issue along the right edge of the image. Some pixels in the industrial area were also classified as water.

Hornfels, a type of rock used as construction aggregate, was identified along what appears to be a road at the bottom of the scene, as well as on rooftops. The pixels identified as paint are scattered around the scene but are mostly concentrated on top of some structures in the industrial area. Asphalt roofing shingle is identified as the primary material of a large building. Shingle is also identified on smaller sections of other roofs in the

(a) LST map

(b) Portion of the LST map. Displayed temperatures are limited to 300 K.
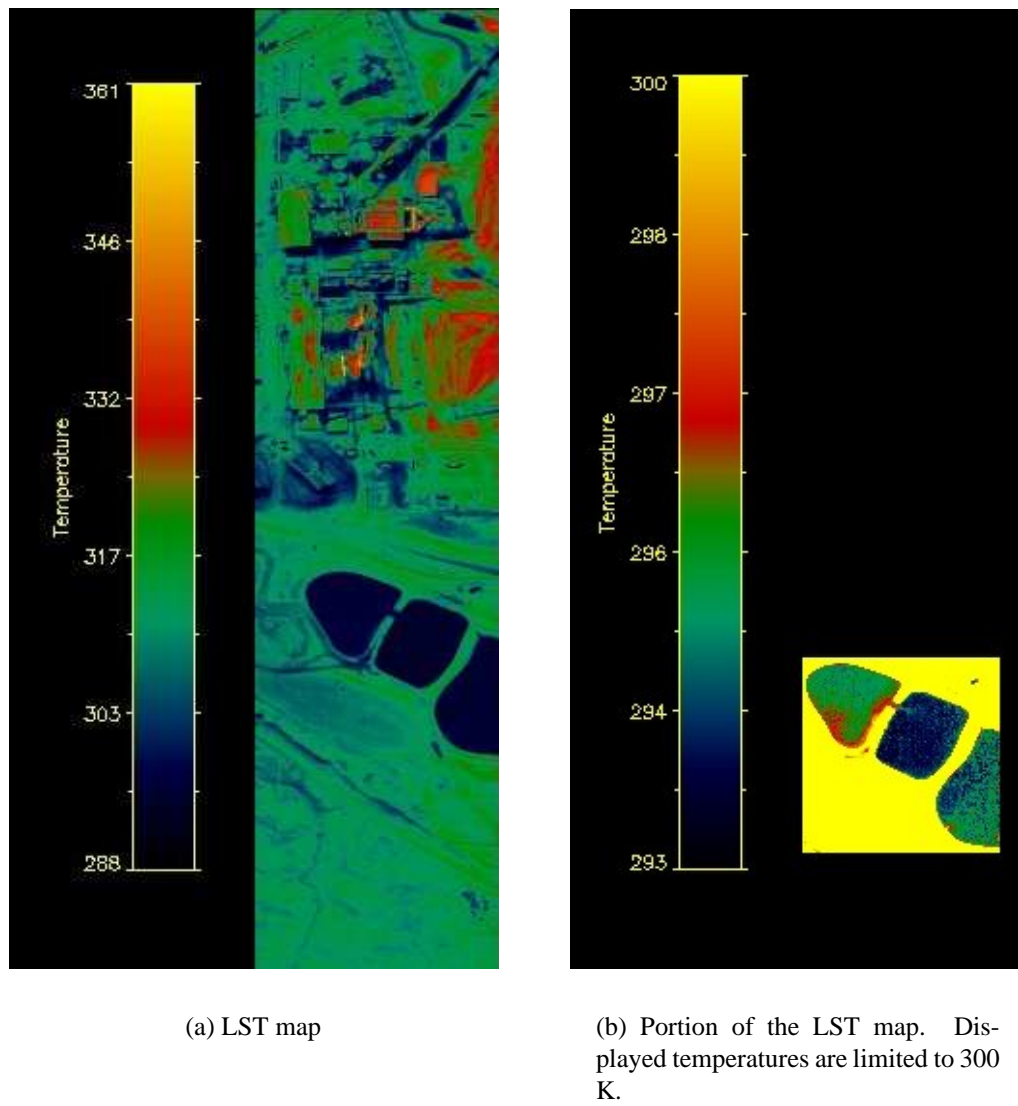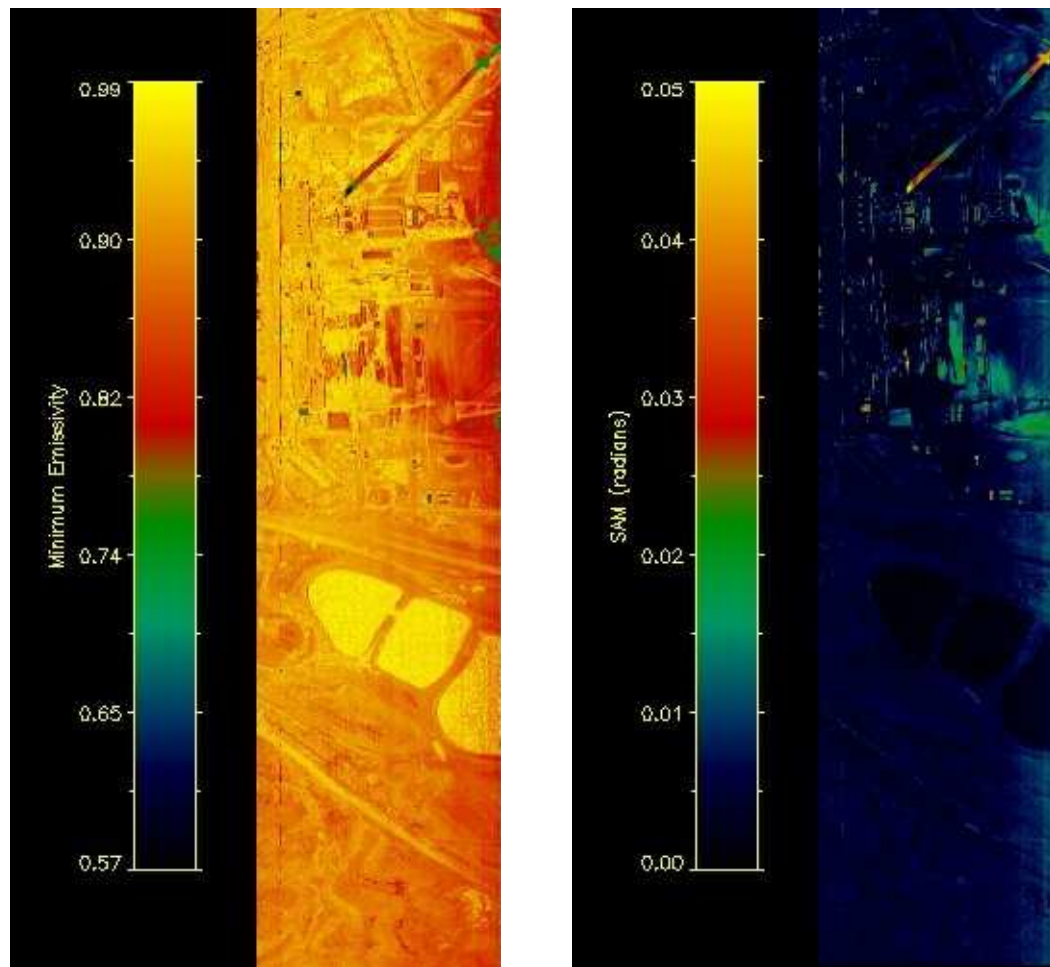
Figure 5.39: OLSTER LST maps for the industrial SEBASS imagery.

(a) Minimum emissivity per pixel   (b) Map of the SAM values

Figure 5.40: OLSTER results for the industrial SEBASS imagery.

industrial area.

The locations of seven pixels in the SEBASS industrial scene are labeled in Figure 5.42. The LST and LSE results for these pixels are shown in Figures 5.43 – 5.49. The OLSTER LSE, cubic spline smoothed LSE, and the emissivity of the best match in the ASTER spectral library are shown for each pixel, along with the retrieved LST value.

A cubic spline smoothing fit (Choi, 2002; Gao et al., 1998) to the OLSTER LSE is included in each plot for display purposes to facilitate the comparison with the library emissivity. The recommended tension value to use is in the range of 20 to 40. However, these tension values smooth over some important spectral features, particularly around the 8.6 μm region of some silicates. A tension value of 3 is used for these plots. Overall, the spectral shape and values of the OLSTER LSEs and their corresponding best match in the library are similar, and the identification of these materials in the scene is reasonable.

(a) Water   (b) Hornfels   (c) Paint   (d) Shingle
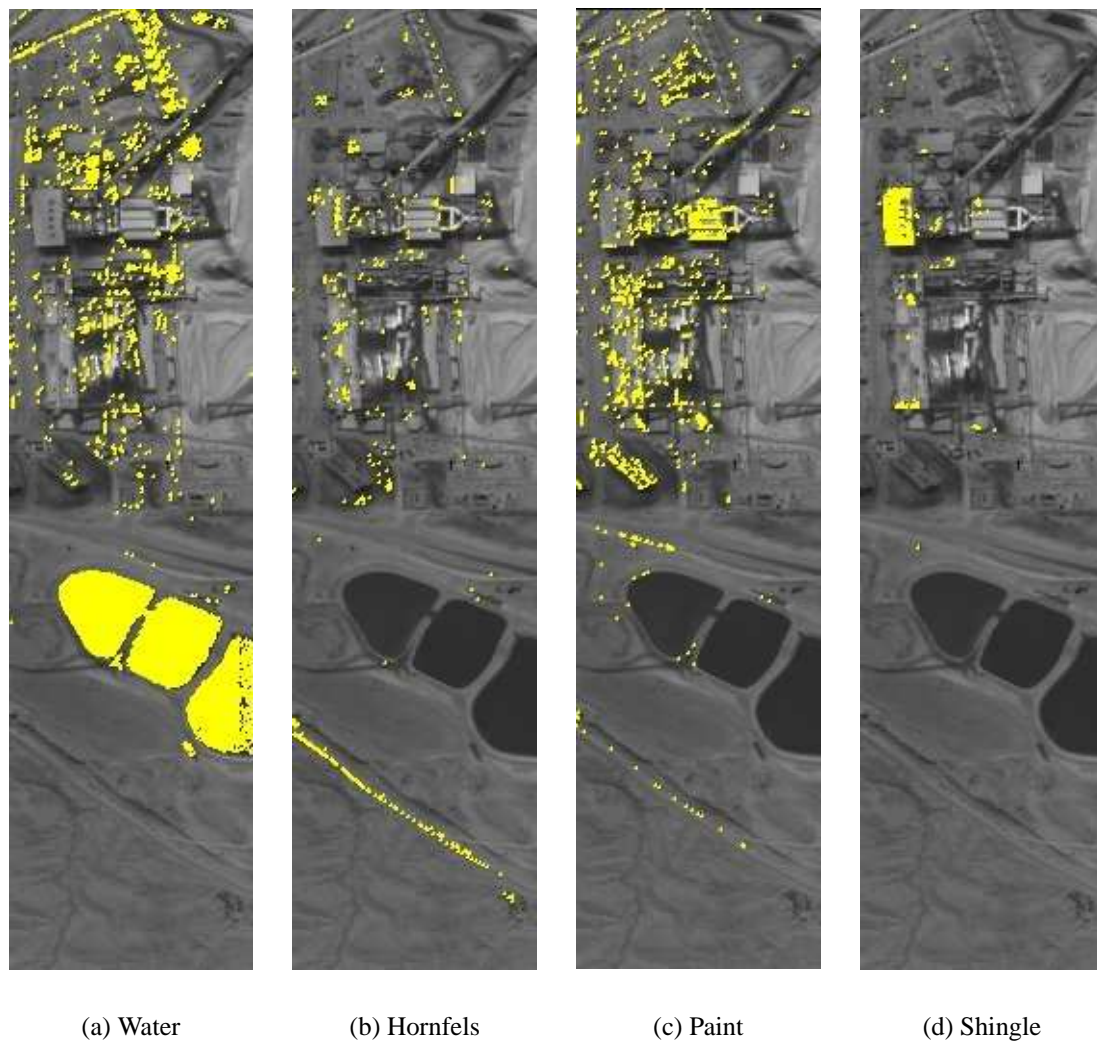
Figure 5.41: SAM classification of the OLSTER LSE results using the ASTER spectral library.

Figure 5.42: Locations of the selected points A through G for the LSE comparison.

Figure 5.43: OLSTER retrieved LSE (black line) for point A, identified as distilled water (red line) with a temperature of 297.3 K. The blue line is a cubic spline smoothed fit of the OLSTER LSE.

Figure 5.44: OLSTER retrieved LSE (black line) for point B, identified as sea foam (red line) with a temperature of 294.1 K. The blue line is a cubic spline smoothed fit of the OLSTER LSE.
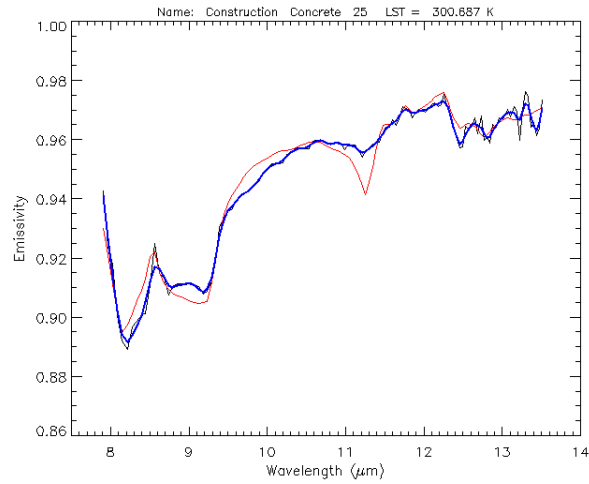
Figure 5.45: OLSTER retrieved LSE (black line) for point C, identified as construction concrete (red line) with a temperature of 300.7 K. The blue line is a cubic spline smoothed fit of the OLSTER LSE.
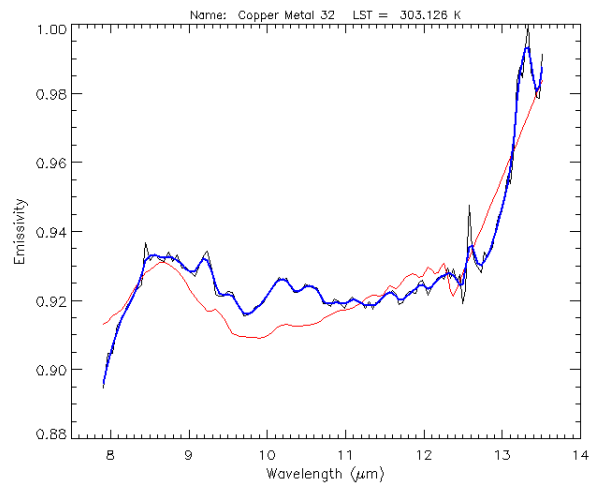
Figure 5.46: OLSTER retrieved LSE (black line) for point D, identified as a copper metal (red line) with a temperature of 303.1 K. The blue line is a cubic spline smoothed fit of the OLSTER LSE.

Figure 5.47: OLSTER retrieved LSE (black line) for point E, identified as basalt (red line) with a temperature of 296.9 K. The blue line is a cubic spline smoothed fit of the OLSTER LSE.
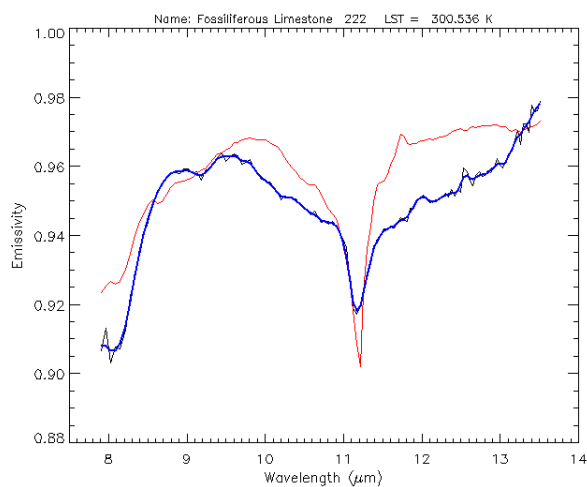
Figure 5.48: OLSTER retrieved LSE (black line) for point F, identified as limestone (red line) with a temperature of 300.5 K. The blue line is a cubic spline smoothed fit of the OLSTER LSE.
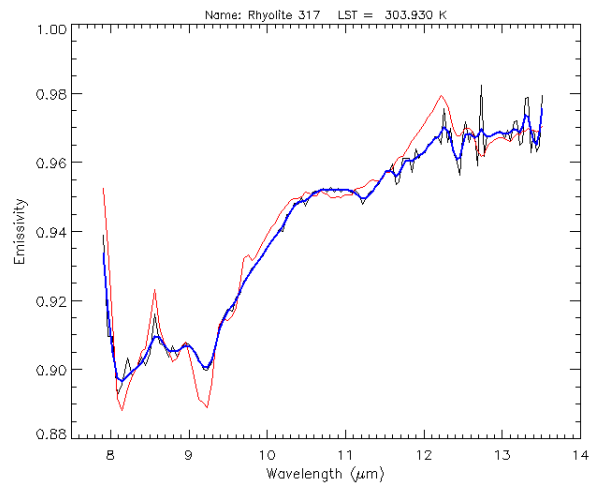
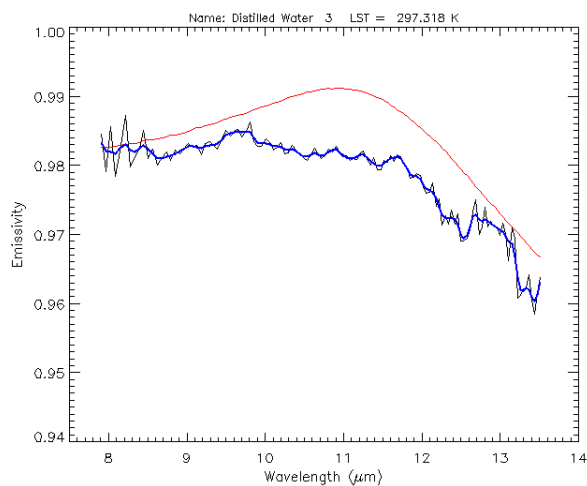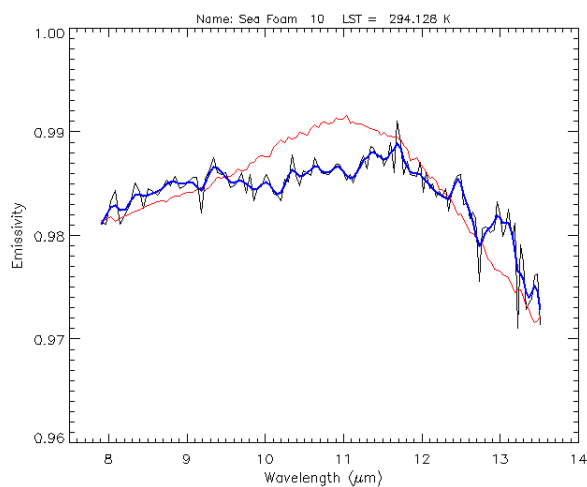Figure 5.49: OLSTER retrieved LSE (black line) for point G, identified as rhyolite (red line) with a temperature of 303.9 K. The blue line is a cubic spline smoothed fit of the OLSTER LSE.
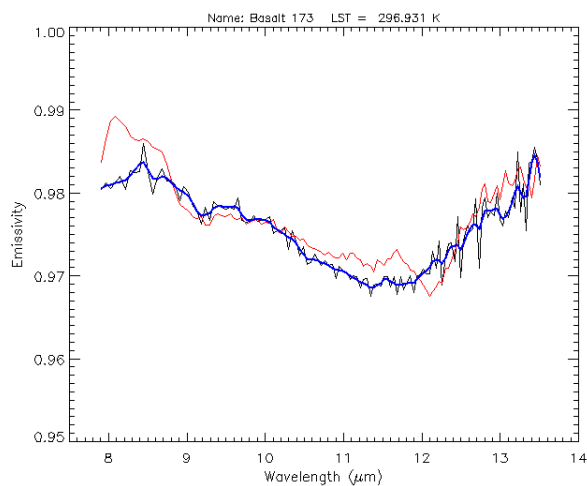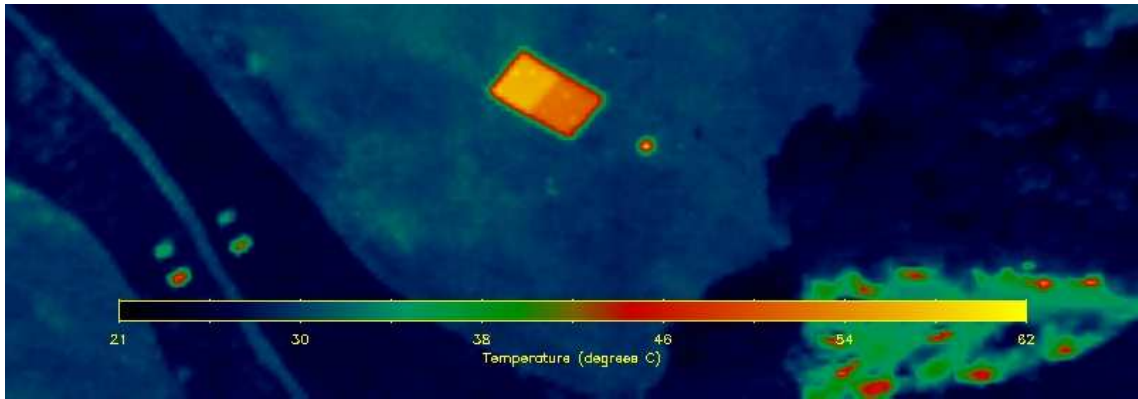
Figure 5.50: OLSTER LST map for the Rochester SEBASS data.

5.4.2 Rochester scene

The OLSTER retrieved LST map for the SEBASS Megacollect scene near Rochester, NY is shown in Figure 5.50. The large calibration tarps and thermal target are located in the center of the LST map. The tarps, thermal target, cars and various other calibration targets are the hottest pixels in the scene. The OLSTER estimated atmospheric compensation spectra are shown in Figures 5.51, 5.52, and 5.53. The shape and values of the atmospheric transmittance and upwelling radiance in general are similar to MODTRAN values for a Mid-Latitude Summer profile.

A plot of the OLSTER LST mean, minimum, and maximum values from regions of interest (ROIs) for the three calibrations targets is shown in Figure 5.54. The OLSTER results are compared to groundtruth measurements from eight individual sensors (up to three contact thermocouples (TC) on each canvas tarp, and a staring IR radiometer for each target). A contact TC on the thermal target malfunctioned, and is not shown in the plot. The east – right contact TC for the black tarp was found to be disconnected at the end of the collect, and is also not shown in the plot. The uneven solar heating due to the
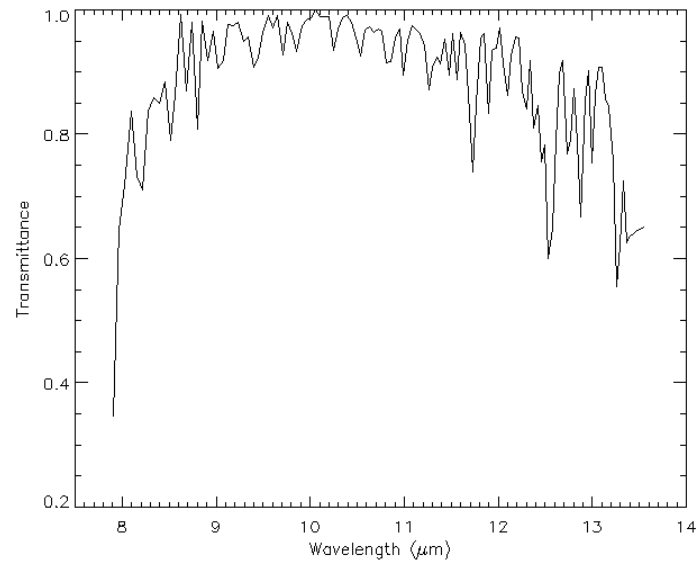
Figure 5.51: OLSTER retrieved transmittance for the Rochester SEBASS scene.
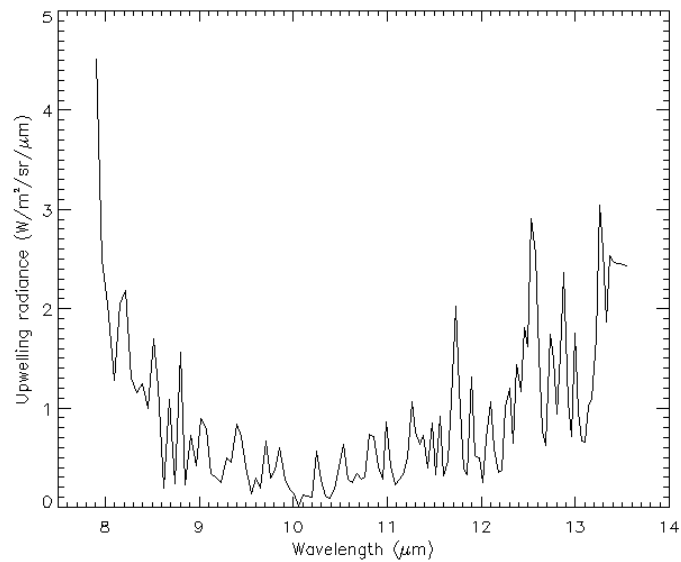
Figure 5.52: OLSTER retrieved upwelling radiance for the Rochester SEBASS scene.
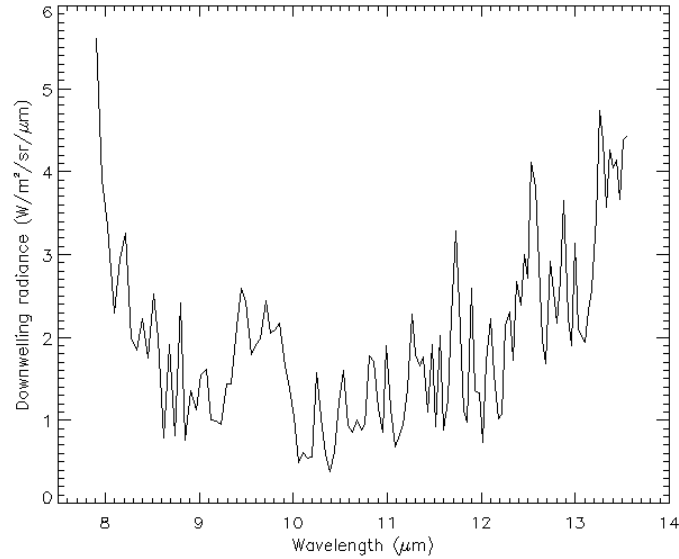
Figure 5.53: OLSTER retrieved downwelling radiance for the Rochester SEBASS scene.

irregular surface of the canvas tarps is one explanation for the variability in the contact TC measurements.

Overall, the range of OLSTER LST values are within 1 K for most of the ground measurements. However, the OLSTER minimum, maximum, and mean LST values for the gray tarp ROI are higher than the ground measurements by about 0.5 K to 3 K.

The OLSTER LSE results are shown in Figures 5.55, 5.56, and 5.57. In general, the OLSTER LSE results match the D&P Instruments model 102F measured emissivities in the 8.5 – 12.5 μm region. At the edges of the LWIR window, the OLSTER LSE results display some residual atmospheric features.
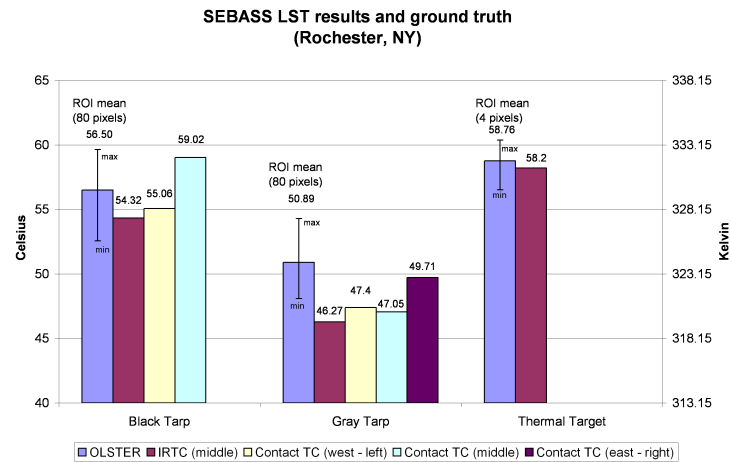
Figure 5.54: OLSTER retrieved LST compared to ground truth for the Rochester SEBASS scene.
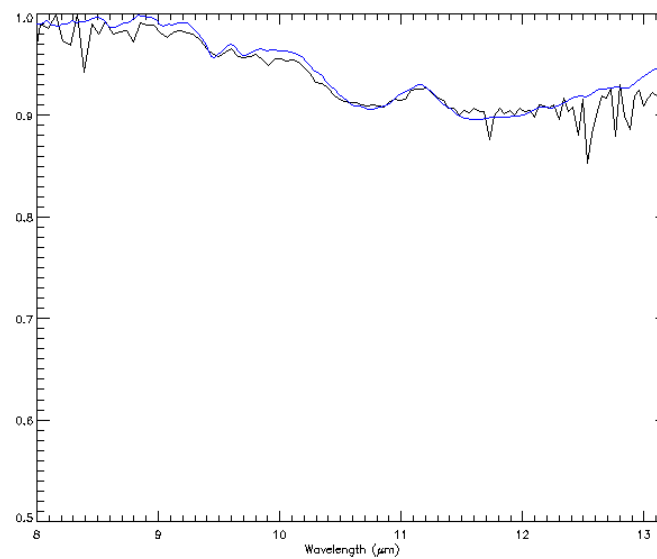
Figure 5.55: OLSTER retrieved LSE (black line) for the black canvas tarp and the measured ground truth emissivity (blue line).
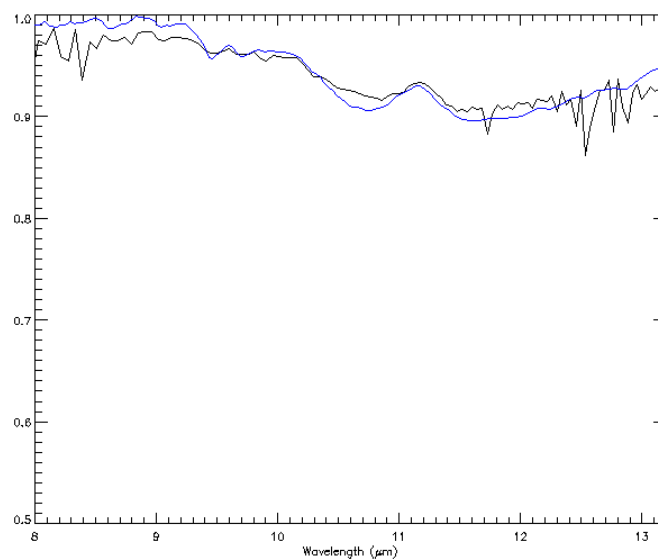
Figure 5.56: OLSTER retrieved LSE (black line) for the gray canvas tarp and the measured ground truth emissivity (blue line).
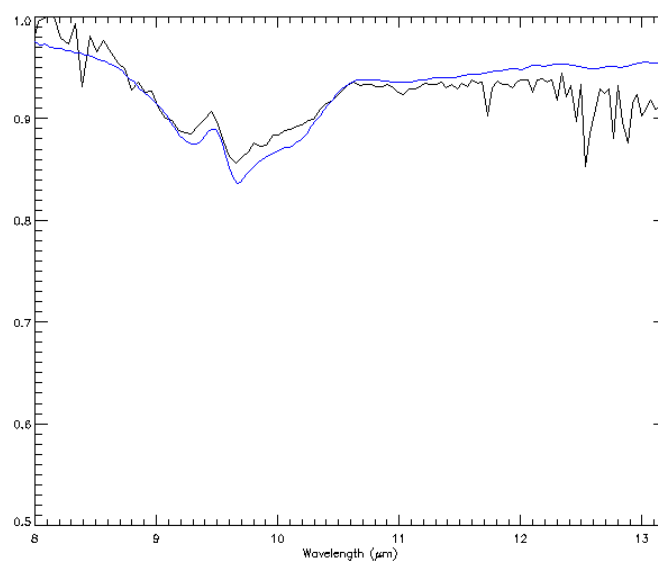
Figure 5.57: OLSTER retrieved LSE (black line) for the rubber thermal target and the measured ground truth emissivity (blue line).

5.5   Discussion

In the initial test of the OLSTER algorithm, the overall spectral shapes of the estimated atmospheric compensation spectra are correct with no discontinuities. The errors in the estimated atmospheric compensation spectra are primarily bias errors and errors associated with the ozone and water vapor absorption regions.

The results for the LST retrieval showed an expected increase in LST error with lower surface temperatures and lower emissivity values. The mostly overestimated LSTs correspond to underestimated emissivity values. The spectral shapes of the emissivity spectra are generally correct, with an increase in bias errors and artifacts in the ozone absorption region and at the edges of the TIR window as emissivity values decrease.

The sensitivity analysis study using the synthetic test scenes demonstrate OLSTER's ability to retrieve LSTs to within about 1 K and LSEs to within about 0.01 for a SNR of at least 500:1 (spectrally correlated noise only) for scenes with some blackbody pixels and thermal contrast. OLSTER is also relatively less sensitive to sensor spectral miscalibration issues compared to the ARTEMISS algorithm, with LSTs within about 2 K and LSEs to within about 0.04 for most of the spectral shifts.

The ARTEMISS results depend on the size and variability of its atmospheric database, and how well the database can model the scene's atmosphere. The database used in this study may be too small. A larger database should improve the ARTEMISS results, limited by the performance of ISSTES. ARTEMISS is relatively insensitive to sensor spectrally correlated noise, since it does not use a data – driven approach. However, it is very sensitive to sensor spectral miscalibration issues.

An ARTEMISS experiment that included the actual atmospheric parameters for the scene in the TLD database shows an improvement in the results. However, ARTEMISS was not able to select the correct atmospheric compensation spectra for the scene. For

most cases, ARTEMISS selected the same FSL radiosonde profile with a different ozone scaling factor. A comparison of the ARTEMISS results using the full TLD database with the ISSTES results shows how a small change in the ozone scaling (a scaling factor of 1.2 instead of 1.0 for all cases except for the cold surface and 100:1 SNR at 2 km) can lead to an increase in the LST and LSE retrieved errors. Modifications to the algorithm's selection of candidate atmospheres, currently using ISAC, and the ARTEMISS spectral smoothness function may lead to improved results.

While ground truth information is not available for the SEBASS industrial scene, the LST maps and material ID maps appear to be reasonable. The LSE results compared to emissivities from the ASTER spectral library show a good atmospheric compensation in general. OLSTER initially failed with unphysical values for the atmospheric parameters. An inspection of the industrial scene showed that the first column consisted of very low radiance values, possibly used for sensor calibration. The results presented in this chapter were obtained by ignoring the first column.

The ARTEMISS algorithm was also applied to the SEBASS industrial and Megacollect scenes with poor results (not shown). The ARTEMISS estimated emissivities are too low with a maximum emissivity of less than 0.5 for most bands, and the estimated surface temperatures are too high with a bias of at least 25 K. The ARTEMISS results show that the MODTRAN generated TLD atmospheric database of 7,986 entries from global radiosonde profiles does not contain enough variability to perform atmospheric compensation for any given scene. In general, the ARTEMISS algorithm will be limited by the size and variability of its TLD database for real sensor data. Validation work for the ARTEMISS algorithm on sensor data was not found in the literature review. However, good results using an upgraded version of ARTEMISS have been claimed, based on unpublished results (Borel, 2007).

The SEBASS Megacollect validation of the OLSTER algorithm demonstrates a LST retrieval within about 1 K for the black tarp and the thermal target, and within 1 K to 3 K for the gray tarp. The comparison of the OLSTER retrieved LST and ground sensor measured temperatures for the large tarps shows the difficulty associated with making a representative ground sensor measurement of a rough surface with uneven solar heating due to projected area effects. The LSE retrieval is within about 0.01 over the $8.5 - 13$ μm spectral region for the canvas tarps. The LSE error at the edges of the LWIR window are a result of residual atmospheric features that have not been completely compensated for. In general, the spectral shape of the OLSTER retrieved emissivities match the ground truth measurements well with very little bias error. The conclusions and future work are presented in the next chapter.

Chapter 6

Conclusions

A new algorithm was developed for atmospheric compensation and surface parameter retrieval of hyperspectral TIR images. The OLSTER algorithm accounts for downwelling radiance and can retrieve the emissivities from both natural and man-made materials. The main steps in the algorithm include a preprocessing step, an iterative search for near-blackbody pixels ($\varepsilon(\lambda) \approx 1$), and a constrained optimization of the atmospheric parameters.

The preprocessing step simplifies the retrieval problem with a blackbody assumption to provide initial estimates of the atmospheric parameters, $\hat{\tau}(\lambda)$ and $\hat{L}_u(\lambda)$, and surface temperatures. The estimated parameters are refined during the search for near-blackbody pixels by performing linear regressions on the pixels that best satisfy the blackbody assumption. Finally, the blackbody assumption is relaxed, and the remaining terms in the RTE are solved for. The downwelling radiance, $\hat{L}_d(\lambda)$, is estimated from $\hat{L}_u(\lambda)$ using a LUT of regression coefficients. The temperature, $\hat{T}_s(x)$, and emissivity, $\hat{\varepsilon}(x, \lambda)$, estimates are retrieved using the ISSTES algorithm with a modified spectral smoothness function. The atmospheric parameters are then optimized in a GRG iterative loop that minimizes

the spectral smoothness measure of the $\varepsilon(\lambda) \approx 1$ pixels while satisfying constraints that ensure physical results.

A TIR initial test image was created with surface materials from the ASTER spectral library, with a range of emissivities from about 0.15 to 1.0, and a range of LSTs from 260 K to 320 K. The test image contains 11,850 spectrally pure pixels. The search for near-blackbody pixels selects 380 pixels in four iterations, and the optimization loop is completed in eight iterations. The spectral shapes of the atmospheric parameters are retrieved accurately, in general, with a maximum transmittance error of + 0.003, a maximum upwelling radiance error of - 0.03 $\frac{W}{m^2 sr \mu m}$, and a maximum downwelling radiance error of - 0.3 $\frac{W}{m^2 sr \mu m}$. The errors for LST are mostly within 2 K for surfaces with a minimum emissivity of 0.5 or higher, and within 0.3 K for the near-blackbody pixels. However, accurate LST retrieval on very low emissivity ($\varepsilon(\lambda) \approx 0.15$) metal surfaces was difficult, with errors from - 2 K to about + 30 K. The spectral shape of the retrieved emissivities generally matched the materials in the spectral library, with larger errors for lower emissivity values, particularly in the ozone absorption spectral region and at the edges of the TIR window. The emissivities were mostly underestimated, which corresponds to the mostly positive bias for the LST estimates.

Results from the initial test led to improvements in OLSTER's processing speed and memory requirements, adaptive GRG constraints, and an expanded downwelling radiance LUT. The computational memory requirement is directly related to the number of variables that are adjusted in GRG. The approach of using a vector of $\hat{\tau}(\lambda)$ and $\hat{L}_u(\lambda)$ variables requires a large Jacobian matrix that must be evaluated for each iteration of the GRG algorithm. Scaling factors for $\hat{\tau}(\lambda)$, $\hat{L}_u(\lambda)$, and $\hat{L}_d(\lambda)$ are the GRG input variables for the initial GRG step. With only three variables to adjust, the number of constraints are also reduced to fewer than two. An initial GRG optimization of the scaling factors before

the final GRG optimization per band generally reduces the convergence time. Adaptive GRG constraints relax the bounds in the initial iteration of the optimization loop if GRG fails to converge. The constraints are then tightened to promote a faster convergence. An expanded LUT uses additional model atmospheres generated using radiosonde data and a greater range of ozone and water vapor variations. The expanded LUT also required a new process to select the best LUT entry for OLSTER to use. The OLSTER IDL code does not require user inputs during processing. However, a cloud mask and removal of bad columns and noisy bands may be required in preprocessing.

A sensitivity analysis of the sensor altitude, noise, and spectral miscalibration was performed. Special cases of a desert environment and a night case were also tested. OLSTER is capable of retrieving LSTs to within about 1 K and LSEs to within about 0.01 for a SNR of at least 500:1 for scenes with some blackbody pixels and thermal contrast. OLSTER is also relatively less sensitive to sensor spectral miscalibration issues compared to the ARTEMISS algorithm, with LSTs within about 2 K and LSEs to within about 0.04 for most of the spectral shifts.

A validation of the approach using TIR hyperspectral imagery from the AHI and SEBASS sensors with ground truth for the Megacollect scene was performed. The OLSTER algorithm retrieved LSTs to within about 1 K for the black tarp and the thermal target, and within 1 K to 3 K for the gray tarp. The LSE retrieval is within about 0.01 over the $8.5 - 13 \ \mu$m spectral region for the canvas tarps. The OLSTER algorithm is currently one of only a few algorithms available that have been documented to retrieve accurate land surface temperatures and absolute land surface spectral emissivities from passive airborne hyperspectral LWIR sensor imagery.

6.1   Future Work

The main areas for future work include implementing multiple starting points in OL-STER, a repeat of the night scene simulation, continued validation of the OLSTER algorithm using new sensor data with corresponding ground truth measurements, and an analysis of the size and variability of the atmospheric database required for ARTEMISS. Multiple starting points in OLSTER may be able to improve the retrieval results for the desert and night temperature cases. For example, OLSTER atmospheric compensation results for an adjacent scene may be applied to a desert flight line to provide OLSTER with a different starting point. The night scene simulation should be repeated using both cold surface temperatures and an atmosphere modeled using a night radiosonde profile. The validation of the OLSTER algorithm should continue as additional sensor data with ground truth measurements are made available.

Bibliography

Abadie, J. and Carpentier, J. (1969). Generalization of the wolfe reduced gradient method to the case of nonlinear constraints. In *Optimization*, pages 37–47.

ASTER (1999). ASTER spectral library. Pasadena, California. http://speclib.jpl.nasa.gov/.

Berk, A., Anderson, G. P., S.Bernstein, L., Acharya, P. K., Dothe, H., Matthew, M. W., Adler-Golden, S. M., J. H.Chetwynd, J., Richtsmeier, S. C., Pukall, B., Allred, C. L., Jeong, L. S., and Hoke, M. L. (1999). MODTRAN4 radiative transfer modeling for atmospheric correction. In *Proceedings of SPIE Optical Spectroscopic Techniques and Instrumentation for Atmospheric and Space Research III*, volume 3756, pages 348–353.

Borel, C. C. (1998). Surface emissivity and temperature retrieval for a hyperspectral sensor. In *IGARSS 1998*, volume 1, pages 546–549. IEEE International Geoscience and Remote Sensing Symposium.

Borel, C. C. (2003). ARTEMISS - an algorithm to retrieve temperature and emissivity from hyper-spectral thermal image data. In *28th Annual GOMACTech Conference, Hyperspectral Imaging Session, March 31, 2003 to April 3, 2003 Tampa, Florida.*

Los Alamos Natioanl Laboratory unclassified report LA-UR-027907. http://nis-www.lanl.gov/ borel.

Borel, C. C. (2007). personal communication.

Bower, N., Knuteson, R. O., and Revercomb, H. E. (1999). High spectral resolution land surface temperature and emissivity measurement in the thermal infrared. In *Proceedings from the AMS 10th Conference on Atmospheric Radiation, Madison, WI.*, page 7B.4. American Meteorological Society, Boston, Massachusetts.

Choi, H. (2002). Spectral misregistration correction and simulation for hyperspectral imagery. Master's thesis, Rochester Institute of Technology.

Dash, P., Göttsche, F., Olesen, F., and Fischer, H. (2002). Land surface temperature and emissivity estimation from passive sensor data: theory and practice-current trends. *International Journal Remote Sensing*, 23(13):2563–2594.

Frontline Systems (2000). Standard excel solver, problems with poorly scaled models. http://www.solver.com/suppstdscaling.htm.

FSL (2005). NOAA Forecast Systems Laboratory. Boulder, Colorado. http://www.fsl.noaa.gov/.

Gao, B., Liu, M., and Davis, C. O. (1998). A new and fast method for smoothing spectral imaging data. In *Airborne Geoscience Workshop Proceedings*.

Gillespie, A. R., Rokugawa, S., Matsunaga, T., Cothern, J. S., Hook, S., and Kahle, A. B. (1998). A temperature and emissivity separation algorithm for advanced spaceborne thermal emission and reflection radiometer (ASTER) images. *IEEE-Transactions-on-Geoscience-and-Remote-Sensing*, 36(4):1113–1126.

Gu, D., Gillespie, A. R., Kahle, A. B., and Palluconi, F. D. (2000). Autonomous atmospheric compensation of high resolution hyperspectral thermal infrared remote-sensing imagery. *IEEE Transactions on Geoscience and Remote Sensing*, 38(6):2557–2570.

Hayashi, J. N. and Sharp, M. H. (2002). Hyperspectral LWIR automated separation of surface emissivity and temperature (ASSET). *Imaging Spectrometry VIII, Proceedings of SPIE*, 4816:258–269.

Hernandez-Baquero, E. D. (2000). *Characterization of the Earth's surface and atmosphere from multispectral and hyperspectral thermal imagery*. PhD thesis, Rochester Institute of Technology.

Ingram, P. M. and Muse, A. H. (2001). Sensitivity of iterative spectrally smooth temperature/emissivity separation to algorithmic assumptions and measurement noise. *IEEE Transactions on Geoscience and Remote Sensing*, 39(10):2158–2167.

Kirkland, L., Herr, K., Keim, E., Adams, P., Salisbury, J., Hackwell, J., and Treiman, A. (2002). First use of an airborne thermal infrared hyperspectral scanner for compositional mapping. *Remote sensing of environment*, 80(3):447–459.

Lasdon, L. S. and D.Waren, A. (1980). A survey of nonlinear programming applications. *Operations Research*, 28(5):1029–1063.

Lasdon, L. S. and Smith, S. (1992). Solving large sparse nonlinear programs using GRG. *ORSA Journal on Computing*, 4(1):1–15.

Lasdon, L. S., Waren, A. D., Jain, A., and Ratner, M. (1978). Design and testing of a generalized reduced gradient code for nonlinear programming. *ACM Transactions on Mathematical Software*, 4(1):34–50.

Li, Z.-L., Becker, F., Stoll, M. P., and Wan, Z. (1999). Evaluation of six methods for extracting relative emissivity spectra from thermal infrared images. *Remote Sensing of Environment*, 69(3):197–214.

Liang, S. (2000). Inversion of land surface temperature and emissivity simultaneously from multispectral thermal infrared imagery. In *IGARSS 2000*, volume 7, pages 3133–3135. IEEE International Geoscience and Remote Sensing Symposium.

Lucey, P. G., Williams, T. J., Mignard, M., Julian, J., Kobubun, D., Allen, G., Hampton, D., Schaff, W., Schlangen, M. J., Winter, E. M., Kendall, W. B., Stocker, A. D., Horton, K. A., and Bowman, A. P. (1998). AHI: an airborne long-wave infrared hyperspectral imager. In *Proceedings of SPIE Airborne Reconnaissance XXII*, volume 3431, pages 36–43.

Luenberger, D. G. (1973). *Introduction to linear and nonlinear programming*. Addison-Wesley, Massachusetts.

Norman, J. M. and Becker, F. (1995). Terminology in thermal infrared remote sensing of natural surfaces. *Agricultural and Forest Meteorology*, 77:153–166.

Papalambros, P. Y. and Wilde, D. J. (2000). *Principles of optimal design: Modeling and computation*. Cambridge University Press, UK, second edition.

Peterson, E. D., Brown, S. D., Hattenberger, T. J., and Schott, J. R. (2004). Surface and buried landmine scene generation and validation using the Digital Imaging and Remote Sensing Image Generation model. *Proceedings-of-the-SPIE-The-International-Society-for-Optical-Engineering*, 5546:312–323.

Prata, A., Caselles, V., Coll, C., Sobrino, J., and Ottlé, C. (1995). Thermal remote sens-

ing of land surface temperature from satellites: current status and future prospects. *Remote Sensing Reviews*, 12:175–224.

Raqueno, N. G., Smith, L. E., Messinger, D. W., Salvaggio, C., Raqueno, R. V., and Schott, J. R. (2005). Megacollect 2004: hyperspectral collection experiment of terrestrial targets and backgrounds of the RIT Megascene and surrounding area (Rochester, New York). *Proceedings-of-the-SPIE-The-International-Society-for-Optical-Engineering*, 5806:554–565.

Research Systems (2005). Interactive Data Language, IDL 6.1. Boulder, Colorado.

Schmugge, T., French, A., Ritchie, J. C., Rango, A., and Pelgrum, H. (2002). Temperature and emissivity separation from multispectral thermal infrared observations. *Remote Sensing of Environment*, 79:189–198.

Singh, C. and Sarkar, D. (1992). Practical considerations in the optimisation of induction motor design. *IEE Proceedings,Part B, Electric Power Applications*, 139(4):365–373.

Sobrino, J. A., Cuenca, J., Kharraz, H. E., and Dempere, L. (1998). Experimental investigation of the angular variation of emissivity in the thermal infrared band. *Proceedings-of-the-SPIE-The-International-Society-for-Optical-Engineering*, 3499:427–436.

Tonooka, H. (2001). An atmospheric correction algorithm for thermal infrared multispectral data over land — a water-vapor scaling method. *IEEE Transactions on Geoscience and Remote Sensing*, 39(3):682–692.

Wan, Z. and Li, Z.-L. (1997). A physics-based algorithm for retrieving land-surface emis-

sivity and temperature from EOS/MODIS data. *IEEE Transactions on Geoscience and Remote Sensing*, 35(4):980–996.

Wan, Z., Zhang, Y., Zhang, Q., and Li, Z.-L. (2002). Validation of the land-surface temperature products retrieved from Terra MOderate Resolution Imaging Spectroradiometer data. *Remote Sensing of Environment*, 83(1-2):163–180.

Windward Technologies and Optimal Methods (1997). User's guide for GRG2 optimization library. http://www.maxthis.com/Grg2ug.htm.

Young, S. J., Johnson, B. R., and Hackwell, J. A. (2002). An in-scene method for atmospheric compensation of thermal hyperspectral data. *Journal of Geophysical Research*, 107(D24):ACH 14.

Appendices

Appendix A

Requirements for running OLSTER

The OLSTER algorithm is coded in the Interactive Data Language (IDL) version 6.1. The minimum requirement for running OLSTER is IDL version 5.1, which includes the Constrained_Min function for GRG optimization. Access to the radiative transfer code MODTRAN4 is needed to generate a LUT of upwelling radiance to downwelling radiance regression coefficients for the appropriate sensor altitude. The upwelling radiance and downwelling radiance values need to be resampled using the sensor's spectral response function before computing the regression coefficients. A database of atmospheric radiosonde profiles with global coverage is required for the MODTRAN runs.

The input data for OLSTER includes a LWIR hyperspectral radiance image (nadir or near-nadir viewing angle), the sensor spectral response, a pre-computed LUT of upwelling radiance to downwelling radiance regression coefficients, and the sensor altitude. It is necessary to remove any bad data lines and areas with clouds from the image before running OLSTER to avoid violating the algorithm's assumptions. After compiling the program files and selecting the filenames for the input data, the OLSTER code requires no additional user inputs. The OLSTER code provides useful information for monitoring

its progress, such as the number of near-blackbody pixels selected, previous and current objective function values, GRG inform values, and the minimum and maximum values of the atmospheric compensation spectra, LST and spectral LSE preliminary estimates. The output results from OLSTER includes the atmospheric compensation spectra, estimated LST per pixel, and estimated spectral LSE per pixel.

Appendix B

Determining if OLSTER results are reasonable

In the absence of ground truth surface temperature and emissivity measurements, other methods are available to determine if the results from OLSTER are reasonable in a qualitative sense. The methods involve an analysis of the OLSTER retrieved LST and LSE products, the atmospheric compensation spectra, and the GRG optimization inform values and objective function results.

A map of the OLSTER retrieved LST per pixel should be examined to determine if the values are reasonable given the location of the image scene, the time of day, and scene content. The OLSTER retrieved spectral LSE should contain a minimal amount of residual atmospheric features that have not been compensated for. The sharp spectral signatures correspond to atmospheric absorption or emission features, such as the 11.7 μm water vapor absorption feature, the 9.6 μm region for ozone, and water vapor and carbon dioxide features at both edges of the LWIR window.

Image areas containing water pixels should have high emissivity values, generally

higher than 0.96. Healthy vegetation should have emissivities greater than 0.9. It is useful to display the minimum emissivity over all sensor channels per pixel, as shown in Figure 5.40(a) for the industrial SEBASS image. A map of the minimum emissivity per pixel may show unexpected spatial patterns for a given class of surface materials that can correspond to structured sensor noise, sensor radiometric calibration issues, and non-uniform regions of atmospheric compensation.

The OLSTER retrieved spectral LSE can also be compared to a spectral database of material emissivities, such as the ASTER spectral library. A classifier, such as the spectral angle mapper, can report the best match in the database per pixel and how close the match is. Displaying the results with a user adjusted threshold of classification, as shown in Figure 5.40(b) for industrial SEBASS data, may reveal underlying issues with the surface parameter retrieval.

Another useful way to display the OLSTER retrieved emissivities is to plot the spectral emissivities for all pixels on a single graph. Most natural materials have emissivities greater than 0.9, and an overplot of all the LSEs may help determine if they are biased or have residual atmospheric compensation errors. Also, when there are no LSE values greater than 0.9, it may be an indication of bias errors in the atmospheric compensation spectra, in particular the atmospheric transmittance.

The spectral shape and values of the atmospheric compensation spectra can be compared to reference atmospheric transmittance, upwelling radiance, and downwelling radiance spectra generated using MODTRAN with default profiles or user defined radiosonde profiles. Large errors in the shape of the atmospheric compensation spectra should also correspond to similar spectral shape errors in the retrieved emissivities.

Finally, the objective function values and GRG inform values at each iteration of the GRG optimization loop can be used to examine the convergence of the optimization step.

The objective function value should decrease at each iteration. If progress appears to be slow or stalled, the solution may be at a local minimum which requires a different starting point.

Appendix C

Things to try if OLSTER is not working for you

The results of the OLSTER algorithm are generally dependent on the spectral shape of the atmospheric compensation spectra from the initialization step. Bias errors are easy to overcome in the initial optimization loop using atmospheric scaling factors. Errors in the spectral shape of the atmospheric compensation spectra may be caused by an improper selection of near-blackbody pixels, sensor noise and calibration issues, and a non-uniform atmosphere over the entire image. The locations of the near-blackbody pixels should correspond to water and vegetation pixels, in general. Image segmentation or masking may be required to remove areas of the image that are incorrectly classified as near-blackbody pixels due to sensor noise issues or low thermal contrast. Noisy data lines along the sensor's scan track and dead pixels or lines should also be removed from the data set. The OLSTER algorithm assumes a nadir or near-nadir sensor viewing angle. Data columns along the edges of the scan track may need to be removed for sensor data with a large field of view (FOV) or with optical vignetting issues.

In addition to removing some pixels from the image data, it may also be necessary to remove some spectral bands from the data, especially at the edges of the LWIR window. For example, the GRG optimization constraints or the objective function may encounter difficulties at only a few particular bands that prevent the convergence to a better solution. Identifying and removing a few bands will facilitate further progress in the optimization step without resorting to a modification of the constraint functions or the objective function for a specific image.

Finally, multiple starting points using OLSTER results from adjacent scenes may be useful for scenes with few high emissivity pixels, low thermal contrast, or noisy data. The OLSTER atmospheric compensation spectra from another scene can be used instead of the initialization step (modified ISAC step) in OLSTER.

Appendix D

Known issues

The OLSTER algorithm was designed to be widely applicable with minimal user inputs during processing. The optimization constraints, objective function, thresholds for the correlation and concavity metrics, and stopping criteria for iteration loops worked well for the synthetic test data, the AHI sensor data and the SEBASS sensor data. The preprocessing used for the AHI data involved spectrally binning 256 sensor channels down to 50 channels to improve the SNR. The industrial SEBASS scene required the removal of the first spatial data column, which contained the same radiance value for each spectral channel for every pixel in the column and may be an undocumented sensor calibration line or bad data. The Rochester Megacollect SEBASS scene required the removal of the first ten and last ten spatial data columns from the image due to sensor noise issues.

One known issue remains regarding the modification of the ISAC algorithm in the initialization step of OLSTER. The modification was designed for scenes that are not dominated by high emissivity pixels that the ISAC algorithm requires. The modification removes pixels with a large range in brightness temperature values compared to the median range for all pixels. The modification works well for most scenes, but may remove

too many pixels in some cases. The remaining pixels in these cases may have little thermal contrast, and it may be better to avoid removing pixels in the initialization step. Unfortunately, it is not clear which case applies to a given scene before running OLSTER. The current approach is to run OLSTER for both cases (with and without the modification to the ISAC algorithm) up to the start of the final GRG optimization loop. The case with the lower objective function value continues to the final optimization step.